UNIVERSITY OF CALIFORNIA, SAN DIEGO

Nanofabrication, nanomagnetism and other applications of nanostructures

A dissertation submitted in partial satisfaction of the
requirements for the degree Doctor of Philosophy
in
Physics

by

Chang-Peng Li

Committee in charge:

Professor Ivan K. Schuller, Chair
Professor John M. Goodkind
Professor Yu-Hwa Lo
Professor Michael J. Sailor
Professor Lu Jeu Sham

2007

The dissertation of Chang-Peng Li is approved, and it is acceptable in quality and form for publication on microfilm:

Chair

University of California, San Diego

2007

TABLE OF CONTENTS

LIST OF FIGURES

LIST OF TABLES

ACKNOWLEDGEMENTS

This dissertation owes its existence to the help, support, and inspiration of many people. First of all, I would like to express my deep and sincere gratitude to my advisor, Professor Ivan K. Schuller for his supervision, encouragement and guidance for my research. In Ivan's group, I stepped into the fascinating nano-world for the first time in my life. His critical and constructive comments are great driving forces for me to continue with my research. What I learned from him is not only how to do solid research, but also, and most importantly, how to be a responsible and successful research scientist. All of these will be great assets for my future career.

Most of the results in this dissertation have been achieved in collaboration with Dr. Igor V. Roshchin and Prof. Xavier Batlle. I want to take this chance to express my utmost appreciation for their personal assistance, guidance, and valuable discussions. I also thank Casey E. Chiang and David Tagatac for their critical reading and constructive comments of this dissertation. I also have to thank Dr. Bernd Fruhberger, Dr. Amos Sharoni, and Corneliu Colesniuc for their help with argon-ion milling, George Kassabian for his help in building the electronic system for automated control of the anodization, and Dr. Casey Miller, Dr. Zhi-Pan Li, Dr. Rafael Morales, and Ge Liu for their illuminating discussions, and frank suggestions for my research and papers.

In addition, discussion and cooperation with all of my colleagues have contributed substantially to this work. I gratefully acknowledge Randy Dumas and Prof. Kai Liu for the First Order Reversal Curve measurements, Jose Mejía-López, Dora Altbir and Prof. A. H. Romero for the Monte Carlo simulations, Dr. Michel Viret, Prof. Frédéric Ott, Dr. Mike R. Fitzsimmons, Dr. Sungkyun Park, Dr. Roger Pynn, Dr. Sujoy Roy and Prof. Sunil Sinha for the neutron scattering measurements, Dr. Javier E. Villegas for the interaction between superconductor and nanomagnets, Dr. Fèlix Casanova, Casey E. Chiang, Anne M. Ruminski, Sara Alvarez and Prof. Michael J. Sailor for porous alumina as a chemical sensing and biosensing chip, and Dr. Thomas Gredig for the study of magnetic nanodots with cut-edge.

Finally and foremost, I want to express my apology and appreciation to my family, especially to my wife, Yang Bai. Because of me, she sacrificed a wonderful

opportunity to become a lawyer in China and came to the USA as a housewife. It's her selfless love and support that helped me to smoothly complete my dissertation research. I also want to express my deepest apologies to my son Lingwen Li, born on Oct. 1, 2006, whom I have regretfully not been able to spend as much time with as I would have desired in the first year of his life. Moreover, I also want to show great appreciation to my parents, Fushan Li and Guiping Zhang, who came to the USA to help us take care of Lingwen.

In addition, support by The Air Force Office of Scientific Research is gratefully acknowledged. I would also like to thank everybody who was important to the successful realization of this dissertation, as well as expressing my apology that I could not mention each and every one.

VITA

2007	Doctor of Philosophy in Physics University of California at San Diego, La Jolla, CA
2003	Master of Science in Physics Shandong University, Jinan, P.R. China
2002	Bachelor of Science in Physics Shandong University, Jinan, P.R. China

PUBLICATIONS

F. Casanova, C. E. Chiang, C.-P. Li, and Ivan K. Schuller, Direct observation of pore blocking and advanced adsorption in nanoporous alumina: cooperative effects at the origin of hysteresis, submitted to *Appl. Phys. Lett.*

R. K. Dumas, C.-P. Li, I. V. Roshchin, Ivan K. Schuller, and K. Liu, Temperature induced single domain - vortex state transition in sub-100nm Fe nanodots, submitted to *Appl. Phys. Lett.*

I. V. Roshchin, C.-P. Li, H. Suhl, X. Batlle, S. Roy, S. K. Sinha, S. Park, R. Pynn, M. R. Fitzsimmons, J. Mejía-López, D. Altbir, A. H. Romero, and Ivan K. Schuller, Measurement of the vortex core magnetization in sub-100 nm Fe dots using polarized neutron scattering, submitted to *Phys. Rev. Lett.*

F. Casanova, C. E. Chiang, C.-P. Li, I. V. Roshchin, Ivan K. Schuller, A. M. Ruminski, and M. J. Sailor, Effect of surface interactions on the hysteresis of capillary condensation in nanopores, submitted to *Europhys. Lett.*

J. E. Villegas, C.-P. Li, and Ivan K. Schuller, Bistability of a superconducting film induced by magnetic vortices, accepted by *Phys. Rev. Lett.*

R. K. Dumas, C.-P. Li, I. V. Roshchin, Ivan K. Schuller, and K. Liu, Magnetic fingerprint of sub-100 nm Fe nanodots, *Phys. Rev. B* 75, 134405 (2007). Also selected in April 16, 2007 issue of *Virtual Journal of Nanoscale Science & Technology.*

J. E. Villegas, M. I. Montero, C.-P. Li, and Ivan K. Schuller, Correlation length of quasiperiodic vortex-lattices, *Phys. Rev. Lett.* 97, 027002 (2006). Also selected in July 31, 2006 issue of *Virtual Journal of Nanoscale Science & Technology* and July 15, 2006 issue of *Virtual Journal of Applications of Superconductivity.*

J. Mejía-López, D. Altbir, A. H. Romero, X. Batlle, I. V. Roshchin, C.-P. Li, and Ivan K. Schuller, Vortex state and effect of anisotropy in sub-100-nm magnetic nanodots, *J. Appl. Phys.* 100, 104319 (2006).

C.-P. Li, I. V. Roshchin, X. Batlle, M. Viret, F. Ott, and Ivan K. Schuller, Fabrication and structural characterization of highly ordered sub-100 nm planar magnetic nanodot arrays over 1 cm^2 coverage area, *J. Appl. Phys.* 100, 074318 (2006).

J.-F. Wang, W.-B. Su, H.-C. Chen, W.-X. Wang, G.-Z. Zang, C.-P. Li, S. Bodde, (Pr, Co, Nb)-Doped SnO_2 Varistor Ceramics, *J. Am. Ceram. Soc.* 88,331 (2005).

C.-P. Li, J.-F. Wang, W.-B. Su, H.-C. Chen, Y.-J. Wang, and D.-X. Zhuang, Effect of sinter temperature on the electrical properties of TiO_2-based capacitor-varistors, *Mater. Lett.* 57, 1400 (2003).

W.-B. Su, J.-F. Wang, H.-C. Chen, W.-X. Wang, G.-Z. Zhang, and C.-P. Li, Nonlinear electrical behavior of the $TiO_2 \cdot WO_3$ varistor, *J. Appl. Phys.* 92, 4779, (2002).

J.-F. Wang, H.-C. Chen, W.-X. Wang, G.-Z. Zhang, and C.-P. Li, Novel $TiO_2 \cdot WO_3$ varistor system, *Mat. Sci. Eng. B-Solid* 99, 461 (2002).

C.-P. Li, J.-F. Wang, X.-S. Wang, H.-C. Chen, and W.-B. Su, Nonlinear electrical properties of Ta-doped titania capacitor-varistor ceramics, *Mater. Chem. Phys.* 74, 187 (2002).

FIELDS OF STUDY

Physics

ABSTRACT OF THE DISSERTATION

Nanofabrication, nanomagnetism and other applications of nanostructures

by

Chang-Peng Li
Doctor of Philosophy in Physics
University of California, San Diego, 2007
Professor Ivan K. Schuller, Chair

Nanostructured magnets have attracted great interest recently due to their new magnetic properties, which are completely different from those in the bulk, and their potential application in device miniaturization approaching the Tbit/in^2 recording density. In this thesis, we have fabricated sub-100 nm magnetic dots covering over 1 cm^2 area by electron-beam evaporation using self-assembled nanopores in anodized alumina as a shadow mask. Due to the large pattern coverage, and high degree of uniformity in both dot size and periodicity, magnetic measurements of such a dot array can be used to investigate the magnetism of a single dot of the average size. For Fe dots with a thickness of 20 nm, we find a transition from a single domain to a vortex state as the dot diameter is increased up to 60 nm. This single domain to vortex state transition has also been studied by the first order reversal curve method, which quantifies the magnetic phase fractions and distributions of vortex nucleation and annihilation fields. A magnetic vortex core size of 16$\pm$3 nm, which is close to or even smaller than the magnetic force microscopy (MFM) resolution, is measured by polarized neutron reflectivity measurements and verified by micromagnetic simulations.

In addition to applications in magnetic memory systems and ultrasmall magnetic field sensors, magnetic nanostructures can also be used as the artificial pinning centers for superconducting vortices. We have observed asymmetric superconducting flux pinning effects with first matching fields above 2 kOe. Most importantly, we find that the properties of a magnetic vortex can be imprinted into transport properties of adjacent Al superconducting thin films, with dots' magnetic reversal events imprinted and magnified in the superconducting behavior. Chemical sensing and biosensing in porous

alumina films, which exhibit more easily controlled pore sizes and higher chemical stability as compared to other porous materials, is studied using optical interferometry. The measured vapor capillary condensation and adsorption-desorption hysteresis is in qualitative agreement with theoretical models and a variety of simulations.

I

Introduction

Nanostructured magnets have recently attracted great interest due to their new magnetic properties, which are completely different from those in the bulks, as well as their potential applications in device miniaturization towards the Tbit/in^2 recording density. [1–4] In addition, nanoscale studies may shed light on the heavily investigated mechanism of exchange bias existing in ferromagnet (FM)-antiferromagnet (AF) bilayers. [5–9] Fabrication of sub-100 nm FM single layer and FM/AF bilayer nanostructures offers a great opportunity for research on fundamental magnetism and exchange bias effects at the nanoscale. [10] With the above motivation, my research dissertation is mostly focused on the fabrication and investigation of magnetic nanostructures.

In this work, we fabricate magnetic nanodots withs 25-130 nm size by using anodic porous alumina as a shadow mask for evaporative deposition (Chapter II). [11] With the pattern size comparable to the FM domain size, the transition from single domain to vortex state has been observed with increasing dot diameter. These are characterized by magnetic measurements (shown in Chapter III) and also theoretical calculations (shown in Chapter IV). Beyond the magnetic properties of magnetic nanostructures, the interaction between the magnetic dots (antidots) and the adjacent superconductor film is also investigated, as shown in Chapter V. In these systems, we have observed the conventional superconductor flux pinning effect. In addition, we also find for the first time that the properties of magnetic nanostructures can be imprinted into the adjacent superconducting layer. Finally, other applications of the porous alumina mask, in

the field of chemical and biosensors, are also given in Chapter VI. Below I will give a brief introduction of the superparamagnetic limit and patterned media, nanomagnetism, exchange bias, and superconductor flux pinning effect, which will be discussed in this thesis.

I.A Superparamagnetic limit and bit patterned media

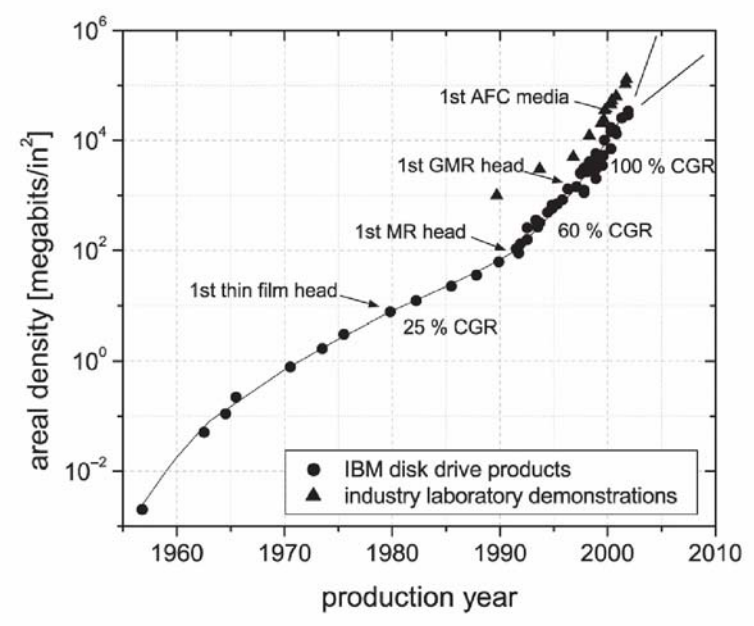

Figure I.1: Progress of magnetic recording density since invention of the first hard disk drive (Moser *et al.*, 2002).

Magnetic recording was first predicted by Oberlin Smith in 1888 Electrical World, and implemented on the first working magnetic recorder, called a telegraphone consisted of wires wrapped around a drum. Since then, various magnetic recording systems have been developed. Currently, magnetic data storage systems, especially the hard disk drives, have become the dominant information storage system. The first magnetic hard disk drive in the world, known as the "RAMAC", was released by IBM in 1956 with a storage density (total number of bits per lateral area) of 2 Kb/in^2. With the continuous growth of digitized world, the recording density has dramatically increased, with the maximum capacity doubling in recent years, as shown in Fig. I.1. To meet future demands, a magnetic storage system with higher capacity and reliability has to

be built. [12, 13]

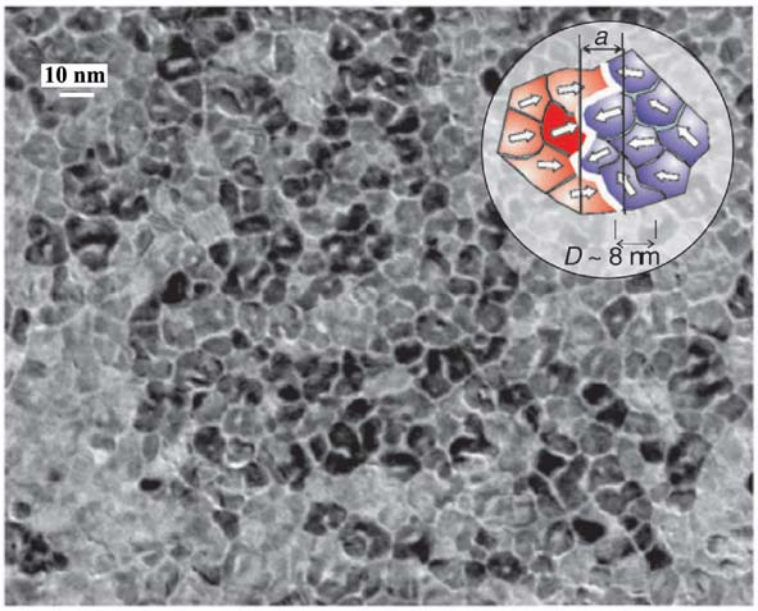

Figure I.2: Transmission electron microscopy image of a typical thin film CoCrPtB recording media. The inset schematically shows a magnetic transition meandering between the grains, which results in the transition noise (Moser *et al.*, 2002).

Current magnetic recording media is mostly made of magnetic thin films. [14,15] A typical thin film media is composed of Co dominant polycrystalline alloys, with a grain size of 15-30 nm. This grain structure results in two different media noises: the particulate noise, due to nonuniformity of grain sizes and magnetic anisotropy, and the transition noise, due to irregular zigzag-shape transition along the bit boundary, as shown in Fig. I.2. The signal to noise ratio (S/N), which directly affects the hard drive readability and liability, is roughly proportional to the square root of the grain number N within one single bit area. Thus, a sufficiently large number of grains are required for a reasonable S/N. For example, a single bit size in Seagate 250 Gb/in^2 recording media is approximately composed of 65 grains. A higher recording density demands scaling down of the bit size, which correspondingly results in a reduction of grain size while keeping the same grain number. [16] This reduction of grain size finally leads to a deterioration of recording stability due to thermal fluctuations, well known as the superparamagnetism.

To clarify the superparamagnetic limit, we take the recording process of a single grain as an example. The magnetic data is stored by saturating the grain with two

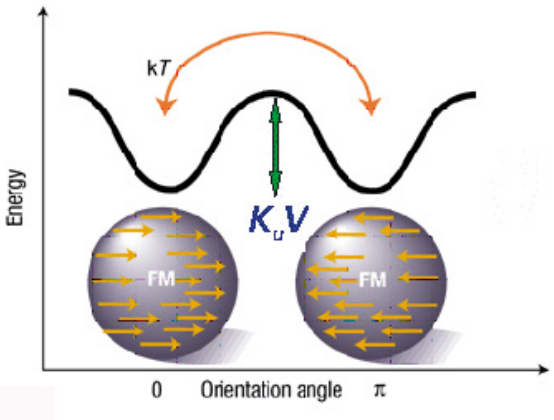

Figure I.3: Schematic of energy barrier used to stabilize magnetic states (Eisenmenger *et al.*, 2003).

opposite directions, as shown in Fig. I.3. These two magnetic states are stabilized by an energy barrier, which is proportional to the product of the magnetic anisotropy energy per volume (K_U) and the volume of the grain (V). The stability of a recording state is mostly characterized by the Néel-Arrhenius equation

$$t = t_0 exp(K_U V / k_B T) \tag{I.1}$$

where t is the magnetic reversal time, t_0 is a time constant with the value of $\sim 10^{-9} - 10^{-12}$ sec, and k_B is the Boltzmann constant. To keep the magnetic states stabilized for more than 10 years, the value of $K_U V / k_B T$ has to be larger than 40. For a typical spherical iron particle, with the anisotropy of $K_U = 4.8 \times 10^4\ J/m^3$, a minimal diameter of 19 nm is required to satisfy the 10-year magnetic stability. Due to this superparamagnetic limit, the achievable maximal recording density is approximately 100 Gb/in^2, assuming the conventional longitudinal recording geometry.

To overcome the superparamagnetic limit, several strategies have been implemented. One thought is to select magnetic materials with high anisotropy as the recording media. However, high magnetic anisotropy requires a corresponding large writing current to saturate the grains, which results in heating related problems in the write head and recording media. Another widely investigated method is that of perpendicular recording, in which magnetic information is recorded along the out-of-plane easy-axis, with the shape anisotropy enhanced with the reduction of lateral bit size. So far, the perpendicular recording has been proved a good candidate for a high density recording

system, and has been on the market since 2006. [17] However, theoretical calculation predicts that this perpendicular recording system can only push the density up to 0.5-1.0 Tb/in^2. [18] To reach a recording density well above 1 Tb/in^2, alternative recording methods must be employed.

Among them, one such candidate is bit-patterned recording media, which is composed of regular magnetic nanodot arrays. [18, 19] The high uniformity of dot size and anisotropy and precisely controlled dot locations prevent the recording media from developing the conventional media noises. Thus, one bit size can be composed of only one single dot, with magnetic saturation along either the in-plane or out-of-plane direction. Compared to the one bit area composed of 65 grains in conventional recording media, the recording density of bit-patterned media with the same dot volume as the average value of grains will be increased up to 65 times. Other methods that can be used to overcome the superparamagnetic limit are exchange coupling anisotropy from an adjacent antiferromagnetic layer, and heat assisted magnetic recording. It has been widely accepted that the heat assisted patterned media is a promising candidate for the next-generation ultra-density recording media. [18, 20]

I.B Nanomagnetism

I.B.1 Magnetic spin configurations in nanostructures

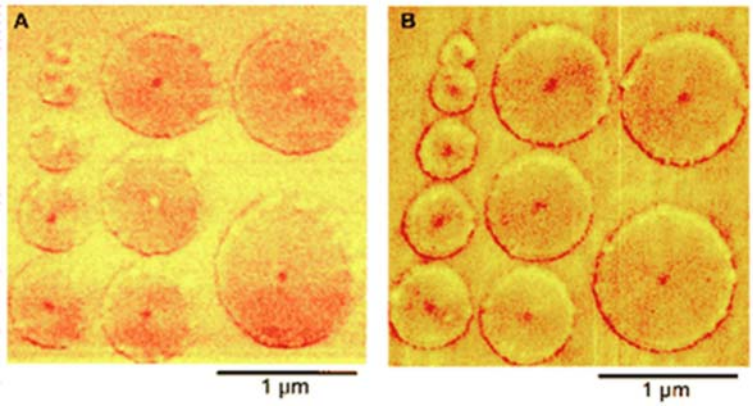

Figure I.4: The vortex state containing a vortex core observed in permalloy (Py) dots with a thickness of 40 nm and diameter ranging from 300 nm to 1 μm (Shinjo *et al.*, 2000).

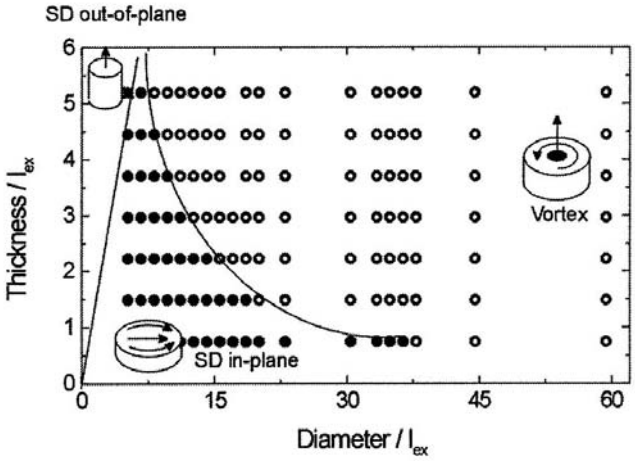

Figure I.5: Phase diagram of magnetic spin configurations as a function of dot diameter and thickness (Buda *et al.*, 2002).

Besides its potential application in magnetic recording systems, the fabrication and investigation of magnetic nanostructures is also essential towards a clear understanding of the basic mechanism behind nanoscale magnetism. Unlike the intrinsic magnetic properties, which are assumed constant as the bulk values with a length scale close to or above 1 nm, the extrinsic properties, such as magnetic hysteresis, domain structures, and coercivity, are very sensitive to the size of the magnets. In bulk magnets or magnetic thin films, multidomain structures are formed to reduce the magnetostatic energy. When the magnetic pattern size is comparable to the magnetic domain wall width ($\sqrt{K/M_s}$ for Bloch wall width) but still well above the superparamagnetic limit, the multi-domain structure becomes energetically unfavorable. Instead, the single domain state, in which all spins point along a same direction in order to reduce the domain wall energy, is exhibited within the nanometer scale magnetic pattern. For a circular magnetic nanopattern, the magnetic spins may curl up along the circular edge to reduce the magnetostatic energy, which results in a circular spin configuration known as vortex state. [21, 22] When the magnetic dots stay in the normal vortex state (demagnetized state), the spins curl in-plane around the center of the dot, pointing out-of-plane either up or down (vortex polarity) at the core, which has been directly viewed by magnetic force microscopy (MFM) [shown in Fig. I.4] and spin polarized scanning tunneling microscopy. [21, 23–25]

This circular spin configuration results in a reduced squareness of the hysteresis loop as well as reduced magnetic remanence, which negatively affects the conventional magnetic recording system as it requires high remanence for signal recovery. However, the closure of spins dramatically reduces dipole interactions between the neighboring patterns, and thus favors the increase of recording density. In addition, the chirality of in-plane spins surrounding the vortex core, which can be manipulated by cutting an edge from the dot and applying the magnetic field along the cut-edge, and the polarity of the vortex core can both be used for the information coding. Taking this into consideration, 2 bits of information can be recorded in one single dot with a vortex state, rather than the 1 bit of information obtained by conventional recording patterns, such as dots with a single domain state. Thus, the nanodots with a vortex state have been considered as a good candidate for magnetic recording (memory) patterns.

The critical size which corresponds to the transition from a single domain to a vortex state can be given as [2]

$$R_{sd} = \frac{36\sqrt{AK_1}}{\mu_0 M_s^2} = 36kl_{ex} \tag{I.2}$$

with $k = \sqrt{K_1/\mu_0 M_s^2}$ and $l_{ex} = \sqrt{A/\mu_0 M_s^2}$ where A is the exchange coefficient, K_1 is the magnetocrystalline anisotropy, M_s is the saturation magnetization, and l_{ex} is the exchange length, below which atomic exchange interaction dominates the magnetostatic fields. The static and dynamic properties of the single domain and vortex states have been widely investigated by both theoretical calculations (analytical calculations and numerical simulations) [26–29] and experimental measurements using Magneto-Optical Kerr Effect (MOKE) magnetometer, MFM, SP-STM, etc, [21,23–25] as shown in Fig. I.4. Phase diagrams of various spin configurations (Fig. I.5) have been given as a function of dot diameter and thickness. [28, 30] However, most of the studies were mainly focused on the scale well above 100 nm due to the fabrication limits and equipment resolution.

In this work, the magnetic dots fabricated using anodic porous alumina cover an area well above 1 cm^2, thus the magnetic properties of the nanodots array can be measured by various techniques, including SQUID and vibrating sample magnetometry, polarized neutron scattering, ferromagnetic resonance, etc. For these arrays, with dot periodicity about twice the dot diameter, the interaction between the dots can be ne-

glected. [31–33] Since the 10% standard deviation in the dot size and periodicity and 4 nm standard deviation in the dot height are relatively small, magnetic measurements of such a dot array can be used to investigate the magnetism of a single noninteracting dot. [11]

I.B.2 Micromagnetic simulation and Monte Carlo simulation

However, a clear image of magnetic spin configurations in a single dot cannot be completely understood by the magnetic hysteresis loops. Therefore, additional simulations, including Monte Carlo simulation and micromagnetic simulations, are crucial for the understanding of the nanomagnetism. In this work we perform micromagnetic simulations with the NIH OOMMF code, [34] which is based on the Landau-Lifshitz equation:

$$\frac{d\vec{M}}{dt} = -\left|\overline{\gamma}\right| \vec{M} \times \vec{H}_{eff} - \frac{\overline{\gamma}\alpha}{M_s}\vec{M} \times (\vec{M} \times \vec{H}_{eff}) \tag{I.3}$$

where $\vec{M}$ is magnetization, $\vec{H}_{eff}$ is the effective field, $\overline{\gamma}$ is the Landau-Lifshitz gyromagnetic ratio, and α is the damping coefficient. The effective field is defined as

$$\vec{H}_{eff} = \frac{-\partial E_{tot}}{\mu_0 \partial \vec{M}} = \frac{-\partial(E_{exch} + E_{anis} + E_{dem} + E_{zeem})}{\partial \vec{M}} \tag{I.4}$$

where E_{exch}, E_{anis}, E_{dem}, E_{zeem} are exchange energy, magnetocrystalline anisotropy, demagnetization energy, and Zeeman energy, respectively.

To simplify the calculations, the magnetic pattern, whose shape can be defined by an image file, is uniformly divided into rectangular cells with square in-plane cross-section. The lateral size of the cells has to be well below the exchange length, and thus all the spins inside the single cell always uniformly point along the same direction and can be resembled by a single spin. In this work, most of the calculations are based on a 2-dimensional model, which assumes cell thickness to be the same as that of the pattern. In addition, a 3-dimensional model, which allows for uniform cell thicknesses to differ from the pattern height, is implemented when the thickness dependence is calculated.

With this simplification, the exchange energy of the cell i can be given as $E^i_{exch} = \sum_i A_{ij}(\vec{m}_i \cdot (\vec{m}_i - \vec{m}_j))/(\Delta^2_{ij})$, where A_{ij} is the exchange coefficient between cells and regarded as a constant A in this work, j represents the six nearest neighbor

cells, $\vec{m}_i$ is the magnetization vectors, and Δ_{ij} is the distance between the cells. The demagnetization energy is obtained by calculating the self-magnetostatic (demagnetization) field of each cell with the assumption of uniform magnetization inside the cells. With the magnetization vectors of the cells preset as $\vec{m}_i$, the new magnetization vectors are obtained by the Landau-Lifshitz equation, which will be used as the initial magnetization vectors in the new calculation. The continuous calculation produces the final spin configurations when the control point, which can be either $d\vec{M}/dt$ or $\vec{M} \times \vec{H}$, is reached.

Monte Carlo simulations are carried out using the Metropolis algorithm that includes local dynamics and single-spin flip methods. [31,35–37] The internal energy E_{tot} of a single FM nanodot with N magnetic moments can be written as

$$E_{tot} = \frac{1}{2}\sum_{i \neq j}(E_{ij} - J_{ij}\widehat{\mu}_i \cdot \widehat{\mu}_j) + E_h \tag{I.5}$$

where the dipolar energy is

$$E_{ij} = \frac{\vec{\mu}_i \cdot \vec{\mu}_j - 3(\vec{\mu}_i \cdot \widehat{n}_{ij})(\vec{\mu}_j \cdot \widehat{n}_{ij})}{r_{ij}^3} \tag{I.6}$$

and r_{ij} is the distance between $\vec{\mu}_i$ and $\vec{\mu}_j$, and $\widehat{n}_{ij}$ is a unit vector along the direction that connects the two magnetic moments. J_{ij} is the exchange coupling, which is assumed to be nonzero only for nearest neighbors. $\widehat{\mu}_i$ is a unit vector along the direction of $\vec{\mu}_i$, and $E_h = \sum_{i=1}^{N} \vec{\mu}_i \cdot \vec{H}$ is the Zeeman energy. For a granular Fe, the parameters of $|\vec{\mu}_i| = \mu = 2.2\mu_B$, a lattice parameter a=2.8 $\mathring{A}$ and J=42 meV, give a Curie temperature for bulk Fe (1043 K), which is in good agreement with experiment. [38] The new orientation of the magnetic moment is chosen arbitrarily with a probability $p = min[1, exp(-\Delta E/k_B T)]$, where ΔE is the change in energy due to the reorientation of the spin, k_B is the Boltzmann constant, and T is the temperature. The number of Monte Carlo steps are changed until a fair agreement with the experimental results is obtained. Typically, we perform 3.4×10^5 Monte Carlo steps per spin for a complete hysteresis loop, and 5-20 different seeds for the random number generator, depending on the needs of each calculation. The calculations are simplified using a scaling technique that scales down the exchange interaction by a factor $x < 1$, i.e., $J' = Jx$, and the dot diameter and height given by $D' = Dx^{\mu}$ and $H' = Hx^{\mu}$, respectively, with $\mu < 0.55$. [31,35–37]

I.C Exchange bias

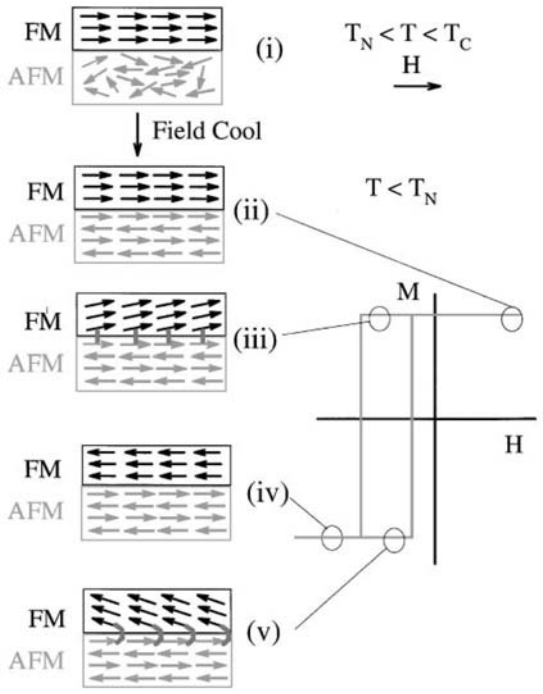

Figure I.6: Schematic of different spin configurations in ferromagnetic and antiferromagnetic layers for different stages of the magnetic hysteresis loop (Nogués *et al.*, 1999).

Exchange bias is a unidirectional anisotropy that exists at the interface between FM and AF materials, which was firstly discovered by Meiklejohn and Bean in Co particles surrounded by CoO shells. [39–41] When this FM/AF exchange-coupled system is field cooled through the Néel temperature of AF materials, the magnetic hysteresis loop of FM material is shifted, mostly in the direction opposite to the cooling field, due to a pinning force from the AF layer. [7, 8] This pinning effect can be used to stabilize the FM material along a particular direction and thus may be used to stabilize the magnetic recording media and thus overcome the superparamagnetic limit. [42–45] In addition, exchange coupling has also been used in the GMR (spin valve) read head, and magnetic sensors due to its capability of tuning FM magnetization. [46, 47] With this in consideration, exchange-biased systems have been widely investigated for the past two decades.

The mechanism of exchange bias was firstly explained by Meiklejohn and Bean

with the assumption that the spins in FM rotate coherently and the spins of the AF layer are frozen. The schematic of different spin configurations in FM and AF layers at the different stages of magnetic hysteresis loop is shown in Fig. I.6. By minimizing the total magnetic energy, the exchange bias was obtained as

$$H_e = \frac{2JS_{FM}S_{AF}}{a^2 M_{FM} t_{FM}} \tag{I.7}$$

where J is the interlayer exchange coefficient between FM and AF layer, $S_{FM}(S_{AF})$ is the spin of FM (AF) atoms, $M_{FM}(t_{FM})$ is the saturation magnetization (thickness) of FM layer, and a is the lattice constant. This model indeed explains many important results, such as the thickness dependence of the exchange bias values. However, this simplified model overestimates the interlayer exchange coupling with the calculated exchange bias by one order of magnitude as compared to the experimental value and cannot explain the striking enhancement of coercivity. To address the big discrepancy between the calculation and experimental values, more complicated models have been proposed. [48–54] However, to date, a clear understanding of the exchange bias is still missing.

I.D Pinning of superconducting vortices

Superconducting materials can be divided into two categories. For type-I superconductors, the transition from the superconducting state to the normal state occurs at a critical magnetic field H_c. Below that critical field, the materials stay in a superconducting state with the magnetic flux completely expelled from the superconductor. For type-II superconductors, complete flux expulsion is exhibited at a magnetic field below H_{c1}. However, when the magnetic field lies between the critical fields H_{c1} and H_{c2}, the flux is only partially excluded, with superconducting vortices forming and trapped at defects, as shown in Fig. I.7 (a). Here I want to emphasize that the vortices in superconductor are formed by supercurrents, rather than magnetic spins as in the magnetic vortex state. To avoid confusion, I will use "superconducting vortices" to indicate the vortices in superconductor, while using "vortices" or "magnetic vortices"to indicate magnetic vortex states. For the type-II superconductors, the motion of superconducting vortices due to weak trapping can result in increased resistance thus deteriorating the superconducting properties [Fig. I.7 (b) and (c)]. The flux pinning (also named as pinning of

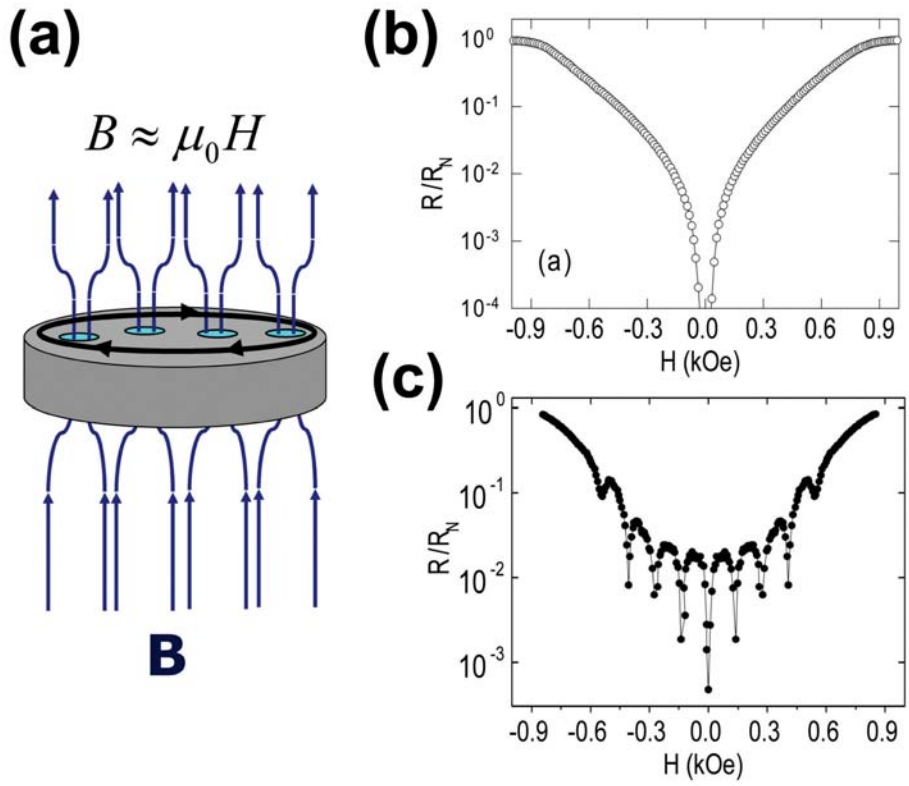

Figure I.7: (a) Schematic of the formation of superconducting vortices with penetration of magnetic flux into superconducting layer. Magnetoresistance measurements of superconducting film (b) without and (c) with patterned pinning centers, with dips representing the superconducting vortices pinning effect.

superconducting vortices) at the matching (commensurate) fields H_n by periodic dots or antidots can increase the stability of superconducting vortices and thus enhance the critical properties of superconductors, such as the critical current (a limiting current that a superconductor can support). [55–59] The first matching field H_1 with hexagonally distributed pinning centers, is equal to $4\Phi_0/(3\sqrt{3}l^2)$, where l is the lattice distance of the pinning centers. The flux pinning can be measured by either magnetoresistance measurements or by magnetometry as a function of external magnetic field, with the pinning fields corresponding to dips in resistance or peaks in magnetization, respectively.

The artificial flux pinning centers are mostly fabricated by electron beam lithography. The high cost and small pattern coverage of this technique limits its practical application for the enhancement of superconducting properties. In addition, the large pattern spacing results in the small matching fields, which limits the usage especially in the case of high magnetic field. With the above consideration, other nanofabrication techniques, such as self-ordering patterns and nanotemplates, have been implemented. In our work, the magnetic pinning centers (FM nanodots and antidots) are patterned through the use of self-ordered porous alumina masks, with a spacing of around 100 nm, which gives the first matching field above 2 kOe. Unlike the very small temperature range close to T_c with regular pinning centers fabricated with electron beam lithography, a broad temperature range of 4-6.5 K is obtained in our samples. [55, 60, 61]

The imprinting of the magnetic spin configurations of FM dots into its adjacent AF layer, with the exchange coupled system cooled through T_N of the AF material, has been intensively investigated. In this work, we have found that the properties of magnetic vortices can be imprinted into the transport properties of superconducting (Al) thin films. [62] This dramatically modifies the behavior of the superconductor, for which magnetoresistance and magnetization show simultaneously reversible or irreversible behavior. Detailed discussion will be shown in Chapter V.

II

Nanofabrication

II.A Introduction

A variety of methods have been used for nanofabrication, including electron beam lithography, optical lithography, and self-assembled nanostructures. The low throughput and high cost of electron beam lithography and focused ion beam lead to limited applicability for the fabrication of nanopatterns over a large area. Although optical lithography has high throughput, the smallest size of features that can be produced is limited by the long optical wavelength. [10,63–68] Nanoparticles with the size well below 10 nm have been fabricated through self-organization. However, this technique is only suitable for specific material systems. [69,70] Among many other nanofabrication methods, a promising technique is based upon using masks with sub-100 nm self-assembled pores. [71–75] Such masks, for example, can be fabricated by the anodization of aluminum under appropriate experimental conditions.

Anodic porous alumina has been widely investigated for more than 5 decades. However, due to its less controlled pore size and regularity, it was mainly used as a dielectric material, corrosion protection, and dye carrier. A great improvement with high self-ordered porous structure in large domains was first achieved by Masuda and Fukuda in 1995 [72] after a sufficiently long anodization under appropriate conditions. A two-step anodization process and prestamping have also been implemented to further improve the regularity of the pores. Although the basic formation mechanism of self-ordering of pores

is not completely understood, a simple explanation has been given by considering the interaction between the pores. Accompanying the formation of porous structures, the aluminum film is transformed into an aluminum oxide which has a reduced density, thus corresponding to a volume expansion. This volume expansion leads to repulsive forces between neighboring pores, thus promoting the formation of a hexagonal arrangement of nanopores. [76]

One important advantage of anodic alumina is its adjustable pore size and distance, both of which are proportional to the applied anodization voltage. By adjusting the anodization conditions, arrays of nanopores with uniform and tunable pore diameters ranging from 10 to 200 nm, and distances ranging from 20-500 nm have been obtained. In addition, the low cost, high stability, and large coverage (more than 1 cm^2) demonstrate the potential application of porous alumina (AlO_x) masks for nanostructure fabrication.

Previously, alumina membranes obtained from the anodization of thick (>100 μm) aluminum foils were mostly used for the fabrication of nanowires. [71, 77–83] These nanowires were grown by electrodeposition, which cannot be easily adapted for the fabrication of planar nanodots with controlled and uniform thickness. Moreover, this method requires transfer of the alumina membranes onto a substrate. Insufficient adhesion between the membrane and substrate, mask corrugation, delamination and general transfer problems reduce the reproducibility and uniformity of the fabricated structures. [45, 84–88] In this work, we fabricate magnetic nanodots using porous masks produced by anodization of Al films grown directly on substrates. This mitigates many problems related to transfer of membrane onto the substrate [11, 89]. By tuning the anodization parameters, dot arrays with average dot size and periodicity of 25-130 nm and 45-200 nm, respectively, have been fabricated. The highest nanopore density exceeds 10^{12} per square inch, thus approaching the holy grail of high-density magnetic media with a density of 1 Tbit/in^2. [18, 63, 90]

II.B Fabrication of self-ordered porous alumina masks on semiconducting and insulating substrates

II.B.1 Growth of Al films

Polished n-type (100) Si wafers (1-10 Ω·cm) are used as the semiconducting substrates. The n-type silicon substrate is moderately resistant to the acids used in processing and has a high enough conductivity to be used as an anode. [84] The substrate is first ultrasonically cleaned for 15 min using first acetone and then methanol. It is then etched in 25 wt% HF solution for 2 min, in order to remove the native silicon oxide and improve adhesion between the deposited aluminum film and substrate. All aluminum pellets in the four liners are pre-melted prior to film growth, thus minimizing the possibility of evaporating interfacial layers with different compositions during the liner changing. During deposition, the chamber pressure is 2-9$\times 10^{-7}$ Torr, and the substrate temperature is kept between 0 °C and 25 °C using liquid nitrogen. Typically, an aluminum film is deposited by electron beam (EB) evaporation (base pressure 1-2$\times 10^{-7}$ Torr) from 99.999% aluminum. An electron beam gun with four pockets is used. Fabmate-carbon-coated graphite liners (from Kurt J. Lesker) are used to isolate the aluminum pellets from the copper crucibles, so as to reduce thermal loss during evaporation and thus save electronic power. Optimally, each of the four liners has enough material to evaporate a 2.5 μm film, thus making 10 μm the maximum film thickness attainable without breaking vacuum. An evaporation rate of 2 $\mathring{A}$/s is maintained throughout the evaporation and monitored by a quartz crystal, which has been calibrated against small angle X-ray relectivity measurements. Any higher evaporation rate in our setup deteriorates the film quality by creating rougher surfaces and is thus avoided. The films grown this way with a thickness over 6 μm have a root-mean-square roughness of ∼10 nm as determined by atomic force microscopy (AFM). Thus, no extra processing is performed prior to anodization.

Alternatively, the aluminum film has also been grown in a sputtering system, which has a 10-in diameter aluminum target. However, these films are found to be very rough, which is probably due to too much heating from the hot plasma. In attempt to improve the aluminum film quality, the Si substrate is mounted onto a Peltier element,

with a liquid nitrogen trap used to remove the heat from Peltier element. The extra substrate-cooling significantly improves the film quality, resulting in an improvement of surface smoothness as well as a reduction of grain sizes. The anodization of some typical films show that the regular porous structures are similar to those of EB-evaporated films. However, the sputtering of aluminum is still not well controlled, due to unknown reasons. Improvement of the aluminum sputtering system is still in progress.

II.B.2 Anodization of aluminum film on Si substrate

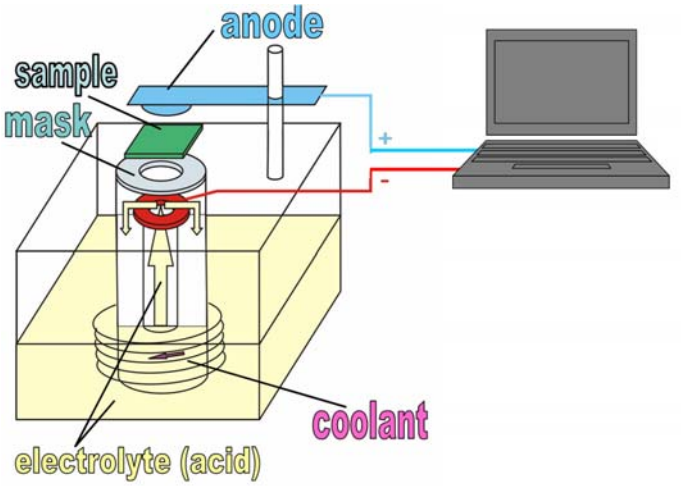

Figure II.1: Schematic of a computer-controlled aluminum anodization system.

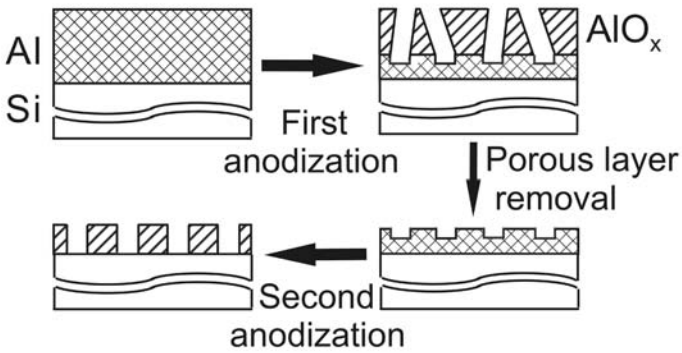

Figure II.2: Schematic of two-step anodization for aluminum films. (After Ref. [11]).

The aluminum films are anodized using an Buehler electropolisher. A schematic of the anodization system is shown in Fig. II.1. The temperature of the electrolyte (acid) solution is controlled using a water cooler. During the anodization process, the acid

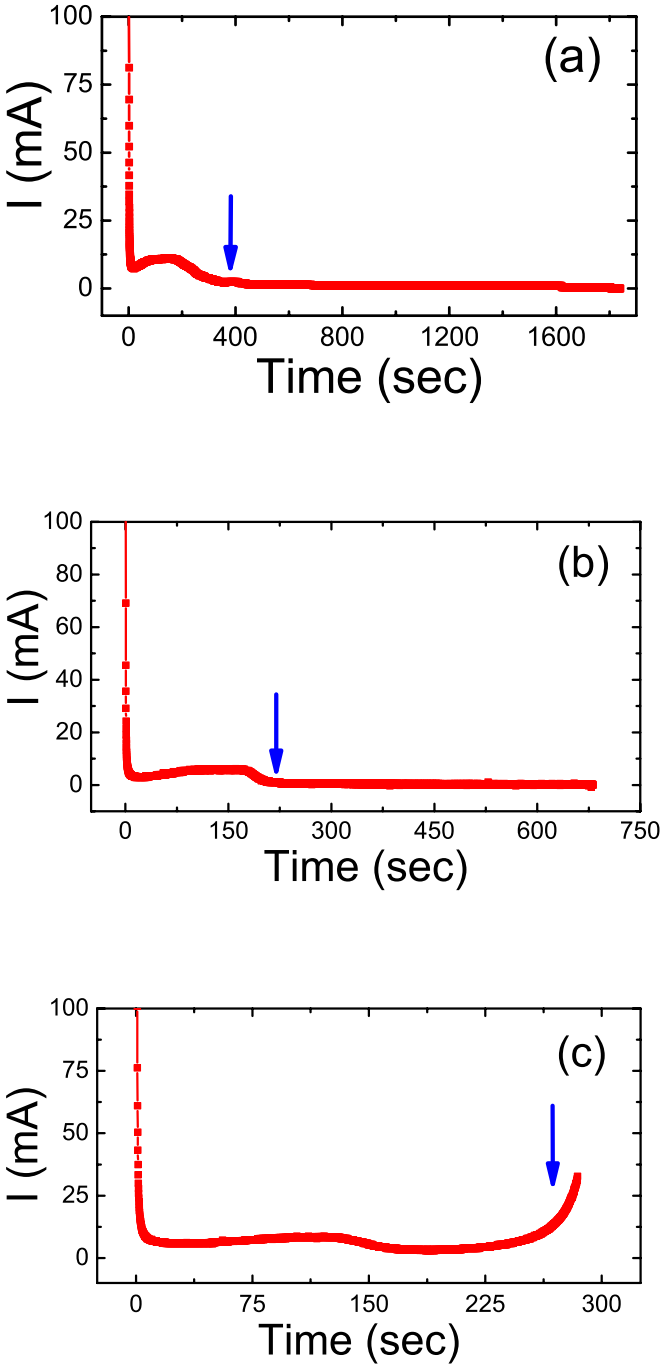

Figure II.3: Anodization current (anodized under 40 V in 0.3 M oxalic acid) as a function of time for aluminum films on top of (a) n-Si substrate, (b) titanium coated n-Si substrate, and (c) Au coated sapphire substrate. The blue arrows indicate that the anodization reaches the substrates.

Table II.1: Parameters of aluminum film anodization at 5 °C. (After Ref. [11]).

Electrolyte type (acid)	Concentration (M)	Anodization voltage (V)
Oxalic	0.05	60-80
Oxalic	0.3	20-60
Sulfuric	0.3	25
Sulfuric	1.7	19
Sulfuric	2.6	10, 15

solution inside the tank is pumped up to the aluminum film by using a magnetic rotor while a rubber O-ring is used both to avoid leakage of the acid solution and determine the area to be anodized. A constant voltage is applied perpendicular to the aluminum film with the Si substrate acting as the anode and a stainless steel plate as the cathode. Voltage and current are automatically monitored by a Labview program during the anodization process. Anodization of the aluminum film results in a transformation from Al to Al^{3+}, with 3 electrons leaving the aluminum film (ion current). The current efficiency, which is defined as the ion current divided by the total anodization current, was found to be close to 100%. [91, 92] Thus, the thickness of the anodized aluminum layer is proportial to the total amount of electrons leaving from the aluminum film, which can be calculated from the total charge passing through the anodized area. In order to obtain ordered porous patterns of different sizes and periodicities, anodization voltages of 10-80 V and various electrolytes (sulfuric acid or oxalic acid) are used, as summarized in Table II.1. [76,93–95] In addition to the anodization voltage and electrolyte, a variety of other factors affect pore ordering. Enhancement of pore self-assembly and improved ordering will accompany a slower anodization process, which is attained by keeping the electrolyte temperature at 5 °C. Continuous circulation of the electrolyte is used to keep its concentration and temperature uniform. [76]

To improve pore regularity and control the thickness of the final porous masks, we anodize the aluminum film in two steps, as shown in Fig. II.2. [85] In the first step, the film is anodized to a certain depth as controlled by the Labview program, which stops

the anodization process when the preset final thickness or time length is reached. After the first anodization, an aqueous solution with 6.0 wt% phosphoric acid and 1.8 wt% chromic acid at 60 °C is used to selectively remove the porous alumina layer, without affecting the aluminum layer below. As a result, a regular dimple pattern is obtained on the intact, non-oxidized aluminum layer. This aluminum layer, whose thickness is measured by a Dektak profilometer, determines the final mask thickness. This mask must be thick enough to ensure a good mask lift-off after deposition of the magnetic materials. However, if the mask thickness (pore height) is much larger than the pore diameter, the bottom of the pores becomes inaccessible to the evaporated materials ("shadow effect"). Details of the shadow effect will be discussed in Section II.C.1. In the second step, the patterned aluminum is anodized completely, using the same conditions as the first anodization process, with pores nucleating in the dimples. The ordering and control of the arrays obtained by this method are competitive with the much more expensive and technically demanding stamping process.

After anodization of the aluminum film, an alumina "barrier" layer, with a thickness proportional to the anodization voltage, is formed at the bottom of pores. The thickness of the barrier layer can be decreased by gradually reducing the anodization voltage to one forth of the original voltage after the anodization reaches the Si substrate, which is indicated by a sharp decrease of anodization current, as shown in Fig. II.3 (a). [78] Subsequent 5 wt% phosphoric etching acid is used to completely remove the alumina barrier layer. At the same time, the isotropic acid etching of alumina also reduces the thickness of pore walls and thus widens the pore diameter at 16 nm per hour, without affecting the pore periodicity. After removal of this barrier layer, additional phosphoric acid etching can be used to further widen pores. The pore opening at the top can also be reduced by depositing aluminum or silver on top of the alumina mask at an angle of 60° to the normal as confirmed by the reduced diameter of Fe dots fabricated using such a mask.

The porous alumina masks are imaged using scanning electron microscopy (SEM) after each stage of fabrication. An accelerating voltage of 20 kV and a probe current of 3.0×10^{-9} A are used to minimize charging of the sample while providing high enough resolution. Two SEM images of a typical porous alumina mask anodized at 40

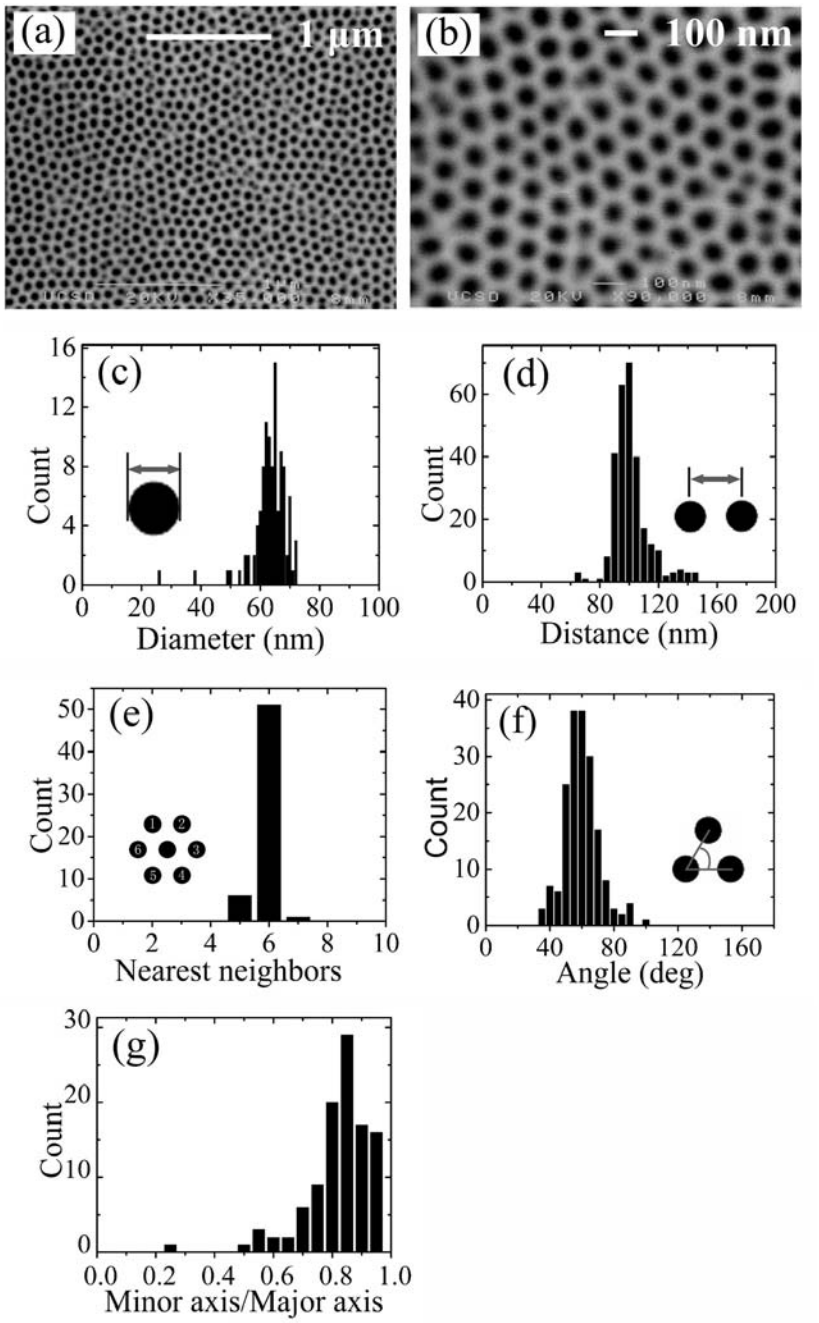

Figure II.4: Typical scanning electron microscopy (SEM) images of a porous alumina mask (40 V) with magnification of (a) 35,000 and (b) 90,000. Structural characterization of the porous mask shown in (b): (c) diameter distribution (average 63 nm, standard deviation 6 nm); (d) periodicity distribution (average 101 nm, standard deviation 12 nm); (e) number of nearest neighbor pores (5.97, standard deviation 0.18); (f) angle between the directions to nearest neighbor pores (59.9°, standard deviation 10.6°); and (g) pore shape analyzed by fitting the pores as ellipses. The average length ratio (minor axis/major axis) of the ellipses is 0.85, with standard deviation of 0.11. (After Ref. [11]).

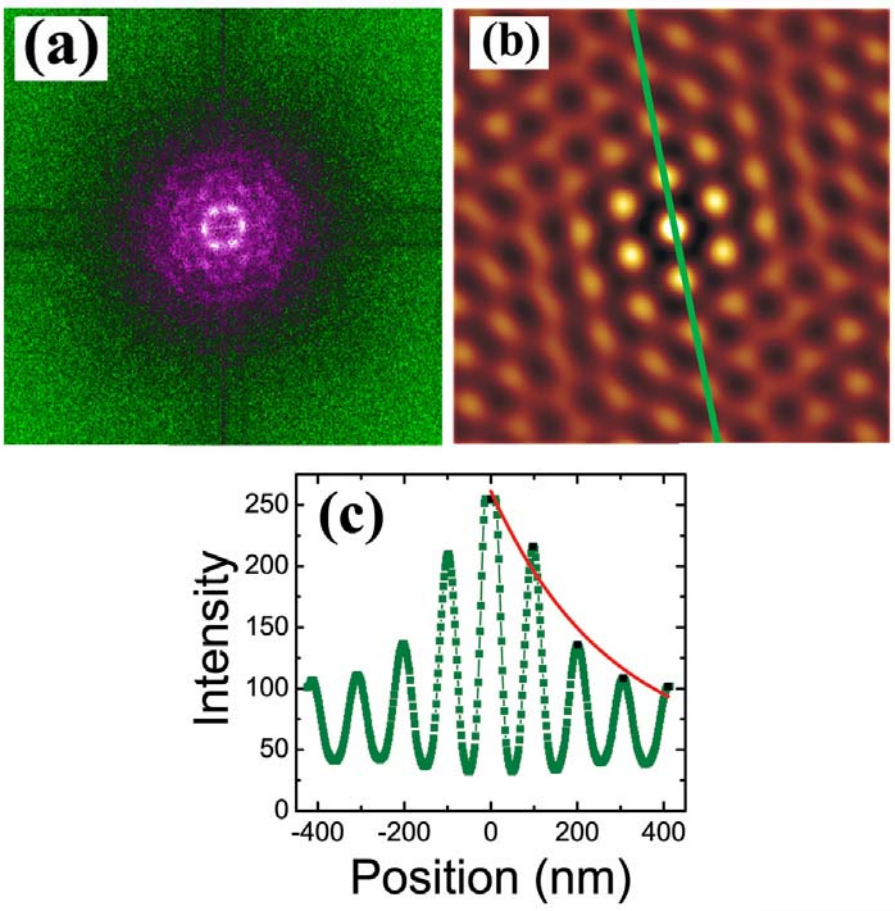

Figure II.5: (a) Fast Fourier transform (FFT) image of the porous structure shown in Fig. II.4(b). (After Ref. [11]). The pore periodicity (∼98 nm) calculated from the FFT spots distance agrees well with the result shown in Fig. II.4(d). (b) Auto correlation image of the porous structure and (c) plot profile along the green line. The peaks in the plot profile correspond to the periodicities of pores (103 nm). Red line is an exponential fit to the peak intensity, which shows the correlation length of the porous structure to be above 400 nm. Both the FFT image and auto correlation analyses are consistent with a hexagonal ordering for the nanopores.

V in 0.3 M oxalic acid are shown in Fig. II.4 (a) and (b). To characterize the porous structures, grayscale SEM images are converted to binary black-and-white images. The pixels with grayscale values exceeding a threshold are set to black, all others are set to white. The threshold values are manually chosen so that the black areas in the black-and-white images reproduce the pores in the original grayscale images. The NIH ImageJ software package is used to measure the sizes, shapes and center positions of the pores from the black-white images. [96] Pore periodicity (center to center distance between nearest-neighbor pores), number of nearest-neighbor pores and angles between directions to neighboring pores are calculated from the positions of pore centers. Analysis of the image in Fig. II.4 (b) shows that the pores have an average diameter of 63 nm and average periodicity of 101 nm, with a standard deviation for both less than 10% [Fig. II.4 (c) and (d)]. The number of nearest-neighbor pores (5.97) and angle between the directions to neighboring pores (59.9°) are consistent with a regular hexagonal arrangement [Fig. II.4 (e) and (f)]. Here, we do not include the pores close to the image boundary since they do not have all nearest neighbors within the image. The pore shapes are analyzed by fitting them as ellipses. The average length ratio (minor axis/major axis) of the ellipses is 0.85 [Fig. II.4 (g)].

The regularity of the porous structure is also investigated in frequency space with the 2-dimensional Fast Fourier Transform image (FFT) of Fig. II.4 (b) shown in Fig. II.5 (a). The six spots confirm a regular hexagonal arrangement of the pores. The pore periodicity (∼98 nm) calculated from the FFT spots distance is in excellent agreement with the result shown in Fig. II.4 (d). The porous regularity can also be characterized by the correlation length, [97] with the 2-dimensional auto correlation image shown in Fig. II.5 (b). The plot profile along the green line [shown in Fig. II.5 (b)] is given in Fig. II.5 (c), with peaks corresponding to the periodicities of pores (103 nm). The red line is an exponential fit to the peak intensity, which shows the correlation length of porous structure to be above 400 nm. Both the FFT image and auto correlation analyses are consistent with a hexagonal ordering of nanopores.

The porous mask in this work exhibits a lower degree of regularity than earlier self-supporting alumina membranes, due to a smaller thickness of the aluminum film used in this paper as compared to the several hundred micron thick aluminum foils used in

other references. [73,74,85] For thicker aluminum layers, a higher order and narrower pore size distribution is found for the same anodization conditions. Further improvements in ordering, required for industrial applications, can be achieved by additional pre-stamping of the aluminum surface. Considering the high cost of stamps made by electron beam lithography, we have tried to use the ordered nanodot arrays, fabricated by using the self-ordered porous alumina as shown in the next section, as the stamp. Fig. II.6 gives a typical stamp composed of SiO_2 dot arrays with a thickness of 100 nm. Successful pattern transfer from stamp to aluminum film surface has not been obtained so far, probably due to the weak stiffness of SiO_2. A thin layer of tungsten can be sputtered on top of the SiO_2 dots in order to improve the stamp stiffness. [84]

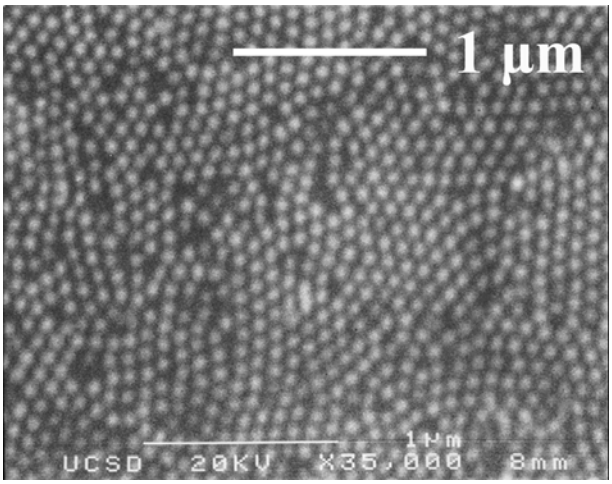

Figure II.6: Typical SEM image of a stamp composed of 100 nm-thick SiO_2 dots, fabricated by using the porous alumina mask anodized at 40 V.

During the anodization process, pore periodicity and diameter can be manipulated by tuning the anodizing voltage. To achieve alumina masks with much larger pore size and periodicity, the aluminum films must be anodized at much higher voltages and in a weaker acid solution, such as weakly concentrated oxalic acid or phosphoric acid solution. However, anodization with a high voltage and similar current produces more electronic heating, which can result in the peeling off or over heating of the aluminum film. So far, we have succeeded in the anodization of an aluminum film under up to 80 V in 0.05 M oxalic acid solution. Unfortunately, the alumina masks obtained from the anodization under 60-80 V do not exhibit good regularity. To obtain masks with

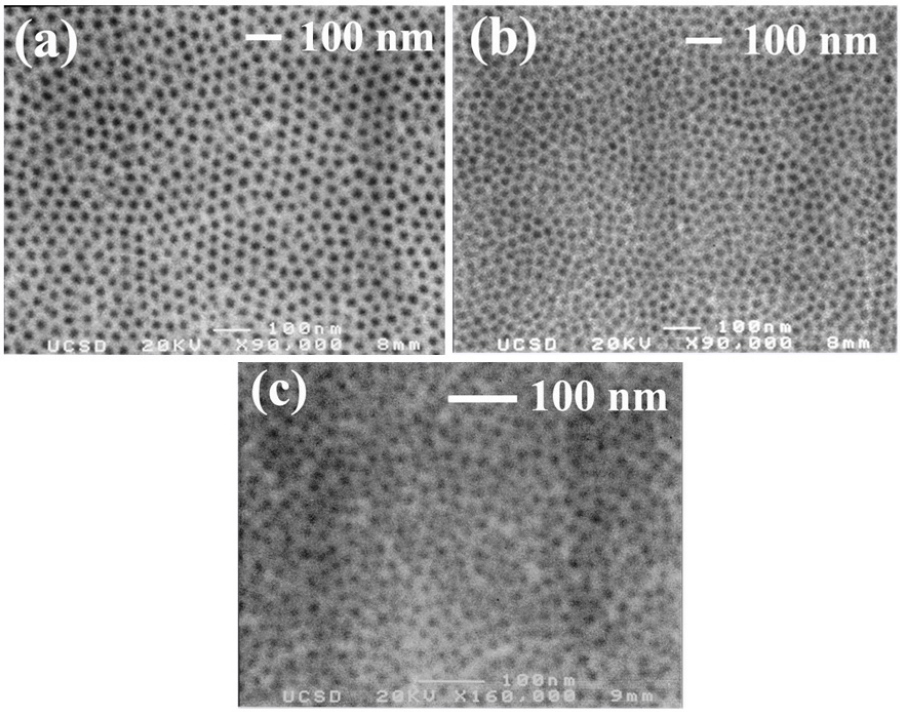

Figure II.7: Typical SEM image of an alumina mask anodized at (a) 25 V in 0.3 M sulfuric acid, (b) 19 V in 1.7 M sulfuric acid, and (c) 10 V in 3.9 M sulfuric acid. The pore density in (c) exceeds 10^{12} per square inch. (After Ref. [11]).

Table II.2: Summary of structural characterization of nanopore arrays in anodized alumina. (After Ref. [11]).

Eletrolyte acid	Anodization voltage (V)	Diameter (nm)	Periodicity (nm)	Number of nearest-neighbors	Angle between directions to nearest-neighbors (deg)
0.3 M Oxalic	40	63±6	101±12	6.0±0.2	59.9±10.6
0.3 M Sulfuric	25	29±6	59±7	5.9±0.6	58.8±10.4
1.7 M Sulfuric	19	24±3	43±6	5.9±0.6	58.1±12.8

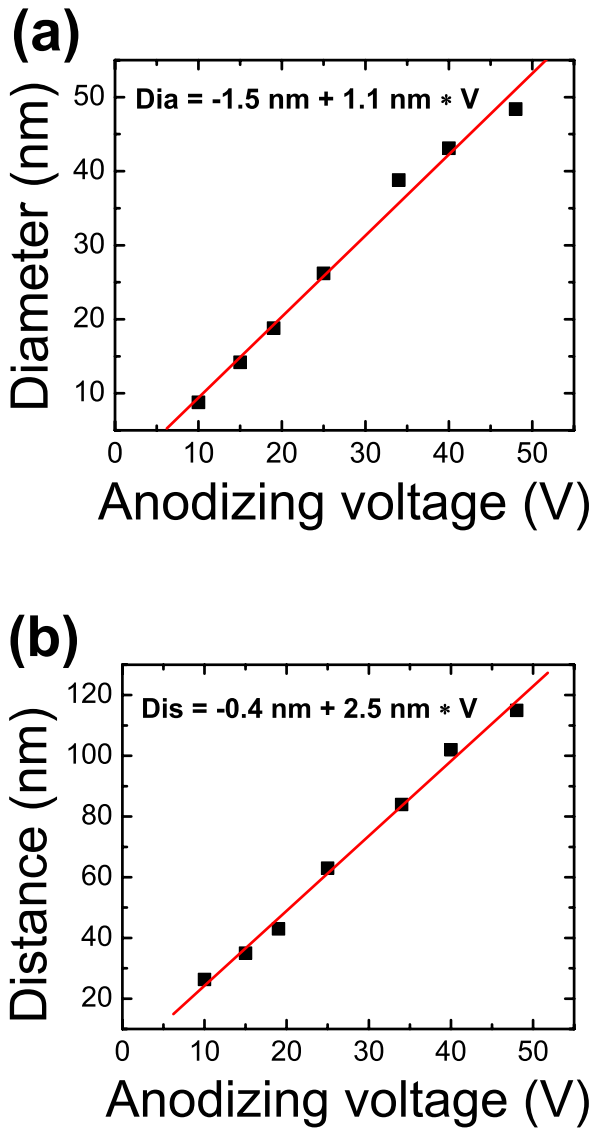

Figure II.8: (a) The pore diameters and (b) pore periodicities of anodic alumina before the pore widening process, which are proportional to the anodizing voltage. The linear fits (red lines) of pore periodicities and pore diameters are plotted as a function of the anodization voltage.

small pore sizes, a low anodization voltage and strong acid solution, such as concentrated sulfuric acid, are used. Despite its low reactivity to acid etching, the n-type Si is etched slightly by the concentrated sulfuric acid solution, which causes the anodized alumina mask to peel off. Etching of the substrate has been confirmed by anodizing two identical aluminum films in oxalic acid and sulfuric acid. After the anodization reaches the substrate, the mask anodized in sulfuric acid peels off with further anodization ("over-anodization"). Under the same anodizing voltage and temperature, the mask remains intact when over-anodized in oxalic acid. Because of this, anodization with sulfuric acid must be stopped as soon as it reaches the silicon substrate. Fig. II.7 shows typical SEM images of porous alumina masks as obtained from aluminum anodization under 25 V, 19 V, 15 V, and 10 V, respectively. With the anodization parameters in Table II.1 and subsequent pore size adjustments, porous masks with pore diameters of 10-135 nm and periodicities of 20-200 nm are fabricated. The results of structural analyses of typical alumina masks anodized in 0.3 M oxalic, 0.3 M sulfuric and 1.7 M sulfuric, at constant anodization voltages of 40 V, 25 V and 19 V respectively, are shown in Table II.2. The pore periodicities and pore diameters before the pore widening process are proportional to the anodizing voltage, as shown in Fig. II.8. Linear fit of the pore periodicities and pore diameters as a function of the anodization voltage gives

$$Distance = -0.5nm + 2.5nm \times V \quad \text{(II.1)}$$

$$Diameter = -1.5nm + 1.1nm \times V \quad \text{(II.2)}$$

where V is the anodizing voltage. Masks with a pore periodicity of 20 nm [Fig. II.7(c)] exhibit pore densities in excess of 10^{12} per square inch, which suggest potential application of this fabrication method towards patterning for ultrahigh density recording media.

II.B.3 Anodization of aluminum film on insulating substrates

In the above section, I have shown the procedures and results of anodization of an aluminum film directly deposited on the Si substrate. Alternatively, a titanium layer can be deposited first as a buffer layer to further improve adhesion between the aluminum film and Si substrate. However, when the anodization reaches the interface

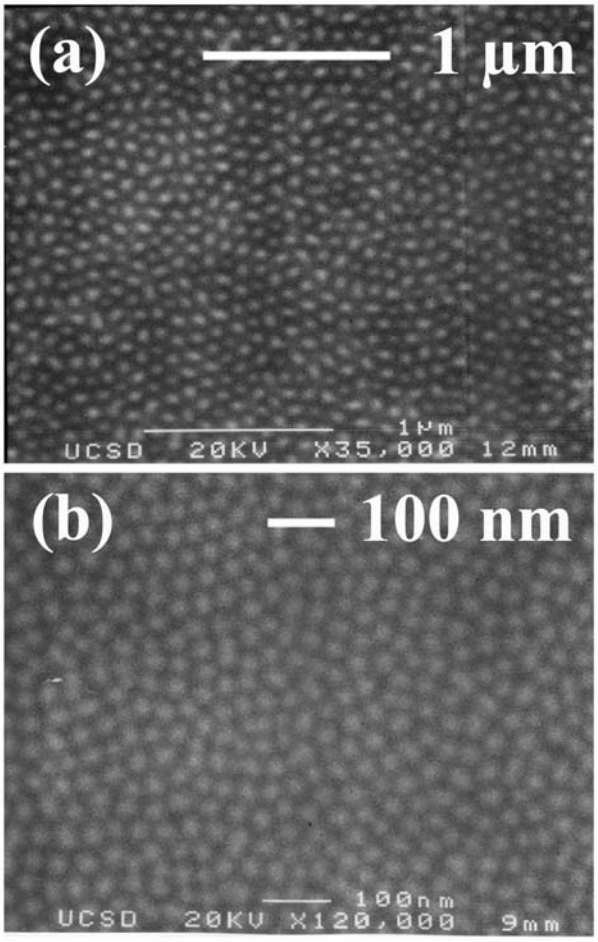

Figure II.9: Typical SEM images of TiO_x patterns after removal of the alumina layer anodized at (a) 40 V, and (b) 19 V.

between aluminum and titanium, it continues into the titanium layer, which results in the formation of titanium oxide pillars on top of a continuous titanium oxide layer extending into the aluminum oxide pores. [98, 99] Fig. II.9 shows two typical titanium oxide patterns after removal of the alumina masks. This patterned titanium oxide can be used as an etching mask for fabrication of magnetic nanodots, which will be shown in Section II.C.3.

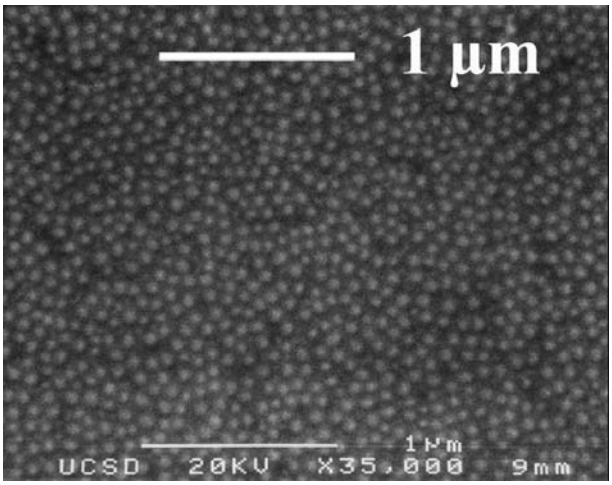

Figure II.10: Typical SEM image of Fe dot array on top of Au-covered sapphire substrate.

To fabricate alumina masks on insulating substrates, a 200 nm aluminum film is directly deposited on a bare sapphire substrate. The aluminum film is anodized, with the aluminum itself acting as the anode. However, after deposition of magnetic materials through the alumina mask, the mask cannot be removed using the procedure shown above, due to unknown reasons. In addition, the slight nonuniformity of the electric field, due to the circular shape of the cathode, results in a slower anodization in the middle of O-ring. Thus, the anodization of the aluminum film is first completed around the edge, which results in the electrical isolation and prohibits the further anodization of the thin layer of unanodized aluminum within the center of the O-ring.

To avoid the above problem associated with mask lift-off, the substrate is first coated with a 20 nm-thick gold film, with a 2.5-20 nm-thick titanium buffer layer between the gold and Si substrate in order to improve adhesion of the gold film. The gold film is then used as the anode in the aluminum anodization process. [89, 100] To avoid mask delamination, the anodization process must be stopped as soon as it reaches the gold film,

which is indicated by a sharp increase in the anodization current, as shown in Fig. II.3 (c). This current increase becomes less abrupt for thicker aluminum films, probably due to nonuniformity of the anodization rate over the film surfaces. Thus, it is more difficult to determine the time at which the anodization process reaches the gold film for thicker aluminum films. Such a limitation results in a lower degree of regularity as compared to that of the masks on Si substrates. However, by using this porous alumina as the evaporation mask, we have been able to successfully fabricate FM dot arrays on top of gold films (shown in Fig. II.10).

II.C Fabrication of magnetic dot arrays using porous alumina masks

II.C.1 Fabrication of ferromagnetic dots utilizing electron beam evaporation and subsequent mask lift-off

In this section, we discuss fabrication of a single FM layer and FM/AF bilayer nanodot arrays using porous alumina masks. Prior to deposition of the magnetic materials, the porous alumina mask is baked in situ at 500 °C for 1 hour to remove water and hydrocarbons from within the pores. In order to fabricate a single layer of FM dots, electron beam evaporation is used to deposit 20-100 nm of a ferromagnet material (Fe, Ni, $Fe_{20}Ni_{80}$) through the porous mask onto a substrate, at a rate of 1 $\AA$/s and a substrate temperature of 200 °C. Afterwards, the substrate temperature is lowered to 150 °C, at which a 5-8 nm-thick silver capping layer is deposited so as to protect the dots from oxidation. After removal from the evaporator, the porous alumina mask is lifted off in either 10 wt% NaOH solution at room temperature for 2 minutes or a mixture of 6.0 wt% phosphoric acid and 1.8 wt% chromic acid at 60 °C for 15 minutes, leaving a single layered FM dot array (Fig. II.11). In order to check adhesion of the FM dots to the Si substrates, we sonicated a typical Fe dot sample in acetone for 10 minutes. SEM images of this sample indicate that the dots remain intact, which confirms the robustness of FM dot arrays on a Si substrate as fabricated by this method.

It should be noted that while the top of the FM is protected, its sides are exposed and thus may be oxidized. For continuous FM films or dots that are much larger

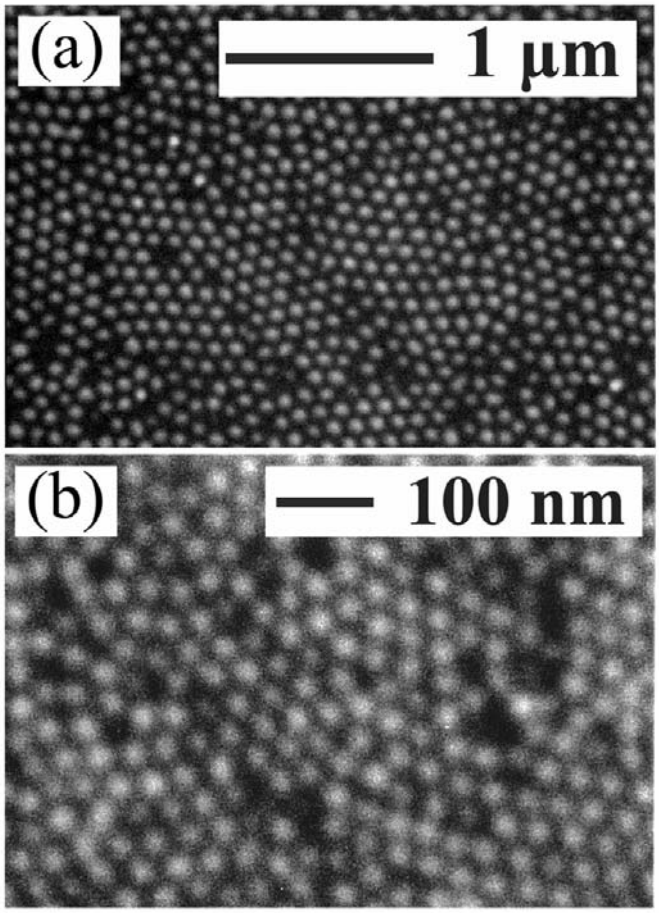

Figure II.11: (a) Typical SEM image of an Fe dot array (fabricated using an alumina mask anodized at 40 V) with average diameter and periodicity of 67 nm and 104 nm, respectively. (b) Typical SEM image of an Fe dot array (fabricated using an alumina mask anodized at 25 V) with average diameter and periodicity of 32 nm and 63 nm, respectively. (After Ref. [11]).

than 100 nm, formation of magnetic metal oxide has only a small effect on the magnetic properties, such as the exchange bias. However, the magnitude of the nanodots' exchange bias is proportional to their oxidized surface to volume ratios, i.e., the magnitude of exchange bias increases as the dot size decreases. Thus, the effect of the oxidation cannot be neglected for sub-100 nm magnetic nanodots. The size dependence of oxidation induced exchange bias will be detailedly discussed in detail in Chapter III. In order to avoid dot oxidation, a thick aluminum layer is deposited *ex situ* immediately after ion milling or mask lift-off. With this protective layer, there is no measurable effect attributable to FM oxidation, suggesting that the amount of metal oxide formed in this case is negligible.

As mentioned earlier, porous alumina masks used for fabrication of dot arrays should be thin enough to avoid the shadow effect. To study the dependence of the shadow effect on mask thickness, Fe is deposited through porous alumina masks with 65 nm diameter pores and thicknesses of 1 μm and 0.4 μm. After mask lift-off, few dots are found on the sample fabricated from the 1 μ-thick alumina mask, while a typical ordered dot array is found with the 0.4 μm-thick alumina mask. Thus, to fabricate dots using a porous mask, an appropriate pore aspect ratio (diameter/thickness) must be chosen. For example, a 0.12 μm or thinner alumina mask must be chosen to fabricate 20 nm diameter dots, while a 0.4 μm alumina mask can be used to obtain 65 nm diameter dots. As discussed earlier, the porous mask thickness is determined by the alumina layer thickness remaining intact after the first anodization. It should be noted that nonuniformity of the anodization rate over the aluminum surface complicates fabrication of thin masks from very thick aluminum films. Hence, the highest density of the dot arrays reproducibly produced so far is about 0.4×10^{12} per square inch, despite the highest nanopore density being 1×10^{12} per square inch.

The nanodot arrays are characterized by analyzing SEM images (see in Fig. II.11), which are taken before the array is protected by the thick aluminum film, in the same fashion as the nanopore arrays. These analyses show that the fabricated nanodots are circular and have a hexagonal arrangement with narrow size and periodicity distributions. Comparison of the size and periodicity distributions of the porous mask to the distributions for the dot array fabricated with this mask indicates a good pattern transfer.

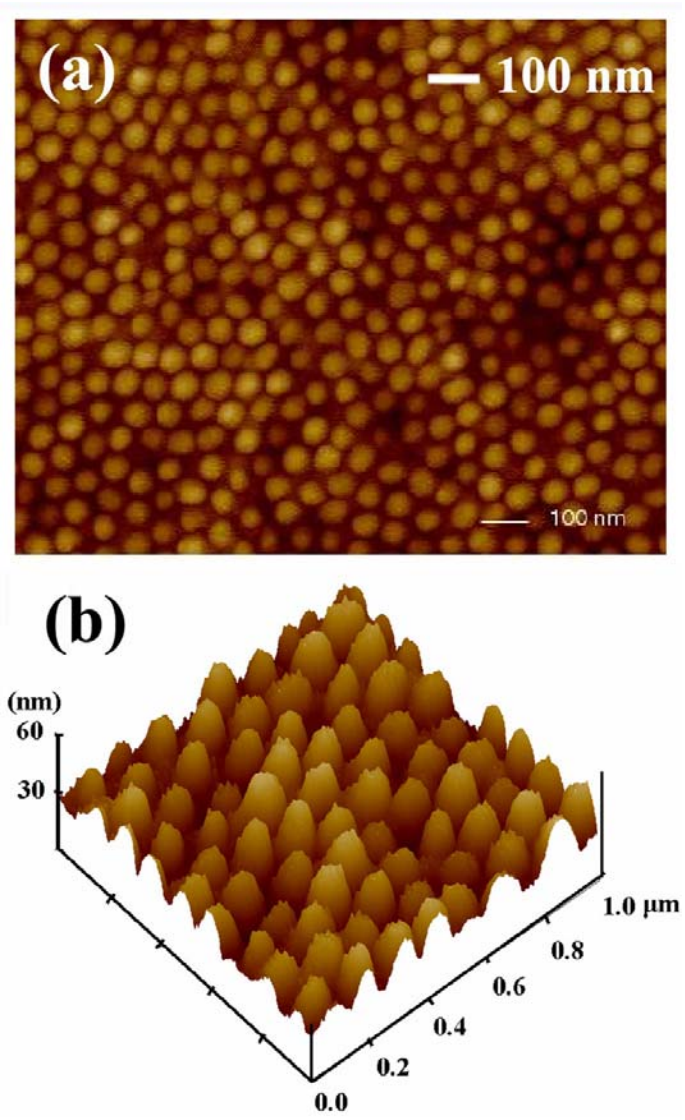

Figure II.12: Typical (a) 2-dimensional and (b) 3-dimensional atomic force microscopy (AFM) images of an Fe dot array (fabricated using an alumina mask anodized at 25 V). The standard deviation for the dot height is about 4 nm.

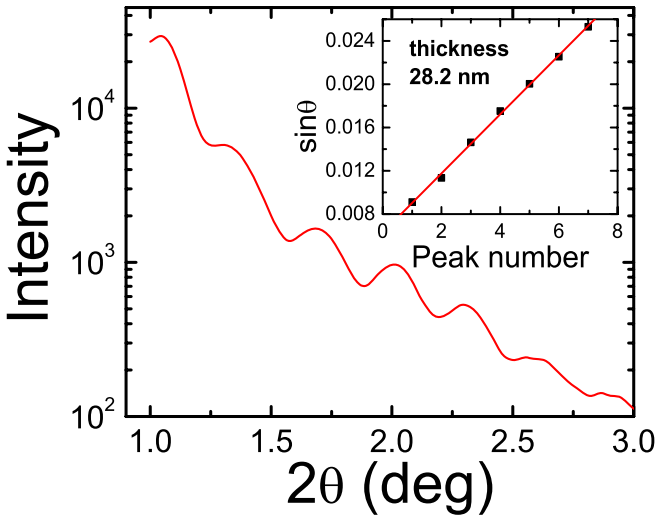

Figure II.13: Small angle X-ray reflectivity measurement of sample presumed to consist of 30 nm-thick Ni dots. Inset shows linear fit of the peak positions as a function of the peak number.

Nanodot structures are also investigated by AFM (Veeco Scanning Probe Microscope), which yields close agreement to that of SEM analyses. Moreover, AFM measurement shows that the standard deviation for the dot height is about 4 nm (Fig. II.12). The average dot height can be measured using small angle X-ray reflectivity (SAXR) measurement. Fig. II.13 shows the SAXR result of a typical sample with presumably 30 nm-thick Ni dots, with the peak position ($sin\theta$) versus peak number shown in the inset. An average dot height of 28.3 nm is calculated from the slope of the linear fit, as shown in the inset. The thickness of a Ni film co-evaporated with the Ni dot sample is also measured by SAXR, giving a thickness (27.1 nm) close to the average dot height. Alumina masks with various sizes and periodicities enable the average dot diameter and periodicity to be tuned from 25 nm to 130 nm and from 45 nm to 200 nm, respectively. For these arrays (20 nm-thick dots with dot periodicity about twice of the dot diameter) the interaction between the dots can be neglected. [31–33] Since the 10% standard deviation in the dot size and periodicity and 4 nm standard deviation in the dot height are relatively small, magnetic measurements of such a dot array can be used to investigate the magnetism of a single noninteracting dot.

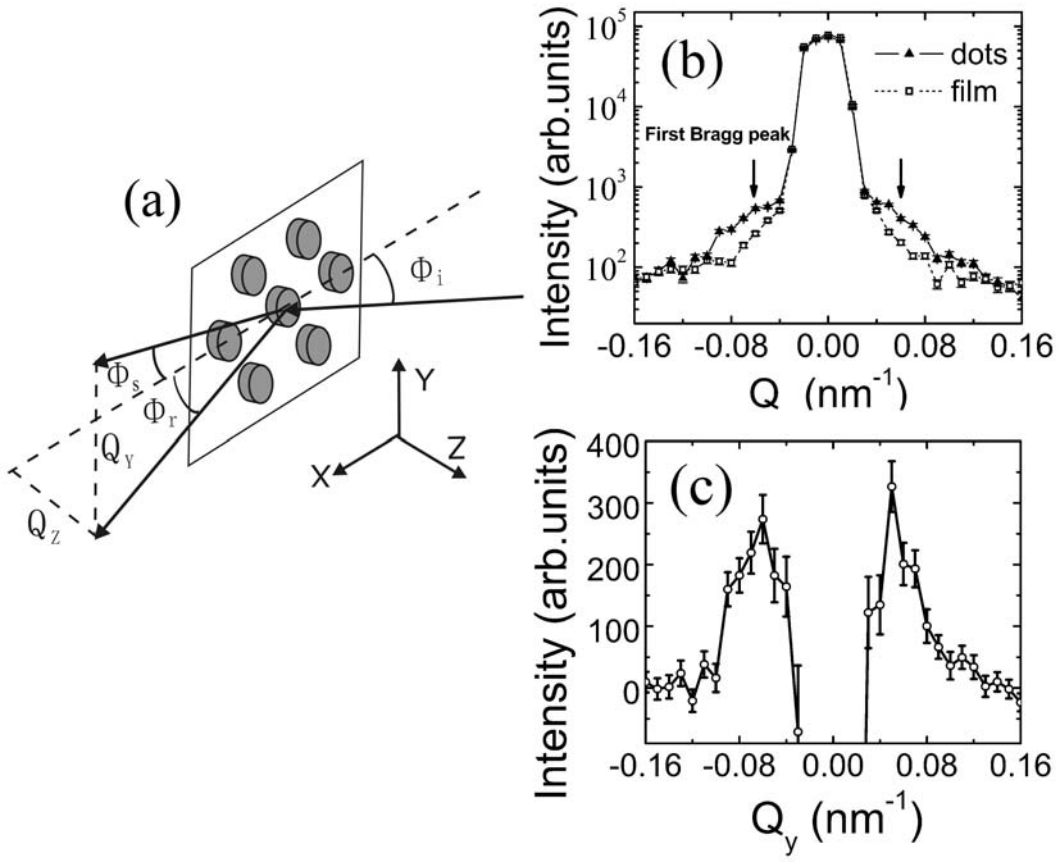

Figure II.14: (a) Geometry of grazing incidence small angle neutron scattering measurement. (b) Scattering intensity as a function of the momentum transfer vector Q_y for an array of Fe dots (20 nm height, 65 nm average diameter) (solid triangles), and a continuous Fe film of the same thickness (open squares). The statistical errors are given by the square root of the scattering intensity. Due to their small sizes, most of the error bars are covered by symbols. (c) Difference between the scattering intensity of the dots and that of the film. (After Ref. [11]).

Since these nanodot arrays cover a macroscopically large area (over 1 cm^2), their magnetic properties can be investigated using techniques that require relatively large quantities of material including SQUID, vibrating sample magnetometry, polarized neutron scattering, ferromagnetic resonance, etc. For example, grazing incidence small angle neutron scattering (GI-SANS), performed at the Laboratoire Leon Brillouin (Saclay) spectrometer PAPOL with 8 $\AA$ wavelength, is used to analyze the microstructure of the samples. To our knowledge, this is the first neutron scattering experiment performed on sub-100 nm magnetic dots. The geometry is such that the scattering plane (X, Z) is formed by the transmitted and reflected beams [Fig. II.14 (a)]. Fig. II.14 (b) shows the scattering intensity as a function of the momentum transfer vector Q_y for a continuous 20 nm-thick film and a 20 nm-thick Fe dot sample with an average diameter of 65 nm. The statistical errors are given by the square root of the scattering intensity. Due to their small sizes, most of the error bars are covered by symbols. The peak at $Q_y = 0$ corresponds to the specular reflection and appears in the neutron scattering for both dots and film samples. The extra shoulders appearing for the dots are the first Bragg peaks due to spatial ordering of the dots. These peaks are even more evident in Fig. II.14 (c), which shows the difference between the scattering intensity of the dots as opposed to that of the film. The dip at the specular angle, $Q_y = 0$, [not fully shown in Fig. II.14 (c)] is due to the transfer of the scattering intensity from the specular reflection peak into the Bragg peaks in the case of the dots. Positions of these Bragg peaks correspond to a dot periodicity of $\sim$100 nm. It is noteworthy that this value of periodicity is observed from the entire, $\sim$2.5 cm^2 in area, sample. This periodicity is in good agreement with that obtained from the SEM image (104 nm), indicating that variation of the periodicity over the sample area is small. This also validates that our characterization based upon SEM images of small areas is indicative of the entire sample.

II.C.2 Fabrication of ferromagnetic/antiferromagnetic bilayer dots utilizing electron beam evaporation and dry etching

Arrays of FM/AF (AF/FM) bilayer dots for nanoscale exchange bias studies are fabricated using about 300 nm-thick porous alumina masks as described above. Similarly to growth of the FM dots, 30-50 nm AF (FeF_2) is deposited at a rate of 1 $\AA$/s with the

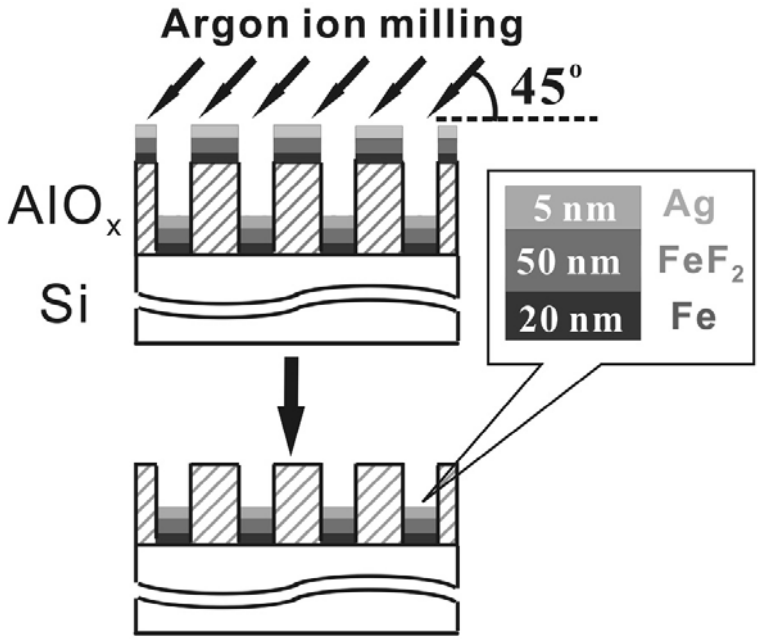

Figure II.15: Schematic of fabrication process for ferromagnetic/FeF_2 exchange-biased bilayer nanodot array using argon-ion milling at an angle of 45°. (After Ref. [11]).

substrate kept at 250 °C, after (FM/AF) or before (AF/FM) the deposition of 20 nm of FM (Fe, Ni, $Fe_{20}Ni_{80}$). Finally, a 5-8 nm thick silver capping layer is deposited in order to protect the dots from oxidation. The bilayer magnetic materials lay both on top of the porous alumina mask and at the bottom of pores. The layers on top constitute a magnetic network or antidot structure. The hole sizes of the network can be tuned with the appropriate alumina pore widening, without affecting the hole distance. To study the magnetic properties of FM/AF (AF/FM) bilayer dots, this magnetic network has to be removed without affecting the materials at the bottom of pores. However, the aforementioned mask lift-off procedure cannot be used for the FM/FeF_2 bilayer dot arrays because FeF_2 is soluble in the aqueous etchant solution. To overcome this, all the magnetic layers on top of the mask are removed using 500 eV argon-ion milling (DC Kaufman ion gun) at an angle of 45°, as sketched in Fig. II.15. The sample is rotated in-plane to ensure uniform milling. After ∼8 minutes ion milling, all the materials on top of the mask and roughly the top 50 nm of alumina mask are removed, but the materials at the bottom of the pores, protected by the alumina mask, are left intact. This is accomplished by ensuring that the distance between the top of the alumina mask

and the surface of the magnetic material at the bottom of pores is larger than the pore diameter during the entire ion milling process. In this fashion the magnetic bilayer dot array is embedded within the nonmagnetic porous alumina masks.

To verify the successful fabrication of the FM/FeF_2 bilayer dots, the sample is measured using SQUID magnetometry both before and after argon-ion milling. The measured magnetic moment in saturation is proportional to the FM volume. The ratio of the FM volume on top of the mask to its total volume should be equal to the ratio of the area outside the pores to the total mask area (typically around 70%), thus reduction of the magnetic moment after the ion milling by the same proportion confirms successful removal of the magnetic layers from the top of the mask. As the sample is ion milled further, no additional reduction in the magnetic moment and exchange bias are found. This indicates that the ion milling affects neither the FM nor the FeF_2 at the bottom of the pores.

When the magnetic dots are fabricated using a mask lift-off, the phosphoric acid etching, which occurs prior to deposition of the magnetic materials, should be long enough to remove the alumina barrier layer remaining at the bottom of pores. Otherwise, the dots will also be removed during the subsequent mask lift-off. However, with the argon-ion milling, this alumina barrier layer does not constitute a problem. Thus, shorter etching times resulting in smaller pore diameters can be used. Because of this, the range of dot diameters that can be fabricated with the same periodicity is much wider.

II.C.3 Fabrication of magnetic nanodots utilizing patterned titanium oxide etching mask

As mentioned in Section II.B.3, patterned titanium oxides are obtained by anodization of titanium buffered aluminum films. To make use of this titanium oxide pattern as the etching mask, we first deposit the FM single layer or AF/FM bilayer films, followed by a 5 nm-thick SiO_2 layer to protect the magnetic films from chemical etching. After the complete anodization and porous alumina lift-off, patterned titanium oxides formed on top of the SiO_2 layer can be used as dry etching masks. Several etching methods have been tried, which include Ar^+ milling with normal incidence, Ar^+ milling at an angle of 45°, and Reactive Ion Etching with an argon source. Currently we have

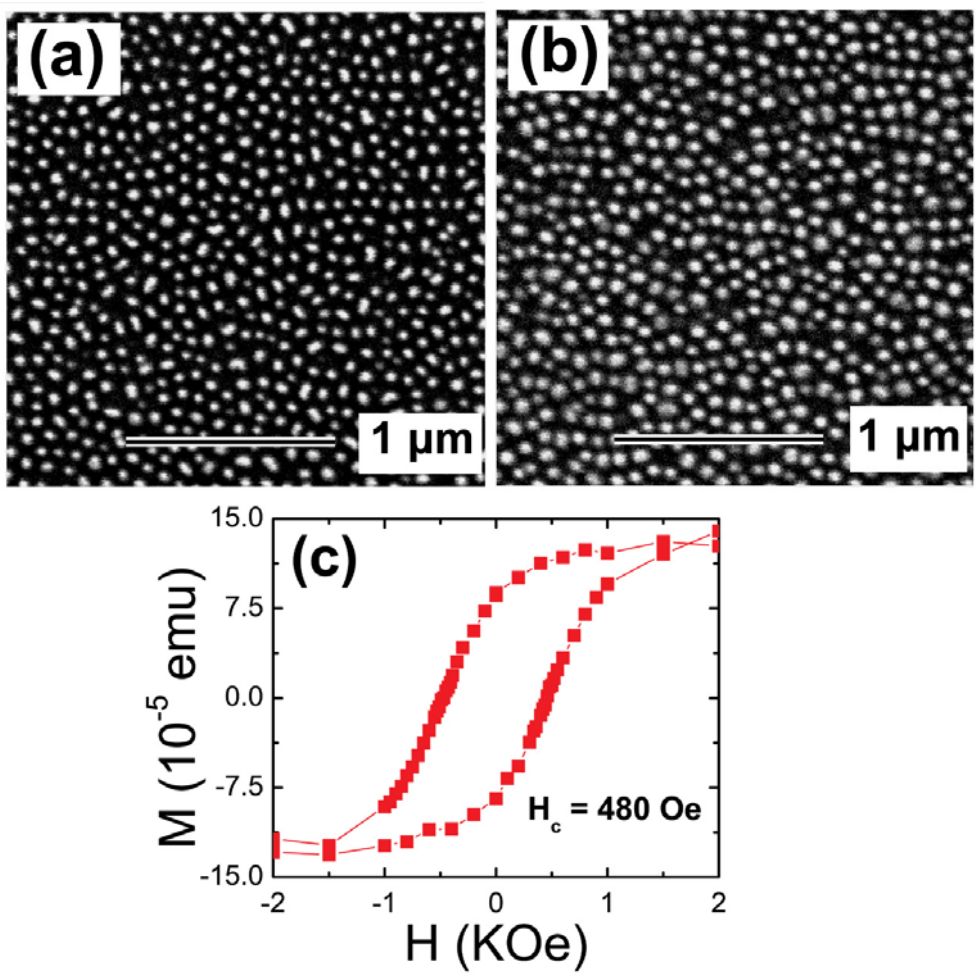

Figure II.16: SEM images of 20 nm-thick Fe film covered by titanium oxide pattern (a) before and (b) after 5 min argon-ion milling at an angle of 45°. (c) Magnetic hysteresis loop after pattern transfer into the Fe film using argon-ion milling.

succeeded in pattern transfer by using Ar^+ milling at an angle of 45°. With 5 min ion milling of a typical sample with a 20 nm-thick Fe film, the magnetic signal decreases from the original 1.65×10^{-3} emu to 2.5×10^{-4} emu, while the coercive field increases to 480 Oe, as shown in Fig. II.16 (c). Patterned FeF_2/Fe dots have also been fabricated by using a titanium oxide etching mask, which exhibit an exchange bias of $H_e = 46.2$ Oe after the sample is cooled to T=10 K in a magnetic field of 2 kOe. Fig. II.15 (a) and (b) shows the SEM images before and after Ar^+ milling. The dots in this typical sample are not regularly distributed, due to only a 500 nm-thick aluminum film being used for anodization. To improve pattern regularity, much thicker aluminum film must be used for the anodization.

When we transfer the pattern by using Ar^+ milling normal to the substrate, the dot feature disappears before the Ar^+ reaches the underlying Fe film, which is verified by the unchanged magnetic signal from SQUID measurements. The difference of the Ar^+ milling between these two different incident angles could be due to the angular dependence of the Ar^+ etching speed. The maximum etching speed does not happen along the normal direction, but rather at an angle of 45°. Thus, the etching speed along the direction normal to the sample is much higher if the beam incident direction is at an angle of 45°.

II.D Conclusions

Porous alumina masks are fabricated by anodization of aluminum films grown on semiconducting and insulating substrates. Control of the anodizing voltage and electrolyte allows fabrication of self-assembled porous alumina masks with diameters of 10-130 nm and periodicities of 20-250 nm. Masks with a periodicity of 20 nm exhibit pore densities exceeding 10^{12} per square inch, which might have relevance towards magnetic media with a corresponding density of 1 Tbit/in^2. With these alumina masks, ordered FM nanodot arrays with coverage exceeding 1 cm^2 are fabricated by electron beam evaporation and subsequent mask lift-off. For FM/FeF_2 bilayer samples, argon-ion milling at an angle of 45° is used instead of the mask lift-off. The average dot size and periodicity can be tuned in the 25-130 nm and 45-250 nm ranges, respectively. Dot periodicity

obtained from small angle neutron scattering on nanodot arrays covering $\sim$2.5 cm^2 is in a good agreement with the SEM characterizations.

II.E Acknowledgement

Support by The Air Force Office of Scientific Research is gratefully acknowledged.

III

Nanomagnetism

III.A Introduction

Nanomagnetism has been widely investigated in recent years due to its novel properties, which are distinguishable from those of bulk materials, and its potential applications towards magnetic memory and magnetic sensors. It is well known that a single domain state will take the place of a multi-domain structure, which exists in bulk magnets, with the magnetic pattern size comparable to or smaller than the magnetic domain wall width. For a circular magnetic nanopattern with a slightly larger pattern size, the magnetic spins may curl up along the circular edge to reduce the magneto-static energy, which results in a circular spin configuration (vortex state). [21, 22] There has been much investigation of the transition from a single domain to a vortex state through both theoretical calculations and experimental measurements, with consideration given to interesting intrinsic physics and possible applications of the vortex state towards magnetic memory systems. However, most of the previous studies focused mainly upon the scale well above 100 nm due to fabrication limits and equipment resolution. In this work, we investigate the magnetic properties of sub-100 nm dot arrays as fabricated by anodic porous alumina masks. [101]

III.B Sample preparation

Magnetic nanodots (except the samples mentioned in Section III.E) are fabricated with 20-nm of FM material deposited through the porous mask, at a rate of 1 $\AA$/s and a substrate temperature of 200 °C, which has been described in detail in Chapter II. [11] By tuning the anodization parameters and subsequently adjusting the pore size, we have obtained FM dots ranging in diameter from 20-130 nm. The resulting hexagonally ordered ferromagnetic dots are polycrystalline as determined by powder X-ray diffraction analysis. To manipulate the spin configurations (shown in Section III.E), we have also grown 20 nm thick Fe nanodots at 25 °C with a 3 h post-annealing at 500 °C (sample A) and without post-annealing (sample B), and grown at 400 °C without post-annealing (sample C). These three samples are grown using the same anodic porous alumina mask (anodized at 48 V), in order to avoid a dot diameter effect. In addition, Fe nanodots with a thickness ranging from 20 nm to 100 nm have also been fabricated, using a 48 V anodized alumina mask at a substrate temperature of 200 °C, in order to investigate the role of thickness in spin configurations (shown in Section III.E).

III.C Size dependence of magnetic properties

The magnetic properties of these Fe dots are measured by Quantum Design MPMS SQUID magnetometry. The resultant magnetic hysteresis loops for dots with a thickness of 20 nm (measured at 10 K) are shown in Fig. III.1 (a), which shows coercivities from 300 Oe to 800 Oe for various diameters. For comparison, the magnetic hysteresis loop of a 20 nm-thick Fe continuous film is given in Fig. III.1 (b). The coercivity of this film is about 38 Oe, which is one order of magnitude less than that of the sub-100 nm patterned dots. An overall enhancement of coercivity corresponding to a decrease in the dot diameter is also observed in Fig. III.1 (a), with a non-monotonic dependence that is probably due to sample to sample variations. Similar values for the coercive fields are observed in both Fe and Py dots of the same size, while there is a difference of two orders of magnitude in the magnetocrystalline anisotropy between Fe and Py. Hence, we attribute this enhanced coercivity mainly to finite size effects (shape anisotropy). In the patterned dots, magnetic spins reverse by coherent rotation, with the coercivity given as

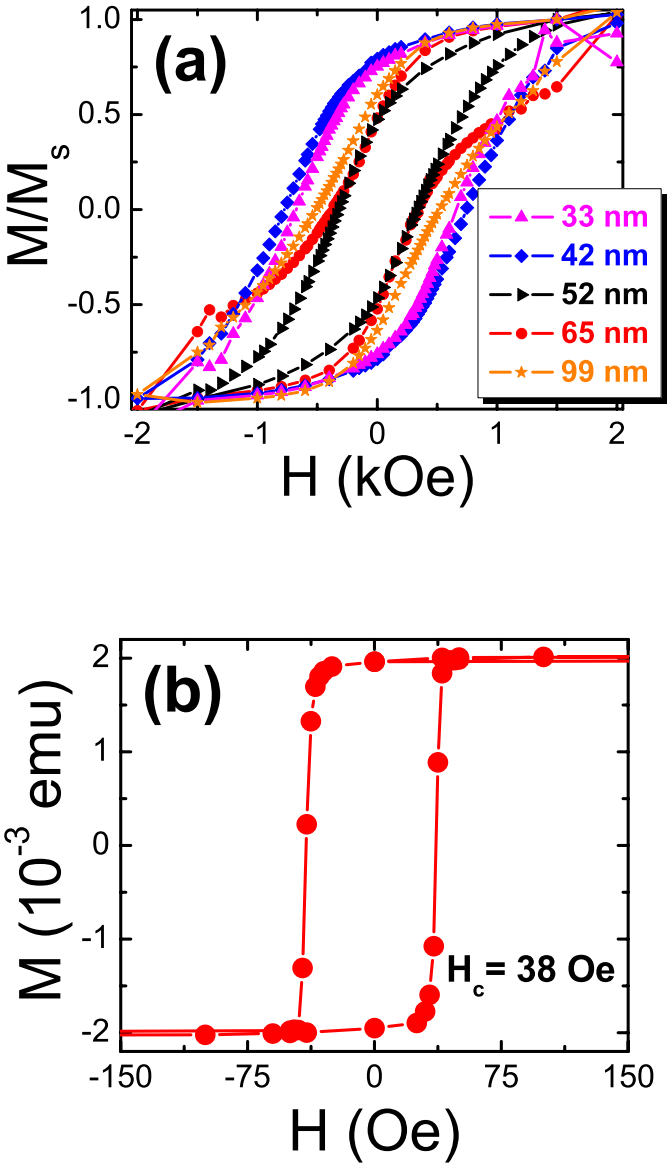

Figure III.1: (a) Magnetic hysteresis loops for 20 nm-thick Fe dot arrays with dot average diameters of 33-99 nm as measured by superconducting quantum interference device (SQUID) magnetometry at T=10 K, which shows the coercivities from 300 Oe to 800 Oe for various dot diameters. (b) Hysteresis loop of a 20 nm-thick Fe continuous film, which exhibits much smaller coercivity (38 Oe) than the dot samples.

$H_c = (2K_1/\mu_0 M_s) + \frac{1}{2}(1-3N)M_s$, where K_1 is the magnetic crystalline anisotropy, M_s is the saturation magnetization, and N is the demagnetizing factor of the nanodots. The coercivity of continuous films, with the formation of magnetic multidomain structures, has been theoretically calculated by Zhao, *et al.*, who reported the coercivity in the range of 0.14-0.42 H_K, where $H_K = 2K_1/\mu_0 M_s$ as given by the Stoner-Wohlfarth model (SW). [102]

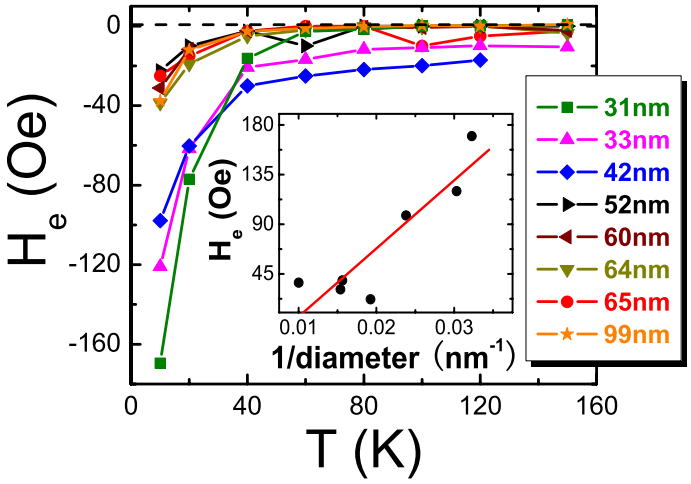

Figure III.2: Size and temperature dependence of exchange bias in side oxidized 20 nm-thick Fe dot arrays. The inset shows the magnitude of the exchange bias (T=10 K) as a function of the reciprocal of dot diameter, which confirms that the origin of the exchange bias arises from the side oxidation. A black dashed line is the eye guide of H_{ex}=0 Oe.

An Fe dot array is also measured after the sample is cooled down to 10 K in magnetic field of 2 kOe. Although there is no adjacent antiferromagnetic layer deposited with the Fe dots, exchange bias is observed. The exchange bias in our samples is attributed to the oxidation occurring along the sides of the dot, despite a protective layer on top of dots. The effect of native oxide on exchange bias is usually neglected for micro-sized patterned structures. This is due to their small surface to volume ratio, given as $S/V = 4\pi Dt/\pi D^2 t = 4/D$, where S is the area of the dot side surface, V is the dot volume, D is the dot diameter and t is the dot thickness. However, for smaller dot diameters, increased S/V results in an enhancement of the exchange bias, which has been confirmed by a linear fit of the exchange bias value as a function of the dot

diameter as shown in the inset of Fig. III.2. The exchange bias of oxidized Fe dots is inversely proportional to the dot diameter, thus confirming dot side oxidation to be the origin of the exchange bias. To get a better understanding of the exchange bias effect, we have measured the magnetic dots both after zero field cooling and after magnetic field cooling at 2 kOe. The enhanced magnetic remanence is observed after the sample is field cooled, which confirms that exchange bias is a good candidate for improving the stability of magnetic recording. [43–45]

III.D Transition from a single domain state to a vortex state

III.D.1 Transition quantified by loop shapes

As shown in Fig. III.1 (a), we find a striking differences in the shapes of the hysteresis loops. For dots with an average diameter larger than 62 nm, a reduced coercivity accompanied by a narrowing of the hysteresis loop close to the zero-magnetization state (pinched neck) are observed, while the hysteresis loops without pinched necks, resembling closely those of a random distribution of magnetic elements in single domain states, are observed for dots with smaller diameters. Typical hysteresis loops for Fe dots with average diameters of 42 nm, 64 nm, respectively, are shown in Fig. III.3 (a). In order to study the influence of dot diameter on the shape of the hysteresis loops, we introduce the parameters $W_{M=0}/W_{M=0.5M_s}$ where $W_{M=0}$, $W_{M=0.5M_s}$ are the widths of the hysteresis loop at zero magnetization, and half the saturation magnetization, respectively, as shown in Fig. III.3 (b). When the dot average diameter is less than 62 nm, a width ratio close to 1 is observed, corresponding to a single-domain spin configuration, as expected. For dot average diameters larger than 62 nm, this ratio is highly reduced due to the appearance of the pinched neck near zero magnetization. The different magnetic properties of the dots are also evident in the virgin curves. The virgin curves are measured by slowly increasing the magnetic field from 0 Oe after the dots have been demagnetized (zero magnetic remanence). The virgin curves reversibility is studied by gradually decreasing the field back to zero after the virgin measurements reach various reversal fields (H_r). Fig. III.4 (a)-(b) shows the virgin curves (blue triangles) and major

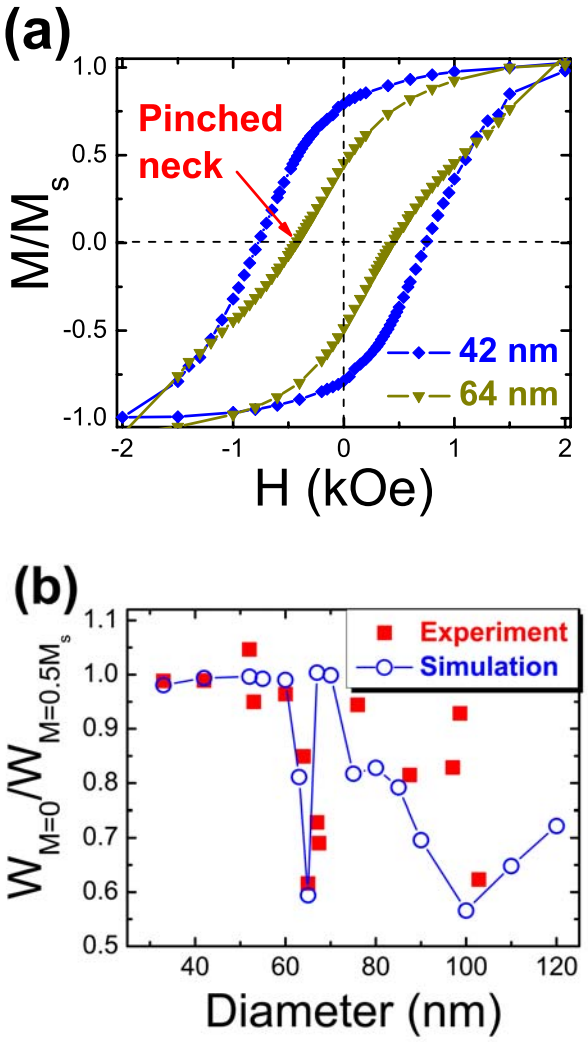

Figure III.3: (a) Typical magnetic hysteresis loops for 20 nm-thick Fe dot arrays with average diameters of 42 nm, 64 nm. (b) The loop width ratio of $W_{M=0}/W_{M=0.5M_s}$ as a function of the dot diameter obtained from magnetic hysteresis loops (red solid squares) and Monte Carlo simulations (blue open circles), where $W_{M=0}$, and $W_{M=0.5M_s}$ are the widths of the hysteresis loop at zero magnetization, and half of saturation magnetization, respectively. (After Ref. [101]).

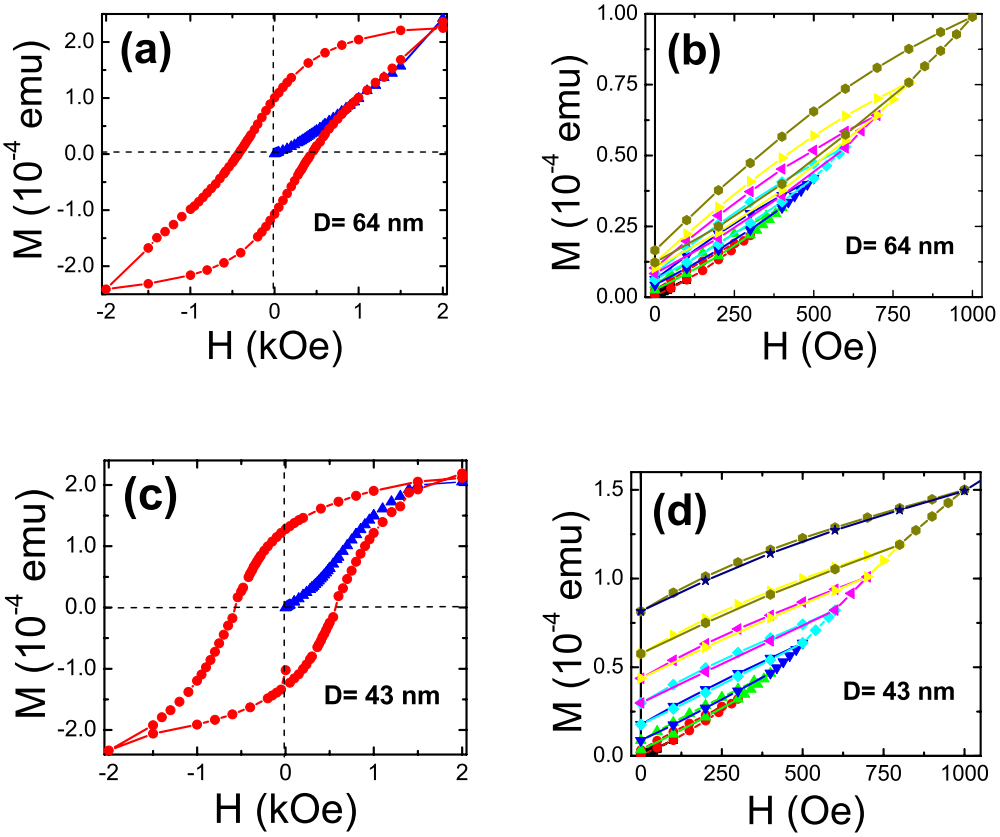

Figure III.4: Typical magnetic hysteresis loops (red circles) and virgin curves (blue triangles) for the 20 nm-thick Fe dots with average diameters of (a) 64 nm and (c) 43 nm. An overlap of the virgin curve upon the lower branch of the major loop is observed for dots with an average diameter of 64 nm, while the virgin curve is well separated from the major loop for dots with an average diameter of 43 nm. The reversibility of virgin curves for the dots with (b) an average diameter of 64 nm, which is not observed for the dots with (d) an average diameter of 43 nm.

loops (red circles) of dot arrays with average diameters of 43 nm and 64 nm, respectively. An overlap of the virgin curve upon the lower branch of the major loop is observed for dots with 64 nm in average diameter, while the virgin curve is well separated from the major loop for dots with an average diameter of 43 nm. In addition, the virgin curves for the dots with an average diameter of 64 nm clearly show reversibility [shown in Fig. III.4 (c) and (d)], which is not observed in the dots with 43 nm in average diameter.

III.D.2 Theoretical calculations

Due to the feature size of our dots (well below 100 nm), which reaches the resolution limit of current magnetic microscopy equipment, [23, 25] we cannot obtain a clear picture of the magnetic spin configurations in these Fe dots by direct measurements. With this in mind, additional theoretical (numerical or analytical) calculations play an integral role in our understanding of nanomagnetism. Therefore, we have studied the magnetic properties of Fe dots by using both Monte Carlo simulations and micromagnetic simulations. A more detailed discussion regarding the micromagnetic simulations will be given in Chapter IV. Monte Carlo simulations are carried out in collaboration with Mejía-López *et al.* [31] using the Metropolis algorithm that includes local dynamics and single-spin flip methods, as shown in Chapter I. [31, 35–37]

According to the simulations, the hysteresis loops with widths ratio close to 1 accompanying dot diameters smaller than 60 nm correspond to a single-domain (SD) spin configuration. Magnetic reversal takes place through coherent spin rotation, resulting in a square hysteresis loop. The loop shearing could be due to dot interactions as well as averaging effects caused by distributions in the dot size and anisotropy. The pinched neck close to the zero-magnetization state for the dots with an average diameter larger than 62 nm is attributed to the appearance of a vortex state (VS), similarly to the previous study using micromagnetic simulations and MOKE. [103] With a decrease in magnetic field from positive saturation state, the spin configuration switches from a single domain to the vortex state at the nucleation field. A further decrease in the magnetic field leads to motion of the vortex core along the direction perpendicular to the external field, followed finally by a return to the single domain state (with the spins' direction opposite to that of the original single domain state), and the vortex core moving out of the dot

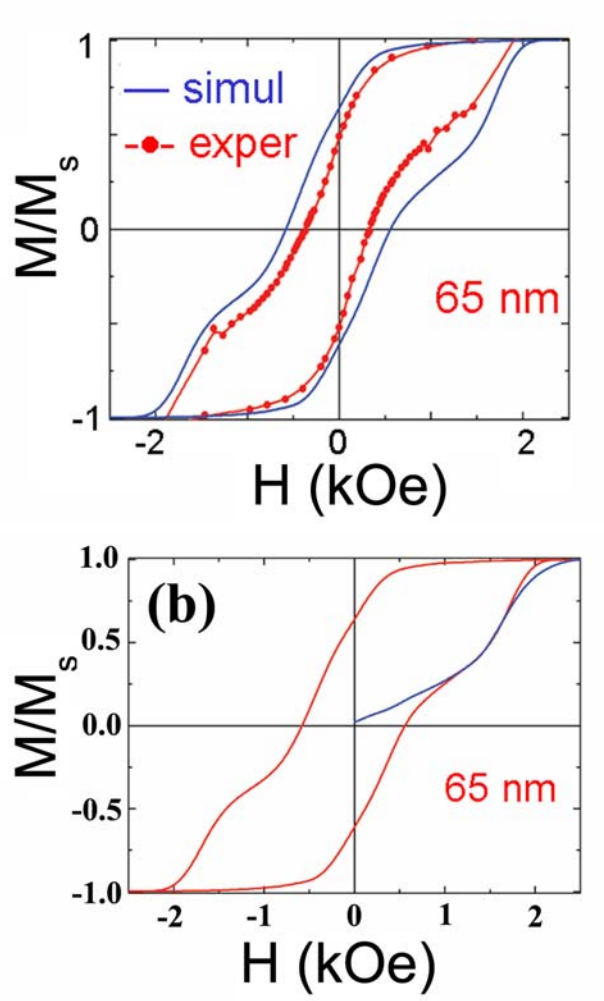

Figure III.5: (a) Experimental hysteresis curve (dots) for an array of 20 nm-thick dots with an average diameter of 65 nm, and the calculated hysteresis curve (continuous line) for a noninteracting dot with the same size (solid line). (b) Calculated hysteresis loop (red line) and virgin curve (blue line) for a dot with the same size. (After Ref. [31]).

boundary at the annihilation field. The vortex state with reduced magnetization results in a decrease of the hysteresis loop width near zero magnetization. The loop width ratio as a function of the dot diameter is investigated by both Monte Carlo and micromagnetic simulations, with the detailed discussion shown in Chapter IV.

For the virgin curve, the applied magnetic field shifts the vortex core outwards from the dot center. As long as the core is not shifted beyond the physical boundary of the dot by a field less than the annihilation field, the vortex core will return to its initial position in the center once the field is removed, which makes the virgin curve fully reversible in the absence of defects and pinning. The presence of the vortex state in the dots with a diameter larger than 62 nm is confirmed by Monte-Carlo simulations, [31] which reproduce well the shape and reversibility of the virgin curves as described above, as shown in Fig. III.5.

III.D.3 Magnetic reversibility measurements

The magnetic reversibility is also investigated by the first-order reversal curve (FORC) method in collaboration with Dumas *et al.* [104] After positive saturation, the magnetization M is measured starting from a reversal field H_r back to positive saturation, tracing out a FORC. A family of FORCs are measured at different H_r, with equal field spacing, thus filling the interior of the major hysteresis loop. The FORC distribution is defined as a mixed second order derivative:

$$\rho(H_r, H) \equiv -\frac{1}{2}\frac{\partial^2 M(H_r, H)}{\partial H_r \partial H} \tag{III.1}$$

which eliminates the purely reversible components of the magnetization. Thus, any non-zero ρ corresponds to irreversible switching processes. The FORC distribution is plotted against either (H_r, H) coordinates or (H_c, H_b) coordinates. [105–109]. This transformation is accomplished by a simple rotation of the coordinate system defined by: $H_b = (H + H_r)/2$ and $H_c = (H - H_r)/2$.

The major hysteresis loops, delineated by the outer boundaries of the FORCs, of typical Fe dots with the diameter of 52±8 nm, 58±8 nm, and 67±13 nm are given in Fig. III.6 (a)-(c), respectively. As mentioned in Section III.D, the major loop for 52 nm dots corresponds to a single domain state, while the pinched neck loop for the 67 nm

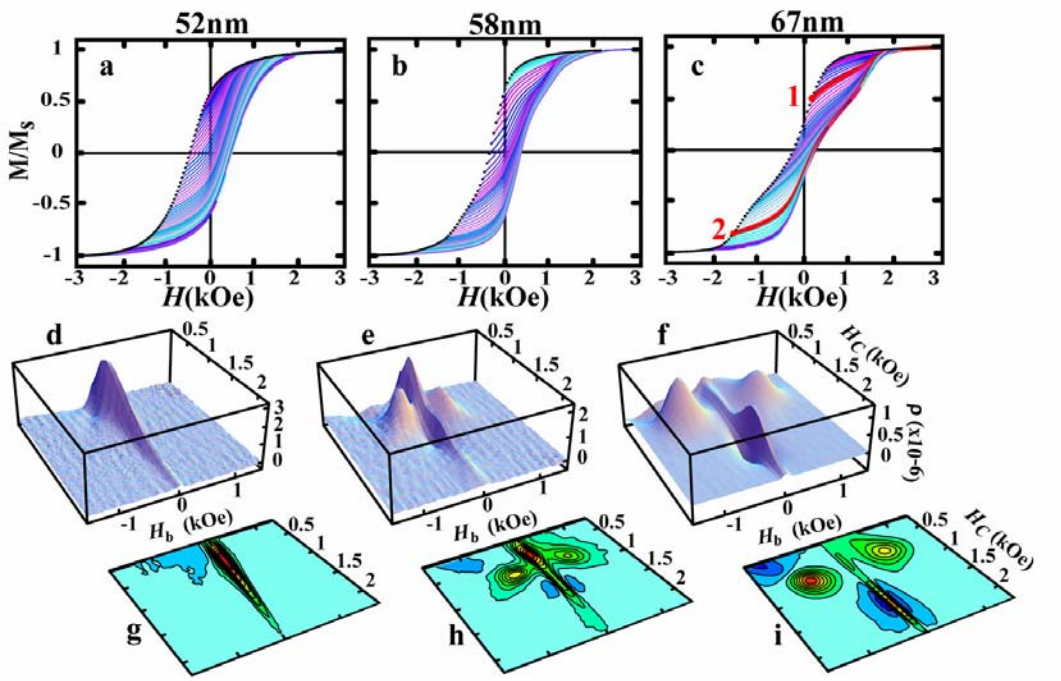

Figure III.6: First-order reversal curves and the corresponding distributions. Families of FORCs (a-c), whose starting points are represented by black dots for the 52 nm, 58 nm, and 67 nm Fe nanodots, respectively. In (c), two FORCs, marked in red, correspond to line scans 1 and 2 in (b). The corresponding FORC distributions are shown as 3-dimensional plots (d-f) and contour plots (g-i). (After Ref. [104]).

dots is indicative of a vortex state. Subtle differences seen in the major hysteresis loops manifest themselves as striking differences in the corresponding FORC distributions, as evidenced in Fig. III.6 (d)-(i). For the 52 nm nanodots, the only predominant feature is a narrow ridge along the local coercivity H_c-axis with zero bias [Fig. III.6 (d) and (g)]. The ridge is peaked at $H_c = 525$ Oe, near the major loop coercivity value of 475 Oe. This pattern is characteristic of a collection of non-interacting single domain particles. As the nanodot diameter is increased, the FORC distribution becomes much more complex. The 67 nm sample is characterized by three main features, as shown in Fig. III.6 (f) and (i): two pronounced peaks at $H_c = 650$ Oe and $H_b = \pm 750$ Oe, and a ridge along $H_b = 0$, forming a butterfly-like contour plot [Fig. III.6 (i)].

In addition to qualitative differences between samples in the single domain and vortex state, the FORC distribution also allows us to extract quantitative information regarding the reversal processes. For the 52 nm sample, we have extracted this distribution by projecting the ridge in Fig. 7(b) onto the H_c-axis ($H_b = 0$ Oe), as shown in Fig. III.7 (a). The relative height gives the appropriate percentage of nanodots with a given coercivity. This extracted coercivity distribution can be compared with the theoretical size dependence of coercivity for a single domain particle $H_c \approx (C_1/D^2) - C_2$, where D is the dot diameter, C_1 and C_2 are constants. [110] The constants of C_1 and C_2 are calculated based upon the FORC projection peaks of the 52 nm and 58 nm samples (H_c=5350 Oe for D=52 nm, and H_c=3750 Oe for D=58 nm). The obtained C_1 and C_2 are then used to calculate a coercivity distribution [solid black circles in Fig. III.7 (a)] based upon the size distribution obtained from the SEM images. Excellent agreement is obtained as compared to that determined from the FORC distribution, after a rescaling of the latter by an arbitrary weight.

To analyze magnetic reversals in the 67 nm dots, the FORC distribution ρ is replotted in against (H_r, H) coordinates. The complex butterfly-like pattern of Fig. III.6 (i) now transforms into irreversible switching mainly along line scans 1 and 2 in Fig. III.7 (b), which correspond to FORCs starting at H_r= 100 Oe and -1450 Oe, respectively [marked in red in Fig. III.6 (c)]. Along line scan 1 ($H_R = 100$ Oe), when the applied field $H = 100$ Oe, vortices have already nucleated in most of the nanodots. With increasing field H, ρ becomes non-zero and peaks appear at 1320 Oe, corresponding

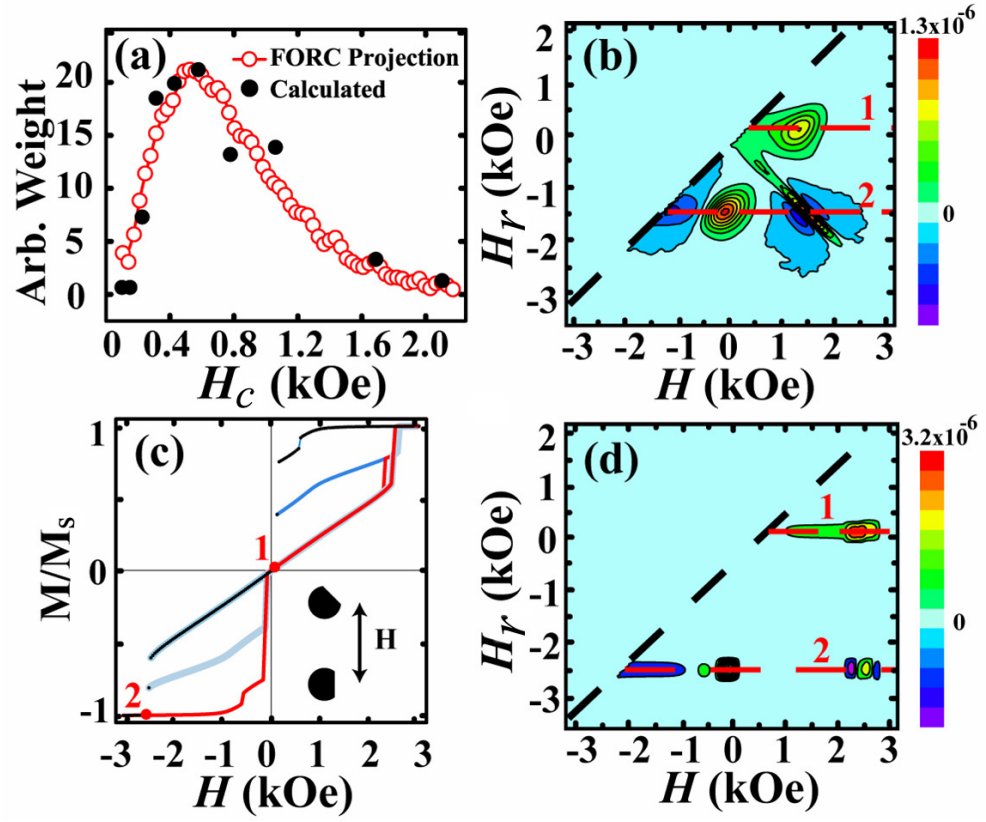

Figure III.7: (a) Coercivity distribution for the 52 nm nanodots obtained from the projection of FORC distribution onto the H_c-axis (red circles), and a calculation based on measured size distribution (black squares). (b) The experimental FORC distribution for the 67 nm nanodots plotted against applied field H and reversal field H_r. Dashed horizontal line scans 1 and 2 highlight the two important reversal paths discussed in the text. (c) A family of simulated FORC's generated using the OOMMF code. Inset shows the orientations of the two dots simulated. (d) The FORC distribution calculated from the simulated FORC's shown in (c). (After Ref. [104]).

to vortex annihilation in the majority of the nanodots (H_{n1}). Line scan 2 starts at $H_r = -1450$ Oe, where the majority of the nanodots have been negatively saturated. As H is increased, a maximum in ρ is first seen at $H = -100$ Oe, corresponding to nucleation of the vortices within the nanodots. A second maximum is found at $H = 1450$ Oe, corresponding to vortex annihilation (H_{n2}). We also notice that the peaks in Fig. III.7 (b) are rather broad, which is a manifestation of the vortex nucleation and annihilation field distributions.

One possible origin of these double annihilation field magnetic reversals could be due to asymmetric shapes of our nanodots. This has been verified by micromagnetic simulations carried out on a nanodot with a small cut on one side (as described in Chapter IV), which reflects the fact that our fabricated dots are not perfectly circular. The simulated FORC contours with field parallel and 45° to the cut-edge are shown in Fig. III.7 (c). Peaks in the simulated FORC distribution clearly indicate nucleation and annihilation fields of the vortex which are apparent in Fig. III.7 (c). It is clear that the simulated FORC reproduces the key features of the experimentally obtained ones in Fig. III.7 (b). Along line scan 1, the vortices are annihilated from the same side of the nanodot as which they first nucleated; along line scan 2, the vortices nucleate on one side of the dot and are annihilated on the other [Fig. III.6 (c)]. It is noteworthy that the annihilation field along line scan 2, $H_{n2} = 1450$ Oe, is larger than that along line scan 1, $H_{n1} = 1320$ Oe. Thus it seems more difficult to drive a vortex across the nanodot and then annihilate it than to nucleate and annihilate the dot from the same side. Hence the asymmetric dot shape is essential in obtaining a larger annihilation field along scan 2 than along scan 1, leading to the negative-positive-negative FORC feature at the lower right corner. Because only two different angles are taken into account, the features in the FORC distribution are much sharper than the experimental data in which a distribution of angles should be present.

III.D.4 Vortex core size measurements by polarized neutron scattering

Since the first imaging of magnetic vortices in permalloy (Py) sub-micron disks using magnetic force microscopy (MFM), [21] many efforts have focused on the 3-dimensional spin structure and magnetic reversal via the vortex state, [23, 24] vortex

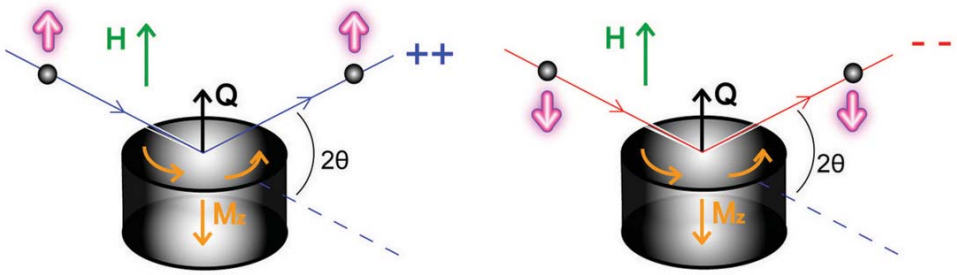

Figure III.8: Schematic of the polarized neutron scattering measurement setup. The neutrons are polarized along the out-of-plane direction.

dynamics [25, 111] and switching of the vortex core polarity, [112] and vortex chirality, [113] in dots, rings, and other micro- and nano-patterned structures. Those studies were performed by magneto-optical Kerr effect (MOKE) magnetometry, magnetic-resonance measurements, magnetization-sensitive microscopies, such as MFM, scanning electron or ion microscopy with polarization analysis, spin-polarized scanning tunneling microscopy, X-ray magnetic circular dichroism, and Lorenz microscopy. [21, 23–25] Most of the experiments were performed with planar structures in which the in-plane size was much larger than 100 nm. Imaging the vortex and especially the vortex core in sub-100 nm structures is limited by the resolution of the tools. Moreover, the majority of such imaging is only qualitative and does not allow quantification of the magnetization and size of the vortex core. Here, we perform grazing incidence small angle neutron scattering with polarization analysis (polarized GI-SANS) in collaboration with Fitzsimmons *et al.* to measure the core size and magnetization, as shown in Fig. III.8.

The neutron scattering (non-spin-flip), with the neutron beam polarized perpendicular to the sample surface, (please refer to Reference [101] for the details) gives the net out-of-plane magnetization averaged over the volume of the dot, m_z=100±40 emu/cm^3. This magnetization is equivalent to that of a 20-nm-thick Fe cylinder with a diameter of 16±3 nm (= 65 nm$\times\sqrt{m_z/M_s}$, where M_s = 1714 emu/cm^3), representing a vortex core. The magnetization profile for a single 20 nm-thick Fe dot with a diameter of 65 nm has been calculated using micromagnetic simulation, which gives the corresponding out-of-plane magnetization and vortex core diameter of 78 emu/cm^3 and ∼14 nm, respectively, in good agreement with the experimental result obtained from polarized

GI-SANS. Similar values are also obtained using Monte Carlo simulations.

III.E Manipulation of spin configurations

So far, we have characterized the spin configurations, especially the vortex state, by using SQUID magnetometry, FORC measurements, and polarized neutron scattering. In the following, I will show you several factors which can be used to manipulate the spin configurations, including magnetic anisotropy and dot thickness.

In this work, the magnetic hysteresis loops of Fe dots grown at 25 °C with 3 h post-annealing at 500 °C (sample A, magenta stars) and without post-annealing (sample B, red squares), and grown at 400 °C without post-annealing (sample C, blue triangles) are measured at 300 K with an in-plane magnetic field, as shown in Fig. III.9 (a). Sample B exhibits the best vortex state, as evidenced by the smallest loop width ratio. With an increase in growth temperature or post-annealing, a striking suppression of the vortex state is observed by the increased loop width ratio, together with enhanced remanence and coercivity. The co-evaporated continuous Fe films also exhibit larger coercivity when grown at higher temperatures or post-annealed, which is a good indication of increased magnetic anisotropies. To further clarify the effects of growth temperature and postannealing procedures, structural properties of the dots are measured by AFM. Fig. III.9 (b) and (c) show the typical AFM images for both samples B and C. The Fe dots of sample C grown at 400 °C exhibit much larger grain sizes and rougher boundaries. Considering the random orientation of the anisotropic easy axis, a less number of grains in a single dot (with larger grain size) will statistically increase the average anisotropy, resulting in a suppression of the vortex state. In addition, rougher boundaries can also reduce the stability of the vortex state, as confirmed by the micromagnetic simulations.

The phase diagrams given by Buda et al. [30] have shown that the spin configuration is a function of both dot diameter and dot thickness. When the dot aspect ratio (dot thickness over diameter) is less than a critical value of 0.90, in-plane spin configurations are preferred, whereas an increase in the dot thickness results in preference towards vortex state. However, Ha and Porrati have predicted the existence of a vortex state with in-plane spins in the vortex core (named in-plane vortex state) when the dot

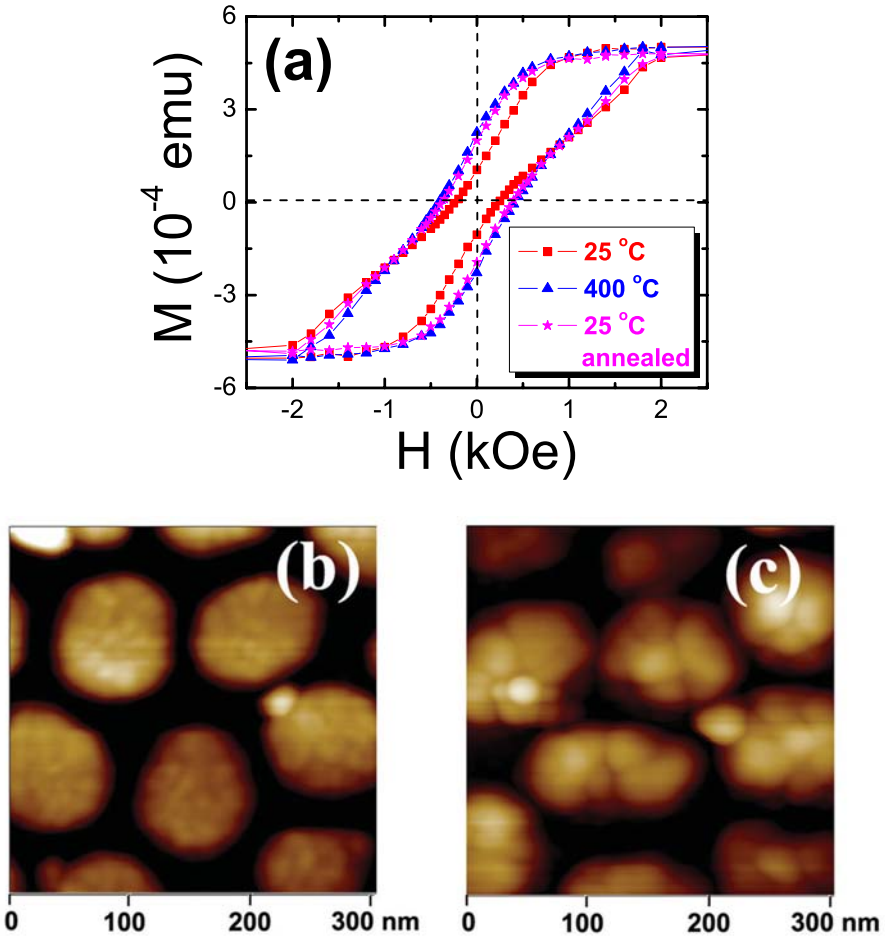

Figure III.9: (a) Magnetic hysteresis loops of Fe dots grown at 25°C with 3 h post-annealing at 500°C (sample A, magenta stars) and without post-annealing (sample B, red squares), and grown at 400°C without post-annealing (sample C, blue triangles), which are measured at 300 K with an in-plane magnetic field. Accompanying either an increase of growth temperature or post-annealing is a striking deterioration of the vortex state is observed. Typical AFM images of (b) sample B and (c) sample C, which shows much larger grains and rougher boundaries in sample C.

thickness is comparable to the dot diameter. [114–116] To date, this in-plane vortex state has not been confirmed by experimental measurements. Therefore, we have decided to investigate the thickness dependence of spin configurations and verify the existence of the in-plane vortex state. The magnetic properties of Fe dots with 76 nm in average diameter and 20-100 nm in thickness are measured by SQUID magnetometry at 300 K with the magnetic field applied along the in-plane direction.

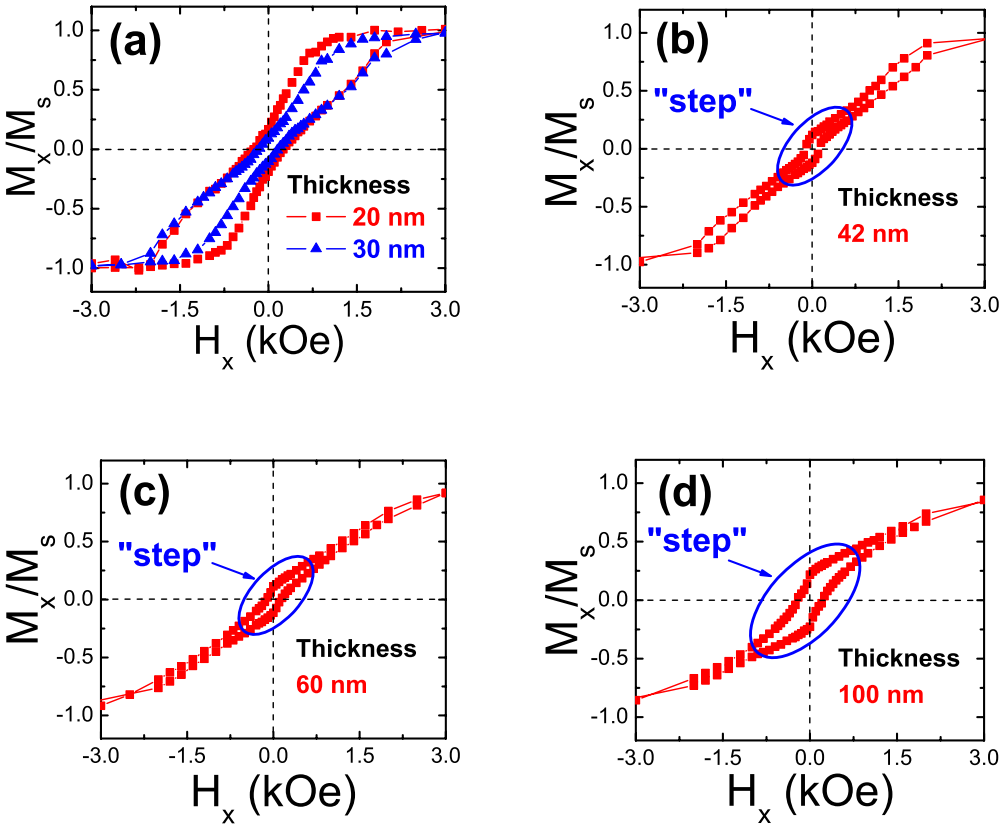

Figure III.10: (a) Magnetic hysteresis loops for Fe dots with an average diameter of 76 nm and a thickness of 20-30 nm, which exhibit enhancement of the vortex state as the dot diameter increases. (b) Magnetic hysteresis loop for Fe dots with an average diameter of 76 nm and a thickness of 42 nm, which shows parallel branches indicative of the emergence of the in-plane vortex state (with vortex core pointing along an in-plane direction), and a "step"-like feature around zero field. This "step"-like feature is enhanced by an increase in the dot thickness, as shown in (c)-(d).

Fig. III.10 (a) shows the magnetic hysteresis loops of dots with thicknesses of 20 nm (black squares) and 30 nm (red triangles), respectively. The increase in dot

thickness from 20 nm to 30 nm results in a preference of the vortex state, as indicated by a decrease in the coercivity, magnetic remanence, and loop width ratio. This vortex state preference is due to reduction of the shape anisotropy, which has been investigated by experimental measurements and theoretical calculations. However, when the dot thickness is further increased to 42 nm, the hysteresis loops exhibit two striking features: a small "step" around zero field and narrow hysteresis loop in the rest part, as shown in Fig. III.10 (b). A narrow hysteresis loop is usually caused when an external field is applied along the hard axis. However, this is ruled out in our case because the aspect ratio for the nanodots is well below the transition point from in-plane easy axis to out-of-plane axis. Micromagnetic simulations show that the parallel branches' feature is due to the emergence of the in-plane vortex state, which will be discussed in Chapter IV.

So far, we have confirmed the existence of the in-plane vortex state based upon both magnetic measurements and micromagnetic simulations. For the "step"-like feature, Ha *et al.* observed a similar result from numerical calculations and attributed it to a switch in the core polarity (in-plane vortex state). [114] However, this feature has not been reproduced by our micromagnetic simulations that model the in-plane vortex state, due to unknown reasons. Another possible origin of this "step"-like feature is the emergence of an out-of-plane single domain state in the dots with smaller diameter, due to the dot size distribution. Also, the enhancement of the "step" as dot thickness increases indicates that the out-of-plane single domain state is formed in a larger portion of the dots, as shown in Fig. III.10 (c) and (d).

III.F Conclusions

In this chapter, we investigate the size dependence of magnetic nanodots fabricated using self-ordered porous alumina shadow masks. For the 20-nm thick Fe dots, direct evidence of both the appearance of the magnetic vortex whose diameter is smaller than 100 nm, and a transition from a single domain to a vortex state as a function of the dot diameter and applied magnetic field have been observed. This single domain to vortex state transition has also been studied by FORC technique, which quantifies the magnetic phase fractions and the distributions of vortex nucleation and annihilation

fields. The vortex core size of 16±3 nm for the Fe dots with a diameter of 65 nm is obtained from polarized GI-SANS measurements, which is in good agreement with results of the Monte Carlo and micromagnetic simulations. Finally, we can also manipulate the spin configurations through tuning of the magnetic anisotropy and dot thickness.

III.G Acknowledgement

Support by The Air Force Office of Scientific Research is gratefully acknowledged.

IV

Micromagnetic simulations

IV.A Introduction

In Chapter III, we discuss how the transition from a single domain to a vortex state is affected by an increase in the dot diameter by measuring the dot array using SQUID magnetometry and the FORC method. However, a clear picture of the magnetic spin configurations for a single FM dot is still missing due to the feature size of our dots (well below 100 nm), which reaches the resolution limit of current magnetic microscopy equipments. With this in mind, additional numerical calculations (simulations) are crucial for a clear understanding of the nanomagnetism. In this work we perform micromagnetic simulations by using NIH OOMMF code, [34] which is based on the Landau-Lifshitz equation:

$$\frac{dM}{dt} = -|\bar{\gamma}|\, M \times H_{eff} - \frac{|\bar{\gamma}|\,\alpha}{M_s} M \times (M \times H_{eff}) \qquad \text{(IV.1)}$$

where M is magnetization, H_{eff} is the effective field, $|\bar{\gamma}|$ is the Landau-Lifshitz gyromagnetic ratio, and α is the damping coefficient. SI units are used in these micromagnetic simulations, and finally transformed into Gaussian units for consistency with experimental results. Bulk parameters of Fe, with $M_s = 1.7 \times 10^6$ A/m, $A = 2.1 \times 10^{-11}$ J/m, and cubic anisotropy $K_1 = 4.8 \times 10^4$ J/m^3, are used to simulate a single Fe nanodot as well as a dot array. Considering the exchange length of Fe $l_{ex} = \sqrt{2A/(\mu_0 M_s)^2}$=2.4 nm, a square cell with a size of 1 nm, which is much smaller than the exchange length, is used for the 2-dimensional micromagnetic calculations. Calculation is considered to be

at equilibrium when the torque $|M \times H_{eff}|$ is less than a given tolerance, $1 \times 10^6 M_s^2$.

IV.B Study of spin configurations: single domain and vortex state

The major hysteresis loops of a typical Fe single dot with a diameter of 30-100 nm are simulated with a uniform field, along the in-plane easy axis for cubic anisotropy, and a step of ±100 Oe after saturation with a field of ±10 kOe, as shown in Fig. IV.1 (a). When the diameter is 40 nm or smaller, the dot switches directly from positive (negative) to negative (positive) saturation, as represented by a square hysteresis loop. According to this simulation, a single domain state is the sole spin configuration. However, for a dot with a diameter of 60 nm or larger, the spin configuration first switches from the single domain to the vortex state at the nucleation field, and then switches to the single domain state with the opposite spin direction at the annihilation field. Thus, the simulations of hysteresis loops show that the single domain to vortex state (S-V) transition happens between a diameter of 40 nm and 60 nm. This value is slightly smaller than found experimentally, which indicated the S-V transition to occur at a dot diameter of 62 nm. The discrepancy is partially due to the fact that the bulk magnetic parameters, which are used in our calculations, are different from those at a length scale below 100 nm. In addition, some of neglected factors, such as neighboring dot interactions, dot roughness and anisotropies, can also affect the spin configurations.

The effect of dot interactions is studied by comparing the magnetic properties for dot arrays with different dot distances. Fig. IV.2 (a) shows a typical schematic image of an Fe dot (t = 20 nm, D = 60 nm) array, with black representing the magnetic materials. Hysteresis loops for the dot arrays, with a center-to-center distance of 70 nm, 90 nm, and 120 nm, have been simulated with magnetic fields applied both along the X-axis and Y-axis, as shown in Fig. IV.2 (b) and (c). The steps along the hysteresis loops correspond to unsynchronized magnetic switchings of the dots, which can be smoothed out with more dots simulated. Regardless of the difference in the field directions, increased nucleation fields and decreased annihilation fields as the magnetic field is decreased from positive saturation are observed in both Fig. IV.2 (b) and (c) with the

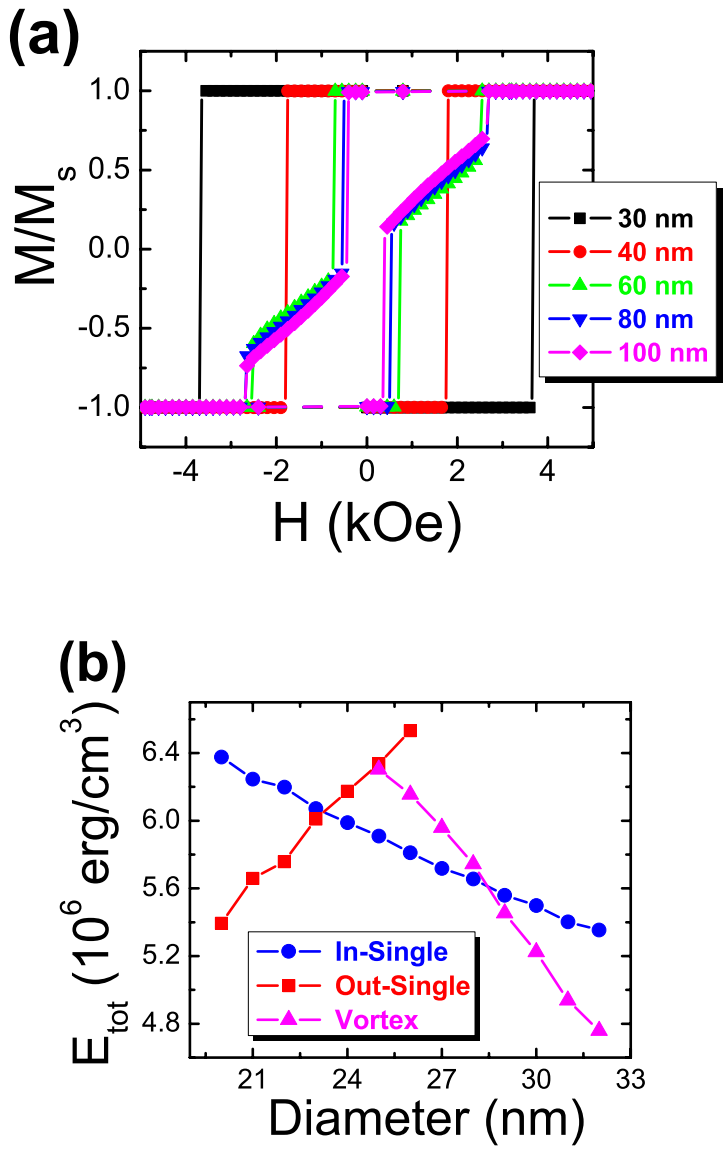

Figure IV.1: (a) Diameter dependence of the magnetic hysteresis loops as calculated by micromagnetic simulations which predict that a vortex state only exists for dots with a diameter above 40 nm. (b) Diameter dependence of the ground state energy for the Fe circular dot with spin configurations of the in-plane single domain state (blue circles), out-of-plane single domain state (red squares), and vortex state (purple triangles). It shows that the vortex state is the ground state for a diameter above 28 nm.

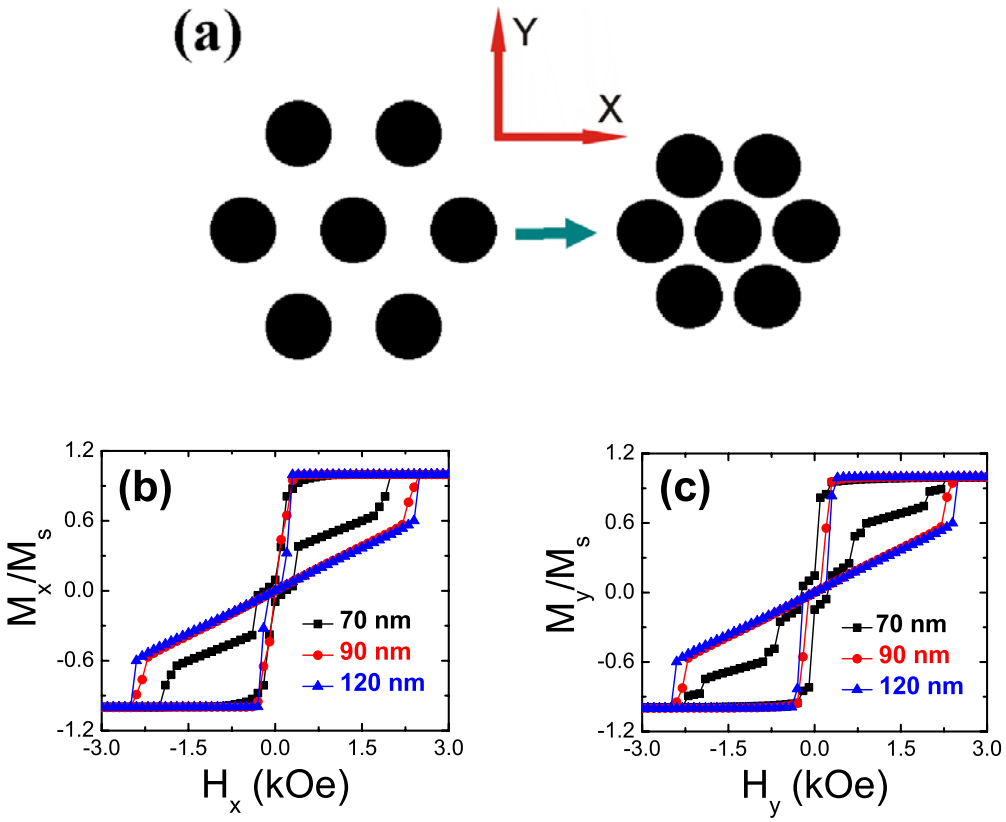

Figure IV.2: (a) Schematic of dot arrays with different distances. Hysteresis loops for the dot arrays with a center-to-center distance of 70 nm (black squares), 90 nm (red circles), and 120 nm (blue triangles) simulated with magnetic fields applied along the (b) X-axis and (c) Y-axis.

distance increased from 70 nm to 90 nm. This results in a lengthened field range for the existence of a vortex state, and correspondingly enhances its stability. As the distance is further increased from 90 nm to 120 nm (twice the dot diameter 2D), there is only a slight change in the hysteresis loops, meaning that interaction between the neighboring dots can be neglected when the dot distance is close to 2D. Similar results have been obtained by analytical calculations and Monte-Carlo simulations. [31] The dots fabricated from the anodic porous alumina exhibit a distance slightly smaller than 2D, resulting in a slight shift of the S-V transition towards a larger dot diameter. However, since the distance is close to 2D, this weak dot interaction is neglected in the following simulations.

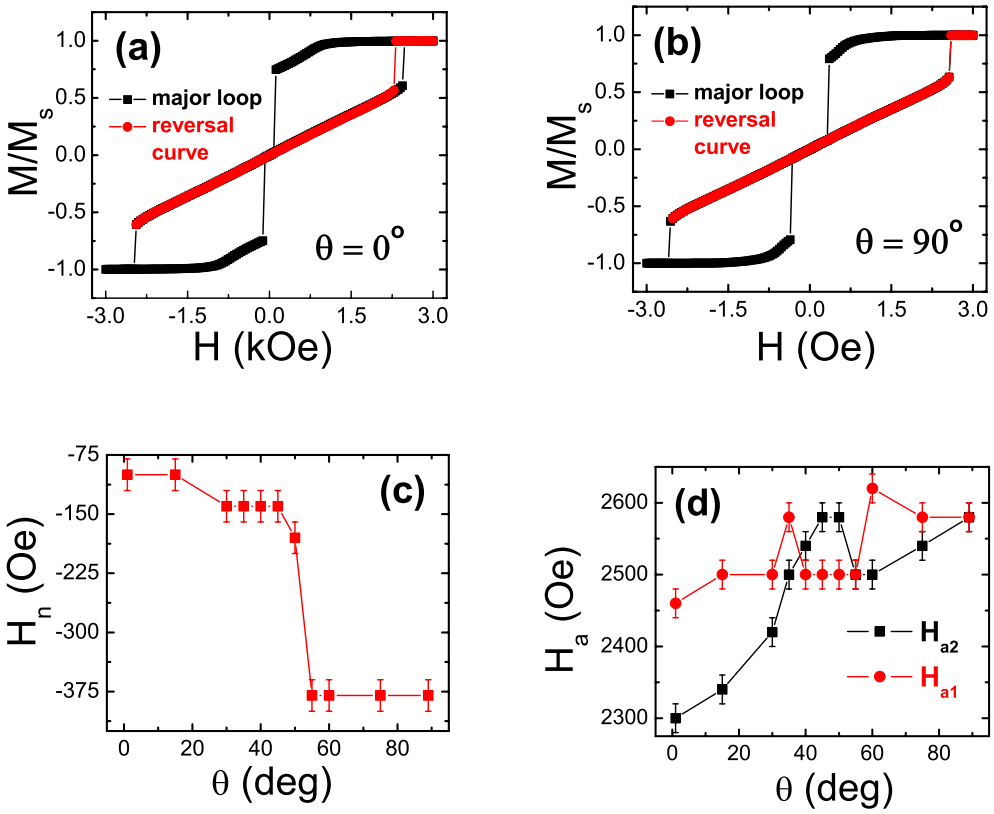

Figure IV.3: Simulated magnetic major loops and virgin curves for an cut-edge dot with the magnetic field applied (a) parallel and (b) perpendicular to the cut-edge. Vortex (c) nucleation field and (d) double annihilation fields plotted as a function of the angle between the applied magnetic field and cut-edge.

The anisotropy effect has been studied by Monte-Carlo simulations, [31] giv-

ing a universal trend: the higher the degree of degeneracy of states that minimize the anisotropy energy term, the more such anisotropy favors the vortex state. In this chapter, I will investigate the effect of an asymmetric shape anisotropy by artificially cutting the circular dot along a straight line, as shown in Fig. IV.3 (a).

In addition to the major hysteresis loops (starting from the saturated single domain state), we also simulated the reversal curves by starting from a reversal field H_r back to positive saturation. These reversal curves follow either the major hysteresis loop with $H_r > H_n$ or $H_r < H_a$, or the virgin curve with $H_a < H_r < H_n$, in which a magnetic dot is in its vortex state. When the magnetic field is parallel to the cut-edge, the annihilation field along the virgin curves (H_{n1}) is smaller than that along the major loop (H_{n2}), while $H_{n1} = H_{n2}$ is observed with the field direction perpendicular to the cut-edge. Snapshots of the spin configurations show that the discrepancy in annihilation fields is due to different directions of vortex core motion. When the applied magnetic field reaches the nucleation field, the positive (negative) single domain state is transformed into the vortex state with the vortex core moving towards the dot center from the cut-edge. The chirality of spins in the vortex state depends upon the relative direction between the vortex core motion and the initial saturation magnetization. For example, if motion of the vortex core is along the -Y direction and the initial saturation magnetization is along the +X direction, the chirality of the formed vortex state is counterclockwise.

The capability to manipulate the chirality of the vortex state by using a cut-edge structure has been demonstrated by means of Lorentz transmission electron microsocpy and magnetoresistance measurements. [117] Unlike the clear preference to nucleate from the cut-edge, the vortex state can be annihilated with the vortex core leaving the dot from either the round or cut-edge, depending upon both the change in magnetic field and the vortex chirality. For the vortex state with a counterclockwise chirality, a decrease in the magnetic field results in the vortex core leaving from the round side (along the major loop), while an increase in the magnetic field leads to annihilation occurring from the cut-side (along the virgin curve). The difference in the annihilation fields demonstrates that the vortex state is more difficult to annihilate from the round side, which has been proved by calculation of energy barriers as shown below. Enhanced annihilation field differences

are observed with an increase in the cutting area (enhancement of shape asymmetry). Taking into consideration the relation between the annihilation field and chirality, the chirality of the vortex state can be determined by measuring the annihilation field.

We have also simulated the angular dependence by applying magnetic fields along different angles relative to the cut-edge. Fig. IV.3 (b) shows the simulated hysteresis major loops (black) and typical virgin curves (red) with the angle (β) between the cut-edge and magnetic field being 0°, 45°, and 90°, respectively. The vortex nucleation field and annihilation fields as a function of the relative angles are given in Fig. IV.3 (c)-(d). Despite the monotonic decrease in nucleation field, fluctuations in the annihilation fields are observed. These fluctuations result in $H_{n2} > H_{n1}$ around an angle near 45°, while $H_{n2} < H_{n1}$ observed at an angle far from 45°. This angular dependence of the annihilation fields has been confirmed by the butterfly structure as obtained from FORC measurements, shown previously in Chapter III. [104]

Similar double annihilation fields are also observed in the calculation of Py dots with the magnetic field along the cut-edge. However, both a single vortex and two vortices (two vortex cores existing inside a single dot), which collapse into a single vortex at remanence, can nucleate depending upon the dot size and material parameters, although a single vortex state is the ground state. Unlike the case in which the single vortex prefers to nucleate from the cut-edge, the nucleation of two vortices begins at the round side. Along the major hysteresis loop, the vortex core moves from the round side to the cut-edge, resulting in a smaller annihilation field. Thus, the annihilation fields with $H_{n2} > H_{n1}$ are observed with the nucleation of the two vortices, rather than $H_{n2} < H_{n1}$ that occur with the single vortex nucleation. The coexistence of single vortex nucleation and double vortices nucleation has been observed by MOKE measurements of Py dot arrays having 600 nm diameters, as represented by two groups of annihilation fields both along the major loop and virgin curves. [118]

IV.C Energy barriers between different spin configurations

IV.C.1 Calculation model

By assuming various initial magnetic spin configurations, a local minimum energy at zero magnetic field can be obtained from micromagnetic calculations. The diameter dependence of the local minimum energies with an out-of-plane single domain, an in-plane single domain and an in-plane vortex state are shown in Fig. IV.1 (b). For dots (t=20 nm) with diameters less than 23 nm, an out-of-plane single domain state is more energetically stable than an in-plane single domain state. An aspect ratio of $L/D = 0.87$, corresponding to this critical diameter, is in good agreement with the transition value of $L/D = 0.905$, at which the magnetic easy axis transitions from in-plane to out-of-plane. [26] For a diameter greater than 28 nm, a dot containing an in-plane vortex state exhibits the lowest energy and will thus be the ground state. However, this result disagrees with the simulations for the hysteresis loops, which shows that the single domain to vortex state transition happens at a diameter of 40-60 nm. To resolve this discrepancy, magnetic energies with various spin configurations are calculated under different external magnetic fields.

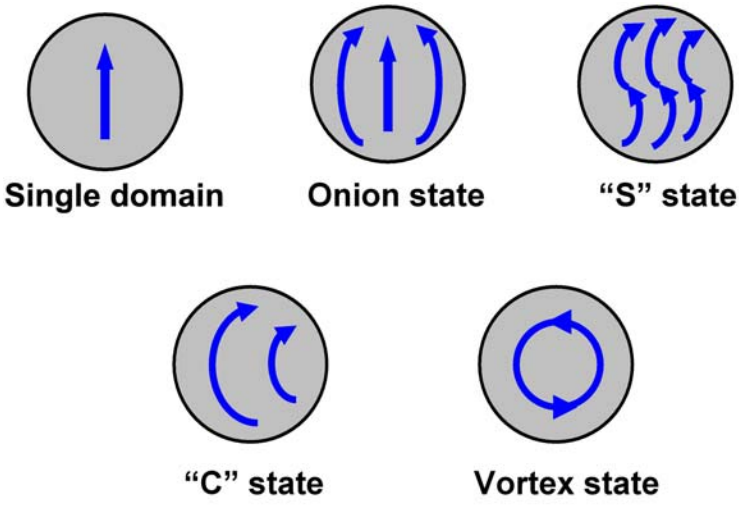

Figure IV.4: Schematic of the five typical spin configurations: single domain, onion, "S", "C", and vortex states.

Now we look carefully at spin configurations transition when an in-plane external field is applied to dots with a diameter of at lest 60 nm and decreased down from 10

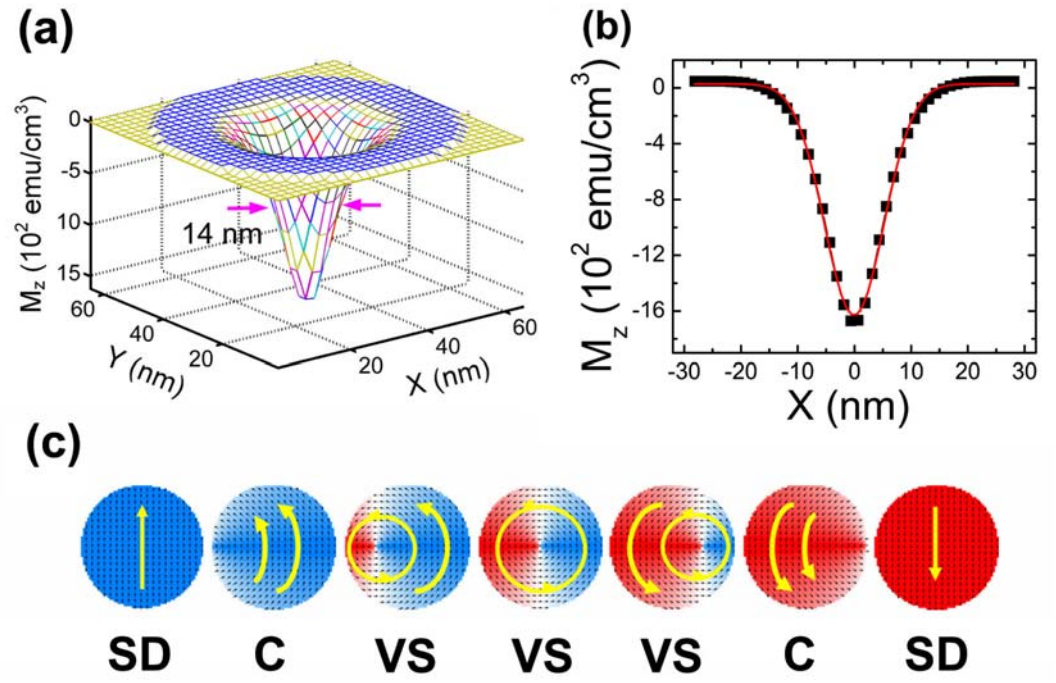

Figure IV.5: (a) Distribution contour and (b) Gaussian fitting of the micromagnetic calculation of M_z for a typical dot with a diameter and thickness of 60 nm and 20 nm, respectively. (c) Various in-plane spin configurations modeled by a shift of the vortex core, where SD, C, and VS represent single domain state, "C" state, and vortex state, respectively.

kOe. In this case, the spin configuration first switches from positive saturation to a "C"-state (as shown in Fig. IV.4), and then to a vortex state at the nucleation field. With a further decrease in external field, the vortex core gradually traverses out of the dot at the annihilation field, finally switching back to the "C"-state again. When the field is decreased down to -10 kOe, the spin configuration transfers back to its saturated single domain state, but now in the opposite direction. [119] In this work, the different spin configurations are built by shifting the vortex core relative to the dot, while the vortex shape is unaffected, similarly to the rigid vortex model. [120] The spin configurations with a vortex core at infinity are used to model the single domain state, while the spin configurations with a vortex core lying inside the dot are used to model vortex states (both core-centered and core-displaced vortex states), and those with a vortex core close to but still outside the dot correspond to "C"-states. All the spin configurations are shown in Fig. IV.5 (c). The single domain and "C"-state, which corresponds to a vortex core lying outside the dot, are composed of in-plane only spins. However, the vortex states are composed of both in-plane and out-of-plane spins within a vortex core.

For the vortex state, the distribution of out-of-plane spins M_z, shown in Fig. IV.5 (a-b), is fitted by a Gaussian distribution, which will then be used to reproduce the spin configurations. The full width at half maximum (FWHM) of the Gaussian distribution is weakly dependent upon the dot diameter and exhibits a value of roughly 12 nm for a 20 nm thick Fe single dot. With a cell size of 1 nm, the vortex spin configurations are built by the following equations:

$$\rho = \sqrt{(x-x_0)^2+(y-y_0)^2} \tag{IV.2}$$

$$M_z = M_s \cdot exp(-4ln(2)\rho^2/2w^2) \tag{IV.3}$$

$$M_y = \sqrt{1-M_z^2}\cdot(y_0-y)/\rho \tag{IV.4}$$

$$M_x = \sqrt{1-M_z^2}\cdot(x_0-x)/\rho \tag{IV.5}$$

where $w = 12nm$ is the FWHM of the Gaussian distribution.

IV.C.2 Results and discussions

The magnetic energies of 20 nm thick Fe dots for these spin configurations are calculated under different external magnetic fields, as shown in Fig. IV.6. With a positive

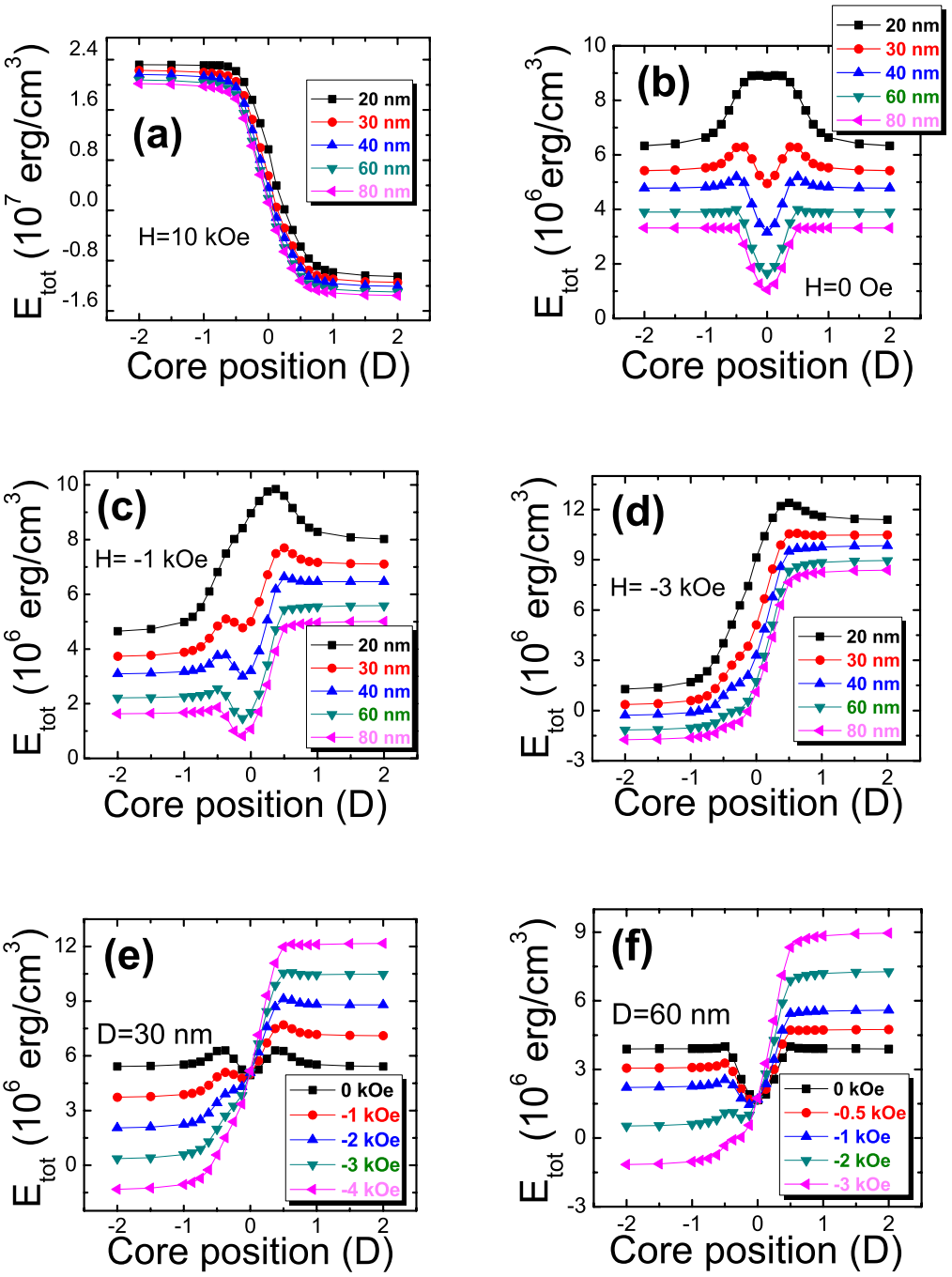

Figure IV.6: Magnetic energy curves of the Fe nanodots with diameters of 20-80 nm under an external field of (a) 10 kOe, (b) 0 Oe, (c) -1 kOe, and (d) -3 kOe. The field dependence of the energy curves for a dot with diameters of (e) 30 nm and (f) 60 nm. The discrepancy between the ground energy calculations and simulations of the hysteresis loops can be explained by the existence of a metastable single domain state.

external field of 10 kOe, a series of tilted energy curves for dots with diameters ranging from 20-80 nm are shown in Fig. IV.6 (a), with the left side (negative magnetization) lifted up. The single domains having positive magnetization exhibit the lowest energies, without other local minima. When the external field is decreased to zero, the single domain state still exhibits a lower energy than the vortex state in the dot with 20 nm in diameter, as shown in Fig. IV.6 (b). However, dots with diameters of at least 30 nm have the vortex state as the global minimum, but with a local minimum energy for the single domain state. For every energy curve, two energy barriers between the two single domain states and the vortex state (VS), [121] during which the vortex core moves either into or out of the dot, are observed. These energy barriers prevent switching between the single domain and vortex states and their heights gradually decrease as the dot diameter increases. Thus, the Fe dots still remain in their initial magnetic states [positive saturation single (PSS) domain states], with the zero magnetic field applied. Upon further decrease of the external field, the energy curves are tilted with the heights of both barriers decreased. Fig. IV.6 (c) shows energy curves generated for a negative external field of -1 kOe. For dots with diameters of at least 60 nm, the energy barriers between the PSS and VS disappear, despite the nonzero energy barrier between the VS and negative saturation single domain state (NSS). Thus, the magnetic states of these dots are transformed into vortex states. However, for those dots having diameters of 40 nm or smaller, PSS states are still exhibited due to the nonzero energy barriers between the PSS and VS. When the external field is decreased to -3 kOe, the energy barrier between the VS and NSS disappears for all dots, while the barrier between the PSS and VS remains for dots with diameters between 20 and 30 nm [shown in Fig. IV.6 (d)]. In this case, the spin configurations have been switched from the VS to the NSS for dots with diameters between 40 and 80 nm, while an even lower external field is required for magnetic switching of those dots with diameters between 20 and 30 nm. Fig. IV.6 (e) and (f) show the energy curves for various external fields for typical dots with 30 nm and 60 nm diameters, respectively. The variation in the energy curves in Fig. 3 clearly demonstrates that the VS can be exhibited for a dot with a diameter of 60 nm, but not for 30 nm. The existence of energy barriers results in a metastable state, which is a single domain state, for a dot with a diameter between 28 and 50 nm, thus preventing

the appearance of vortex states.

IV.C.3 Applications of the energy barrier model

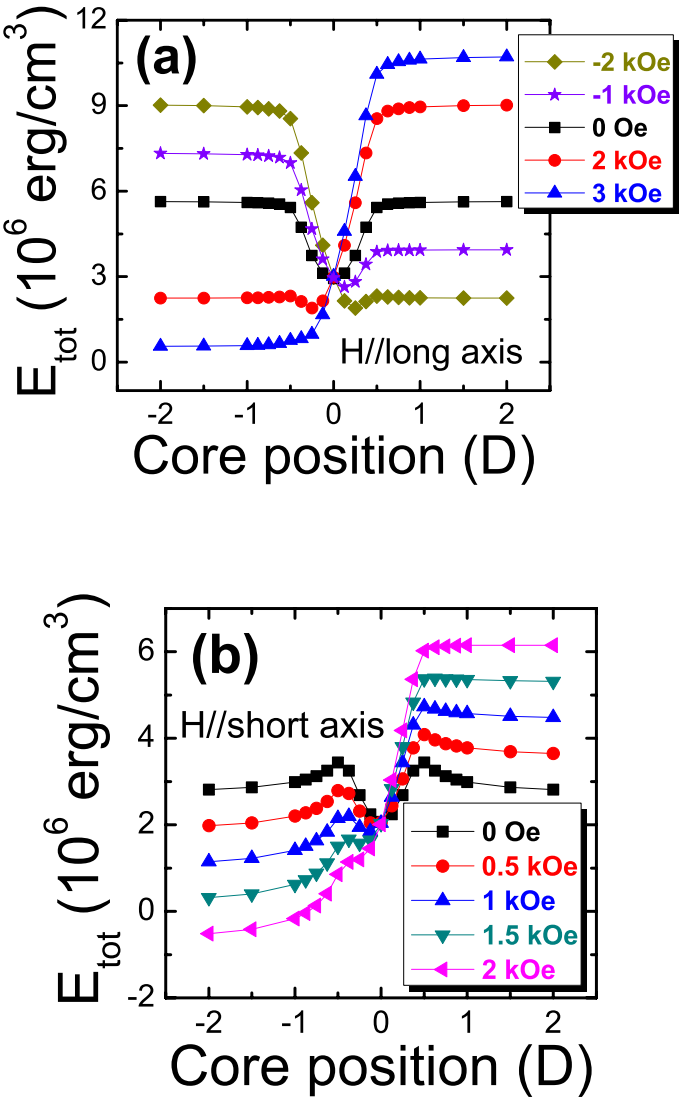

Figure IV.7: Magnetic energy curves of an elliptical dot with the field applied along the (a) 80 nm long axis and (b) 50 nm short axis.

Using this energy barrier model, we can also study the anisotropy effect. For example, shape anisotropy is introduced by the replacement of a circular dot with an elliptical dot, which has a long and short axis of 80 nm and 50 nm, respectively. Fig. IV.7

(a) and (b) show the energy curves for various external fields along the short axis and long axis. When the external field along the short axis is decreased from 10 kOe, the energy barrier between the PSS and VS disappears at a positive field of 1 kOe, thus enabling switching to the VS. Inclusion of shape anisotropy reduces the energy barrier, resulting in a positive nucleation field (vortex state nucleation occurring before zero field). Accompanying a further decrease in the external field, the NSS appears at a field of -3 kOe. However, when the external field is applied along the long axis of the ellipse, only a single domain state is observed and the spin configuration directly switches from the PSS to NSS at a field of -2 kOe, which is due to enhancement of the energy barrier, resulting from the shape anisotropy. Thus, it is expected that the different energy barrier heights for given external field along both the long and short axes contribute to a discrepancy in the magnetic switching, which has been confirmed by magnetic simulations.

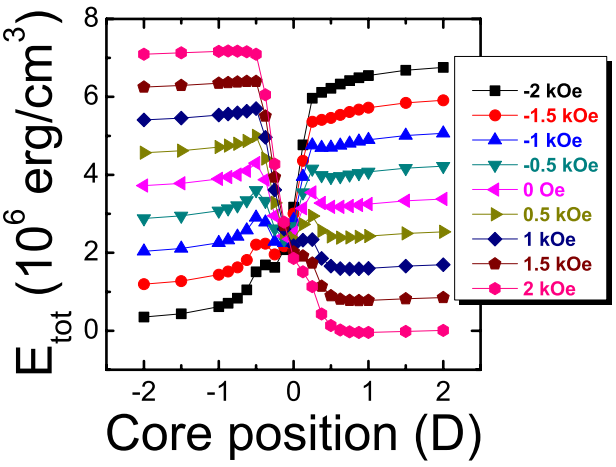

Figure IV.8: Magnetic energy curves of an Fe dot with the asymmetric shape anisotropy (cut-edge). Due to the asymmetric energy with the vortex core moving perpendicular to the cut-edge, the vortex core prefers to move out the dot through the cut-edge rather than the round side, resulting in two different annihilation fields.

When the asymmetric shape anisotropy is introduced through dot cut-edge, the vortex state will annihilate at different magnetic fields, depending upon the movement direction of the vortex core. In order to study the origin of double annihilation fields, we built a series of spin configurations having a vortex moving perpendicular to the cut-edge. The magnetic energies of these spin configurations are calculated in the same way for the

above circular nanodot, shown in Fig. IV.8. For zero external field, an asymmetric energy curve is obtained. The spin configuration with the vortex core closest to the round edge exhibits a relatively higher energy, resulting in a higher energy barrier. Thus, the vortex core prefers to move in (out) of the nanodot through the cut-edge at the nucleation (annihilation) field, resulting in a smaller annihilation field for the vortex core moving out through the cut-edge (along reversal curves).

IV.D Quantitative study of the single domain to vortex state transition

The transition from the single domain to the vortex state has been quantified by the magnetic hysteresis loop width ratio $W_{M=0}/W_{M=0.5M_s}$, where $W_{M=0.5M_s}$ and $W_{M=0}$ are the hysteresis loop width at half of the saturation magnetization and zero magnetization, respectively. The width ratio plotted as a function of the dot diameter (20 nm thick Fe dots) has been given in Chapter III, which shows a width fluctuation with a minimum at an average diameter of 65 nm followed by a maximum at an average diameter of 78 nm. This fluctuation of width ratio should be related to the transition from a single domain to a vortex state, but the origin of the minimum and maximum in the width ratio cannot be obtained directly from either SQUID measurements or current analytical calculations. However, we are able to give a possible explanation by using 2-dimensional micromagnetic simulations.

The calculated loop width ratio of $W_{M=0}/W_{M=0.5M_s}$ is given in Fig. IV.9 (a), which shows a similar curve to these obtained from experimental results and Monte Carlo simulations. The quantitative difference between these simulations and experimental results can be fitted by further adjusting the simulation parameters. To investigate the origin of loop width fluctuation, we simulated magnetic hysteresis loops and snapshots of the spin configurations for Fe dots with a diameter of 60 nm, 69 nm, 78 nm, and 90 nm, respectively, as shown in Fig. IV.9 (b)-(e).

We classify the Fe dots into four different categories based on their diameters. These categories are the following: less than 69 nm, 69-78 nm, 78-84 nm, and larger than 84 nm. A single domain state is exhibited for a diameter less than 69 nm (first category),

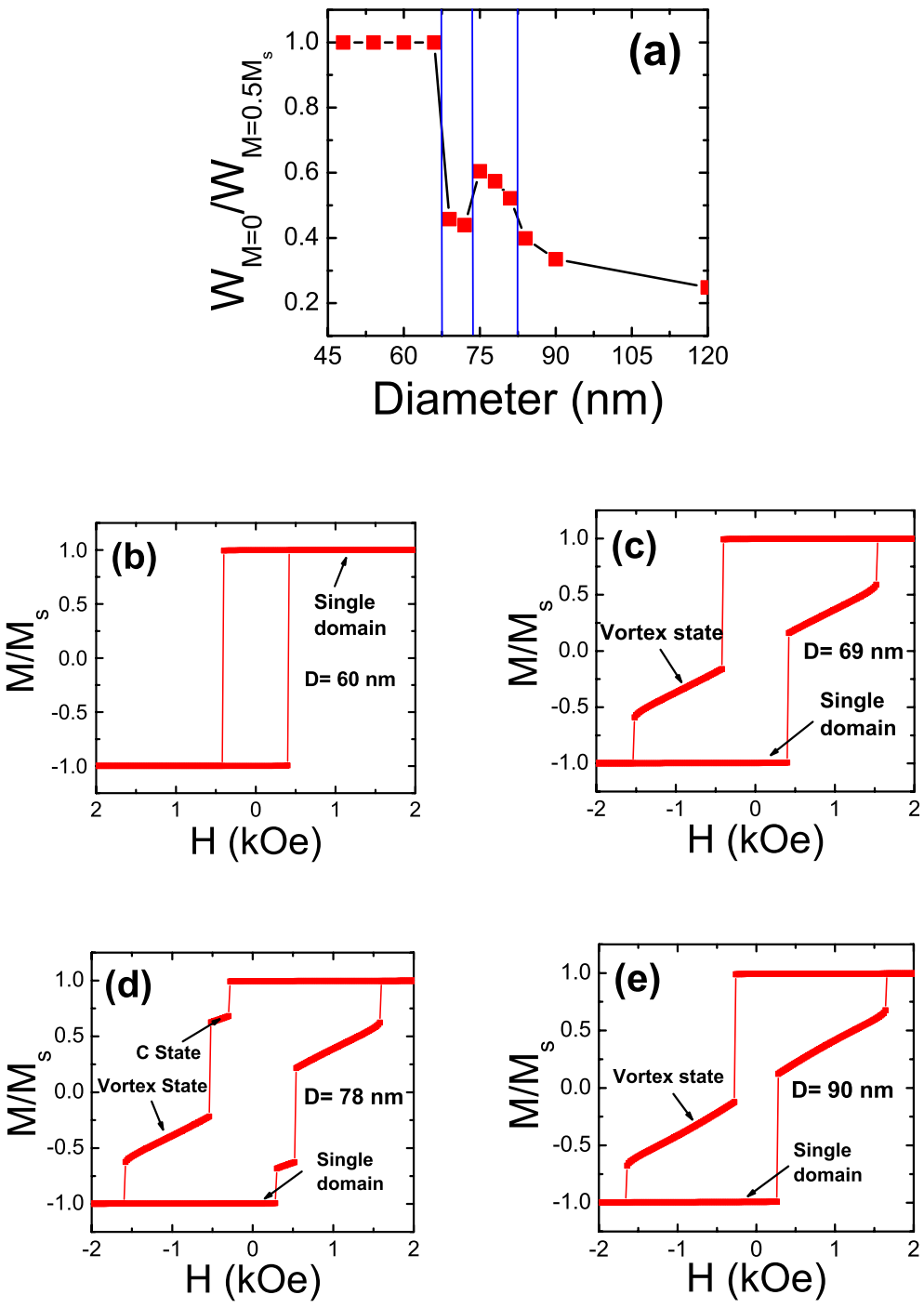

Figure IV.9: (a) The ratio of the hysteresis loop width ($W_{M=0}/W_{M=0.5M_s}$) at $M = 0$ (zero magnetization) and $M = 0.5M_s$ (half of saturation magnetization) as a function of dot diameter; Magnetic hysteresis loops for dots with diameters of (b) 60 nm, (c) 69 nm, (d) 78 nm, and (e) 90 nm.

with square hysteresis loops corresponding to coherent spin rotation. For a diameter of 69-78 nm, a striking decrease in the hysteresis loop width is observed accompanying the spin configuration transition of single domain state→vortex state→single domain state. However, a width ratio peak is observed in the dots with diameters ranging between 78 and 84 nm. This increased width ratio is due to the appearance of two switching fields H_{s1} (from the single domain state to the "C" state) and H_{s2} (from the "C" state to the vortex state), rather than a single switching field (from the single domain to the vortex state), as observed in other categories. This width ratio fluctuation has also been investigated by using Monte Carlo simulations, and shows a similar two switching fields for Fe dots with a diameter between 67 and 78 nm. However, the origin of the second switching field in Monte Carlo simulation is due to the appearance of the "S"-state (as shown in Fig. IV.4), rather than that of the "C"-state, as found in micromagnetic simulations. The simple explanation for the different magnetic reversals is that the energy barrier variations are strongly dependent upon dot diameter. However, we cannot give quantitative calculations of the energy barriers, due to ambiguity in the spin configurations.

IV.E Thickness dependence of spin configuration

Ha and Porrati [114, 115] have predicted the existence of a vortex state with in-plane spins in the vortex core (referred to as an in-plane vortex state) for a dot with a thickness comparable to the dot diameter. To confirm the existence of this in-plane vortex state, we have investigated the thickness dependence for the spin configurations, shown previously in Chapter III, by varying the Fe dot thickness ($D = 76$ nm) from 20 to 100 nm. Additionally, in this chapter the 3-dimensional micromagnetic simulations for an in-plane and out-of-plane magnetic field are used to interpret our SQUID results. In order to do this, dots with diameters of 45 nm and 66 nm are divided into small cells of uniform rectangular cylinders with a length, width, and height of 1.5 nm, 1.5 nm, and 2.5 nm, respectively. Magnetic hysteresis loops are simulated by varying the magnetic field with a field step of ± 200 Oe, starting from the saturated single domain states.

When the thickness of the Fe dots (66 nm in diameter) is less than 30 nm,

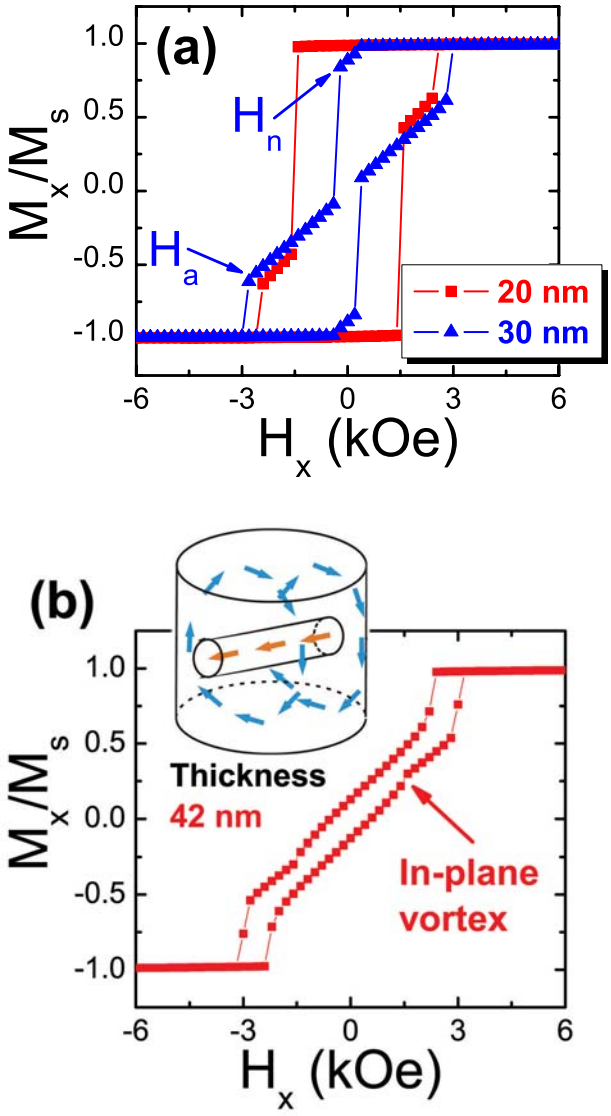

Figure IV.10: (a) Simulated in-plane magnetic hysteresis loops for Fe dots (D=66 nm) with thicknesses of 20 nm and 30 nm, showing an preference of the vortex state as the dot thickness increases. (b) In-plane simulated hysteresis loops of an Fe dot (D=66 nm) with a thickness of 42 nm. The narrow loop width corresponds to the emergence of an in-plane vortex state with the vortex core along the in-plane direction.

the stability of the vortex state is enhanced due to an increase in the dot thickness, with an increase of the field range between nucleation field and annihilation field, as shown in Fig. IV.10 (a). This vortex state preference, which has been confirmed by the SQUID measurements shown in Chapter III, is due to reduction in shape anisotropy (magnetostatic energy) as the dot thickness increases. For a dot thickness above 30 nm (still much smaller than the dot diameter), we observe a transition from the out-of-plane vortex state to the in-plane vortex state, with the two branches of the hysteresis loops being parallel to one another [shown in Fig. IV.10 (b)], even though zero-field energy calculations show that an out-of-plane vortex state has a lower energy than an in-plane vortex state for these dots. Reduced hysteresis loop width (coercivity) is observed as the dot thickness is further increased. This transition is due to a reduction in the Zeeman energy for an in-plane vortex state with the spins inside the vortex core pointing along the magnetic field, resulting in a transition from the out-of-plane vortex state to the in-plane vortex state for a dot thickness still well below the dot diameter. This in-plane vortex state is also observed for Fe dots (45 nm in diameter) with a thickness greater than 30 nm.

More interesting results are given by micromagnetic simulations in which an out-of-plane magnetic field is applied. For a thickness (66 nm in diameter) of 50 nm and smaller, an out-of-plane vortex state is observed with the two branches of the narrow hysteresis loops parallel to one another, similar to the in-plane vortex state caused by an out-of-plane magnetic field. For the dot with a 45 nm diameter and 20-40 nm thickness, an out-of-plane vortex state is also observed with the out-of-plane magnetic field, despite only in-plane single domain state observed from the simulations with in-plane magnetic field applied. Similar to the previous case, the formation of an out-of-plane vortex state, instead of an in-plane vortex state (in-plane single domain state), is due to the reduced Zeeman energy for the spins with an out-of-plane vortex state pointing along the external magnetic field. For a dot (66 nm in diameter) thickness above 50 nm, a pinched hysteresis loop, similar to the typical feature of the out-of-plane vortex state with in-plane magnetic field, is observed. The snapshots for these spin configurations show that the saturated out-of-plane single domain state is first transformed into an unusual out-of-plane vortex state (the spins at the two surfaces of dot rotate with opposite chiralities) as magnetic

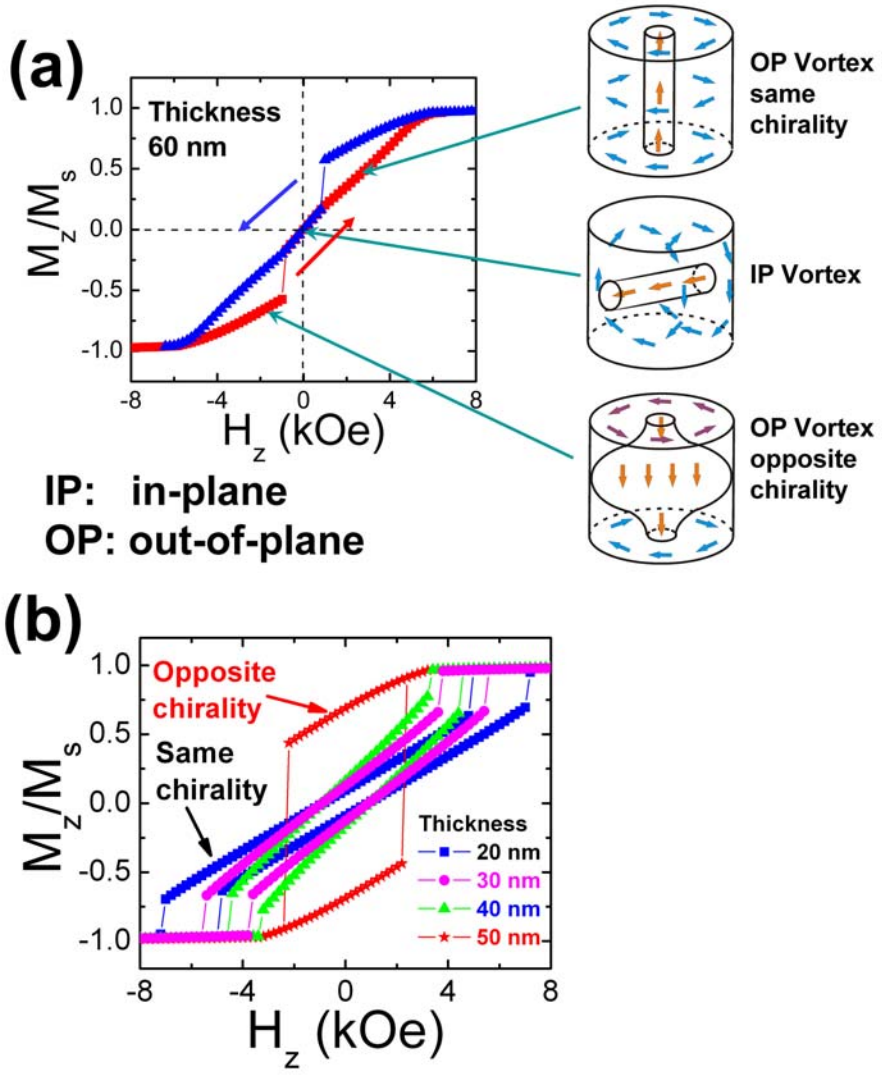

Figure IV.11: (a) Simulated out-of-plane hysteresis loops of Fe dots with a diameter and thickness of 66 nm and 60 nm, respectively. As the magnetic field is increased from negative saturation, spin configurations corresponding to the out-of-plane vortex state with opposite spin chiralities at two surfaces, the in-plane vortex state, and the out-of-plane vortex state with same spin chiralities are observed; (b) Out-of-plane simulated hysteresis loops for Fe dots with a diameter of 45 nm and thickness of 20-50 nm.

field decreases, as shown in Fig. IV.11 (a). The formation of this unusual vortex state is due to the dipolar interaction between spins at the two surfaces. This interaction rotates the spins at the two surfaces in opposite directions. However, energy calculations show that this unusual vortex state is a metastable state, with a higher energy than the normal out-of-plane vortex state (the spins at the two surfaces of the dot rotate with the same chiralities). When the magnetic field is further decreased, the spin configuration is transformed first into another metastable state, an in-plane vortex state, and finally into the normal stable out-of-plane vortex state with the rotation of the vortex core. For the Fe dots with diameters of 45 nm and thicknesses greater than 40 nm, a similar unusual out-of-plane vortex state is also found to be a metastable state as the magnetic field decreases. Further decreasing the field, however, results in a transition to out-of-plane single domain, instead of the normal out-of-plane vortex state, as found previously for the dot with a diameter of 66 nm, shown in Fig. IV.11 (b). Unfortunately, this unusual out-of-plane vortex state has not been confirmed by experimental measurements, which could be due to the distribution of dot sizes and dot interactions in real samples.

IV.F Conclusions

Micromagnetic simulations have been used to investigate the transition of magnetic spin configurations from a single domain to a vortex state. Although the vortex state is the ground state for Fe dots with 20 nm in thickness and the diameter more than 28 nm, the simulations of magnetic hysteresis loops show that a vortex state does not exist for the dot with diameter of 40 nm and smaller. To explain this discrepancy, the magnetic energies of various spin configurations are calculated. This simple model can qualitatively demonstrate magnetic switchings and explain the above discrepancy, which is due to a metastable single domain state resulted by the energy barriers along energy curves. The influence shape anisotropy on the magnetic switchings can also be qualitatively explained by the different height of energy barriers. In addition, the nanodot thickness dependence of spin configurations is also investigated by using a 3-dimensional model, which exhibits the transition from an out-of-plane vortex state to an in-plane vortex state with a increase of dot thickness.

IV.G Acknowledgement

Support by The Air Force Office of Scientific Research is gratefully acknowledged.

V

Interactions between magnetic nanostructures and an adjacent superconducting film

V.A Asymmetric pinning of superconducting vortices by magnetic dots and antidots

V.A.1 Introduction

In Type-II superconductors, superconducting vortices can be formed with quantized magnetic fluxes trapped at defects. The pinning of superconducting vortices at magnetic (nonmagnetic) pinning centers has been investigated comprehensively due to their potential applications and other related scientific interests. [55–59,122,123] To date, the pinning centers of the superconducting vortices are mostly fabricated by electron beam lithography with large pattern spacing, which results in a small first matching field and limits the potential applications especially in the context of high magnetic fields. In our work, magnetic pinning centers (magnetic nanodots or antidots), with spacing of approximately 100 nm, are fabricated using the self-ordered porous alumina masks, which can result in a first matching field as high as 2 kOe. Since these pinning centers cover a macroscopically large area (over 1 cm^2), the flux pinning effect can be

measured by a conventional magnetometry, such as the SQUID magnetometry.

V.A.2 Sample preparation

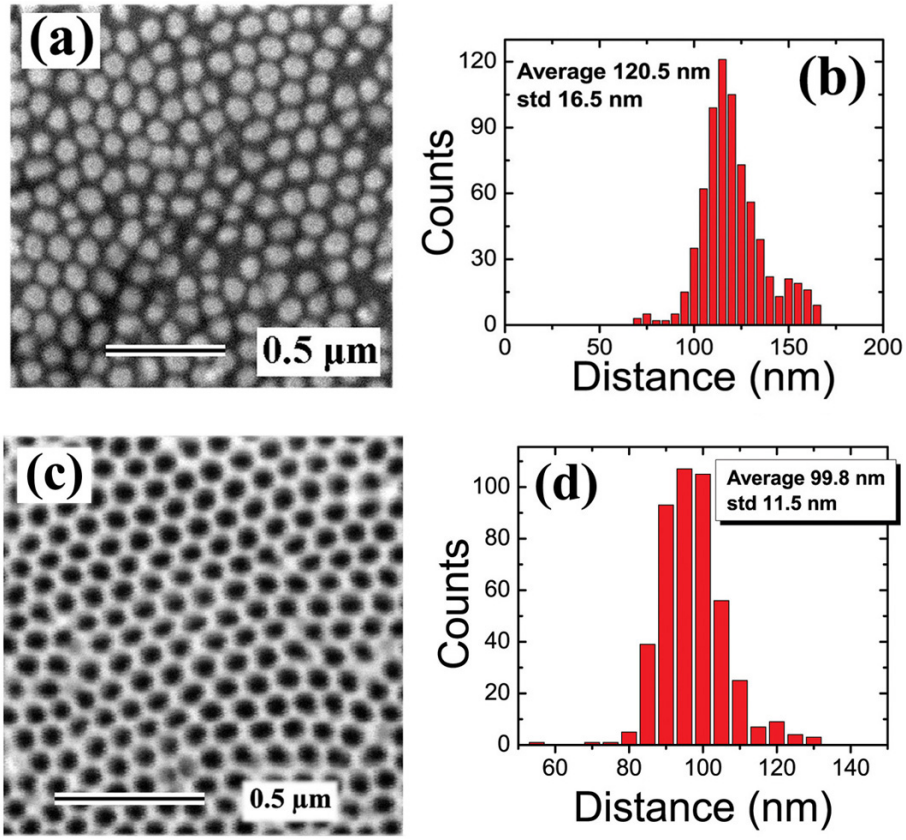

Figure V.1: Typical (a) SEM image and (b) distribution of the dot distances in sample A with 40 nm thick Fe dots, fabricated by using porous alumina anodized under 48 V. Typical (c) SEM image and (d) distribution of pore distances in a porous alumina mask (anodized under 40 V), used to fabricate samples B and C.

The samples are fabricated by evaporating a niobium (Nb) film on top of FM nanodot (sample A) and antidot (sample B, C) arrays. For sample A, 40 nm of the Fe are electron beam deposited, using a 300 nm thick porous alumina (anodized at 48 V) shadow mask. Iron dot arrays [Fig. V.1 (a)-(b)] are obtained after removal of the anodic alumina via a solution of 6.0 wt% phosphoric acid and 1.8 wt% chromic acid. Sample B is an FM antidot array (network) fabricated with 40 nm of FM deposited on top of a 1.5 μm-thick porous alumina mask (anodized at 40 V), as shown in Fig. V.1 (c)-(d). An additional coverage of 10 nm SiO_2 is used to eliminate the proximity effect. To

clarify the magnetic contribution to the flux pinning effect, sample C (with nonmagnetic antidots) is also fabricated with the deposition of 50 nm SiO_2 on top of the same porous alumina mask as sample B. 100 nm thick Nb films are then deposited on top of the pinning centers by molecular beam epitaxy (MBE) with a base pressure below 10^{-9} Torr. Tilted deposition with the beam at 25° to the normal ensures that the Nb film in sample B is well separated from the possible FM dots at the bottom of the pores. The critical temperature of the superconducting film is measured by SQUID magnetometry by gradually increasing the temperature from 4.5 K to 9 K under a small magnetic field of 50 Oe. The temperature at which the magnetization reaches zero is defined as the critical temperature. For samples A-C, the critical temperatures are reduced to 7.25 K, despite the high T_c (8.75 K) of their co-deposited Nb film. This decrease in critical temperature could be due to deterioration from the pinning centers.

V.A.3 Pinning of superconducting vortices as induced by the pinning centers

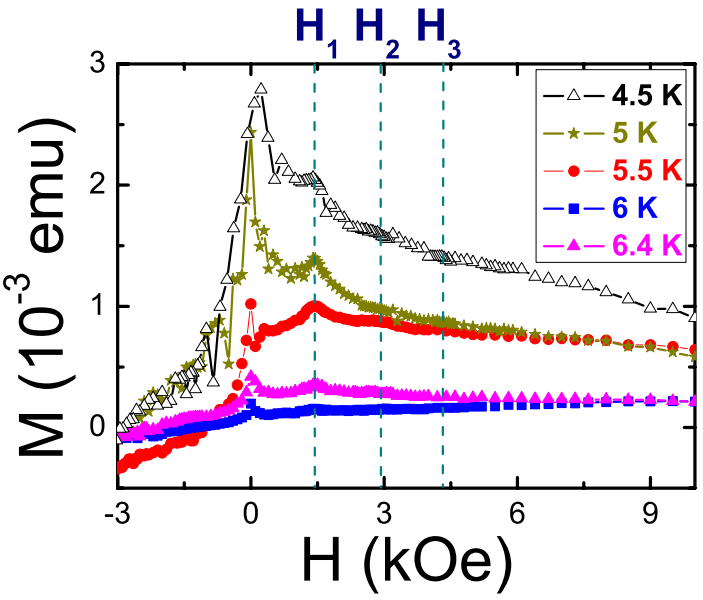

Figure V.2: Magnetic measurements of the superconducting flux pinning effects in sample A with 40 nm Fe dots as the pinning centers at temperatures from 4.5 to 6.4 K. Dash lines are eye guids of matching fields, with the first matching field of about 1450 Oe.

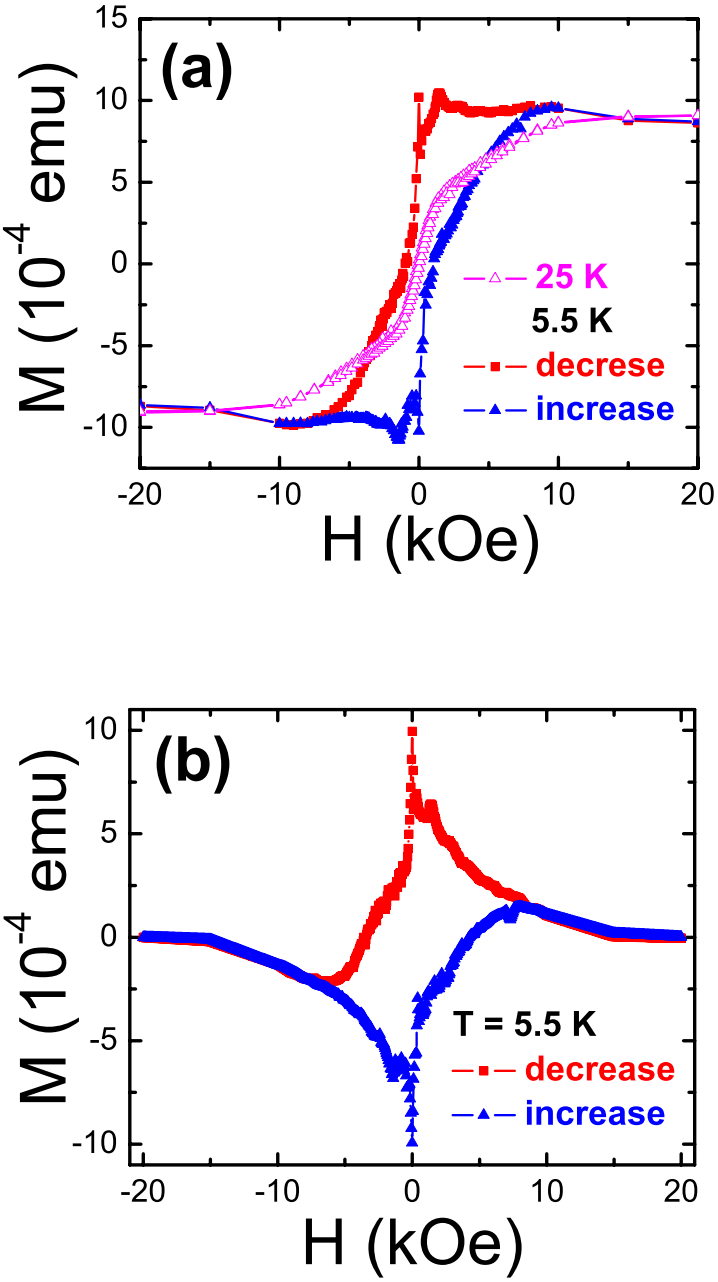

Figure V.3: (a) Magnetic measurements of sample A at 5.5 K (below the critical temperature) and 25 K (above the critical temperature), which exhibit the coexistence of the magnetic signal from both the superconducting film and the magnetic pinning centers; (b) The signal solely from the superconducting layer, obtained after removal of the dots signal. Red squares and blue solid triangles represent the loop branches with the decreasing and increasing magnetic field applied, respectively.

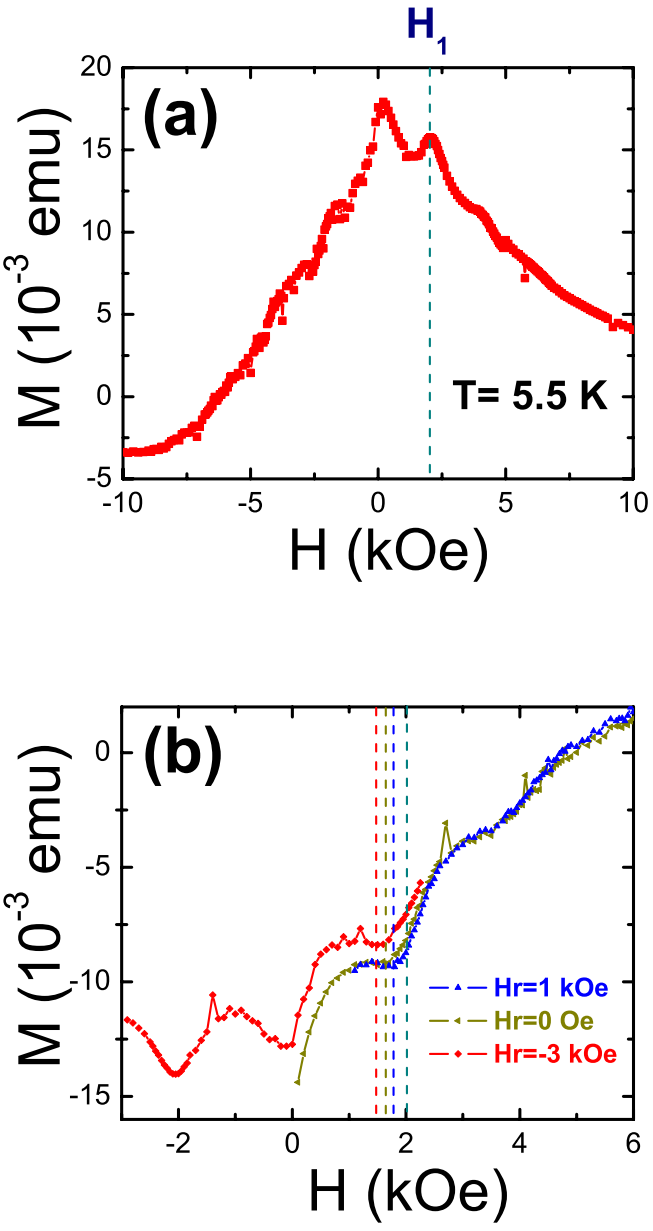

Figure V.4: (a) Magnetic measurements of sample B with 40 nm thick Fe antidots as pinning centers, which show enhanced asymmetric flux pinning when compared to sample C. Dark cyan dash lines are eye guides for the matching fields. (b) The effect of the magnetic dipoles on flux pinning revealed by measuring the reversal curves with reverse fields (H_r) of 1 kOe, 0 Oe, and -3 kOe. Dark cyan, blue, dark yellow, and red dash lines are eye guides for the first matching fields according to the major loop measurement, and minor loop measurements with reversal fields of 1 kOe, 0 Oe, and -3 kOe, respectively.

To study flux pinning, the samples are measured by decreasing and increasing the applied magnetic field after the samples have been saturated at 40 kOe and -40 kOe, respectively. The magnetic hysteresis loops of sample A at a temperature between 4.0 and 6.5 K are measured as shown in Fig. V.2. A clear coexistence of magnetic signals from both the dots (antidots) and superconducting film for sample A is observed. Fig. V.3 (a) shows the full scale hysteresis loop for sample A after removal of the diamagnetic background signal, with the saturation of the samples at a field of approximately 15 kOe. Unlike the typical small magnetic signals found after saturation of the samples, a high magnetic signal comparable to the value of the zero-field peak is observed in our samples. The signal from the superconducting layer is obtained after removal of the dots signal, which is measured at a temperature close to, but above T_c for our samples, as shown in Fig. V.3 (b).

Despite a 10-15% standard deviation from the average pinning center size and distance, strong flux pinning effects are observed in our samples. This is shown by peaks in the magnetization curves, as opposed to the steps mentioned in other references. [55, 60, 61] The positions of the peaks correspond to the matching fields given as H_1, $H_2 = 2H_1$, and $H_3 = 3H_1$. For the sample with hexagonally distributed pinning centers, the first matching field H_1 is given as

$$H_1 = (2/\sqrt{3})(\Phi_0/l^2) \tag{V.1}$$

where Φ_0 is the magnetic flux quantum of 2.0678×10^{-15} T$\cdot m^{-2}$, and l is the distance between pinning centers. Analysis of the SEM image for sample A shows that the average distance is 120.5 nm, which gives a first matching field of 1644 Oe. This calculated matching field is about 13% larger than the experimentally measured value of 1450 Oe, obtained from the first peaks in the magnetization curves. Similar discrepancies have also been observed on other samples, as shown in Table V.1. The origin of these discrepancies has been attributed to the disorder of pinning centers. [61]

To clarify these discrepancies, we have investigated the pinning effects by tuning the magnetic moment with different reversal fields, as shown in Fig. V.4 (b). We first saturate our sample with a high positive field of 60 kOe, and then slowly decrease the field to the various reversal fields of $H_r = 1$ kOe, 0 Oe, and -3 kOe. Pinning effects are

Table V.1: List of first matching fields obtained from experimental measurements and theoretical calculations.

Sample	Distance of pinning centers (nm)	H_1 from calculation (Oe)	H_1 from measurements (Oe)	Discrepancy
A	120.5	1651	1450	12%
B	99.8	2406	2050	15%
C	99.8	2406	2000	17%

measured by increasing the magnetic field from H_r. A slight reduction of flux pinning strength and a decrease in the matching field are observed with a decrease in reversal field and thus a decrease in magnetic moment (more negative) for the pinning centers. This correlation between pinning strength and matching field indicates that the discrepancies could be a result of local maxima shifting along a magnetization curve (due to the intrinsic properties of the superconducting film) with a nonzero gradient.

Unlike the lithographically fabricated samples with pinning center distances greater than several hundred nanometers, the periodicity of our pinning centers is of the same order length scale as the superconducting Nb film. [55, 60] This ensures that the potential energy of the superconducting vortices is dominantly periodic even at very low temperatures. [124] Thus, strong flux pinning in samples A and B is observed over a broad temperature range from 4.0 to 6.5 K, in contrast with the narrow temperature range close to T_c required for lithographically fabricated samples. At high temperature, the increased size of the superconducting vortices results in strong overlapping and interaction between superconducting vortices. This reduces the flux pinning forces. The flux pinning effect is more pronounced at lower temperatures, although weaker pinning and non-monotonic magnetization curves are observed at temperatures below 4.5 K due to avalanches of superconducting vortices. [125–127]

V.A.4 Asymmetric pinning of superconducting vortices as induced by magnetic nanostructures

Striking asymmetric pinning effects are found in samples A and B. Pronounced flux pinning peaks are observed at the right side with $H > 0$, while a sharp decrease in

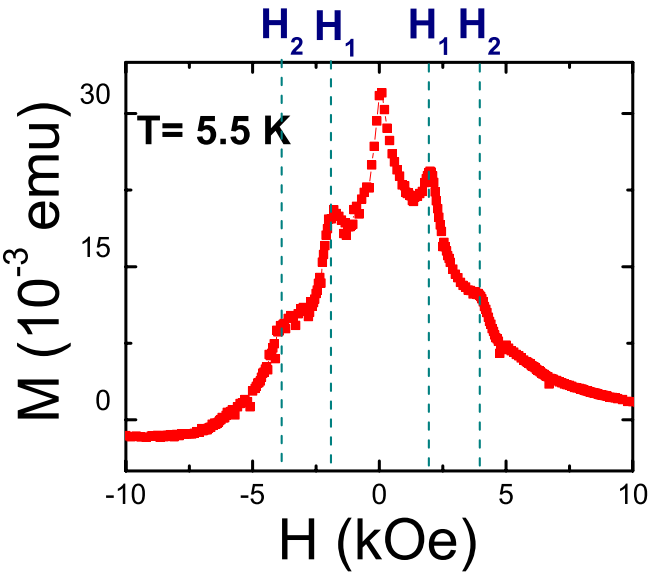

Figure V.5: Magnetic measurements of sample C with a porous alumina mask as the nonmagnetic antidot pinning centers. Dash lines are eye guids for matching fields. A slightly asymmetric flux pinning effect could be due to ferromagnetic impurities or intrinsic properties of the superconducting film.

the magnetic signal without a flux pinning effect are observed at the left side, as shown in Fig. V.2 and Fig. V.4. This asymmetric pinning effect is evidence of a flux pinning force from the local magnetic stray field of dots (antidots). Larger asymmetry is found in samples composed of pinning centers with higher magnetic moments. The asymmetric flux pinning from dots has been attributed to the different locations of superconducting vortices (either strongly pinned at the dot pinning centers or weakly pinned at the interstitial sites), and is affected by the direction of the magnetic flux relative to the magnetic polarity of the pinning center. [128–132] A simple energy calculation of the superconductor/ferromagnets (S/F) system has been implemented by Van Bael *et al.* to explain this magnetic dipolar contribution: $E_{tot} = E_{kinetic} + E_{field} + E_{moment}$. [130] Due to the interaction between the supercurrents and dipoles induced screening currents, E_{moment} is dependent upon the magnetic polarity as

$$E_{moment} = -\int \vec{m}(\vec{r}) \cdot \vec{b}(\vec{r}) d\vec{r} \tag{V.2}$$

where $\vec{m}$ is the magnetic moment of pinning site, and $\vec{b}$ is the local magnetic field due to the flux. With the magnetic moment $\vec{m}$ parallel to the flux field $\vec{b}$, opposite rotation of supercurrents and dot dipole induced screening currents result in a negative E_{moment}. The large magnetic moments at the dots result in a lower energy with superconducting vortices at dots than at interstitial sites. Thus, a pronounced pinning effect is observed, with the superconducting vortices strongly pinned at the dot pinning centers. [128–130] On the other hand, for a positive value of E_{moment}, when $\vec{m}$ is antiparallel to $\vec{b}$, the interstitial positions will be the pinning sites. Weaker pinning forces at the interstitial sites result in a less pronounced flux pinning effect.

One major difference between our samples and Van Bael's samples [130] is the high matching fields ($H_1 = \pm 1450$ Oe in sample A, and $H_1 = \pm 2150$ Oe in sample B) and relatively small coercive field of pinning centers for our samples. The magnetic measurement at a temperature of 25 K (well above the critical temperature of the superconducting layer) shows that the coercivity of FM dots in sample A (antidots in sample B) is below 100 Oe (700 Oe) when an out-of-plane field is applied. Unlike the fixed magnetic moment with small matching fields as reported in Van Bael's paper, the magnetic moments of sample A are 3.6×10^{-4} emu and -3.2×10^{-4} emu at the first positive and negative matching fields. The magnetic moments are parallel to the external magnetic field at the both sides, which should result in similar strong flux pinning. So far, a clear interpretation of the strong asymmetric flux pinning in samples A and B is still missing.

V.B Bistability of a superconducting film induced by magnetic vortices

V.B.1 Introduction

The role of spin configurations on the pinning effects has been investigated in a hybrid system of FM/AF. In that system, the magnetic spin configurations of FM dots can be imprinted into the adjacent AF layer when the exchange coupled system is cooled below T_N of the AF material. [133,134] In this work, we propose a novel S/F structure in which the ferromagnetic characteristics are imprinted into the superconducting transport properties by magnetic stray fields. [62, 135]

V.B.2 Sample preparation and corresponding magnetic properties

Arrays of Fe dots (20 nm thick) covered with a Au capping layer (1 nm thick) are fabricated on n-type Si substrates using nanoporous alumina as shadow masks. Three FM dot arrays A ($D = 55\pm5$ nm, $l = 85\pm20$ nm), B ($D = 75\pm5$ nm, $l = 120\pm20$ nm) and C ($D = 140\pm20$ nm, $l = 180\pm40$ nm), where D and l are the dot diameter and distance (center-to-center), are then covered with a superconducting Al thin film, either 20 or 40 nm thick. A standard four-probe bridge for magnetotransport measurements is defined using optical lithography and ion etching. The superconducting critical temperatures are found to be around $T_c = 1.40 \pm 0.02$ K for all samples.

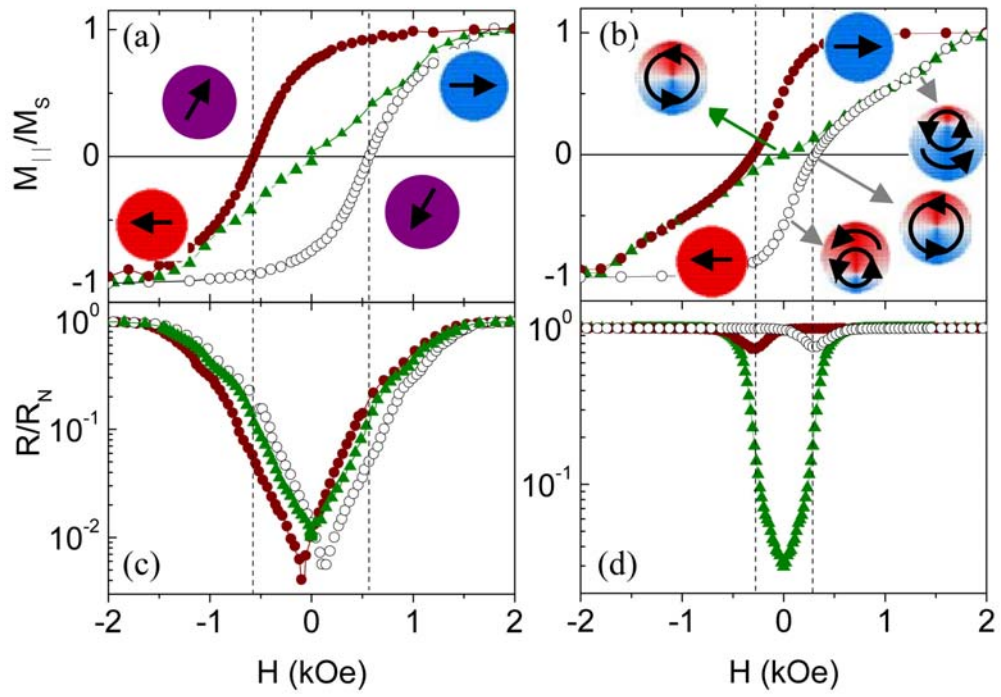

Figure V.6: Normalized magnetization vs. in-plane applied field for (a) sample A and (b) sample C at T=6 K (M_s saturation magnetization). Normalized resistance vs. in-plane applied field for (c) sample A and (d) sample C (R_N normal-state resistance), at T=1.25 K =0.89 T_c with J=25 kA$\cdot$ cm^{-2}. Hollow (white) and solid (brown) dots are for curves measured starting from negative and positive saturation, respectively. Triangles (green) represent the virgin curves. The negative branches of the $M_{//}$(H) virgin curves are mirror images of the positive ones. Vertical dashed lines point out coercive fields. The sketches are cartoons of the reversal mechanisms. (After Ref. [62]).

Magnetic properties of FM dot arrays are measured using SQUID magneto-

metry with an in-plane external magnetic field and at a temperature of 6 K. The major hysteresis loops and reversal curves are shown in Fig. V.6. The hysteresis loop for sample A [Fig. V.6 (a)] corresponds to magnetic reversal of a single domain state with coherent rotation of magnetic spins. Meanwhile, the hysteresis loops of samples B and C exhibit a pinched neck around zero remanence, [Fig. V.6 (b)] which is a feature characteristic of a magnetic vortex state. When the magnetic field is decreased, this magnetic vortex state is formed at the nucleation field of $H_n \approx -100$ Oe, and transformed back to a single domain state in samples B and C at the annihilation field of $H_a \approx 1.5 - 1.25$ kOe. Due to the distribution of dot sizes and dipole interactions between neighboring dots, there is a wide distribution of annihilation and nucleation fields, with full-width at half-maximum of $\sim$0.5 kOe, which has been observed in the FORC measurements. Minor loop and reversal curve measurements exhibit the reversible properties of a vortex state in samples B and C within the field range of $H_n < H < H_a$. A detailed discussion of the single domain and vortex state has been given in Chapter III.

V.B.3 Magnetoresistance measurements and discussion

DC magnetotransport measurements are done in a liquid He cryostat mainly with the magnetic field applied along the in-plane direction. Figs. V.6 (c)-(d) show the magnetoresistance of sample A and B, as a function of the applied magnetic field at $T = 1.25$ K$= 0.89T_c$, with the current $J = 25kA \cdot cm^{-2}$ injected parallel to the field. The solid (brown) and hollow (black) data are measured from positive to negative saturation (with $H_c \approx 2.5$ kOe) and vice-versa, respectively. Triangles (green) are for the "virgin" curves with measurements performed from zero magnetization to positive (negative) saturation.

Sample A exhibits a similar magnetoresistance [Fig. V.6 (c)] when the field is swept from positive to negative saturation (or vice versa) or when swept from zero field to saturation after a demagnetizing cycle. For lower fields, a several orders of magnitude drop in resistance characterizes the transition into the superconducting state, with a gradual transition into the normal state as the applied field is increased above H_{c2}. Samples B and C exhibit a strikingly different behavior [see Fig. V.6 (d)]. When the field is swept from positive (or negative) saturation, the resistance remains close to normal-

state values at all fields, with small minima around the coercive fields (at H_c ∼0.5 and ∼0.3 kOe for samples B and C respectively). After a demagnetizing cycle (triangles), a deep superconducting transition takes place, similar to sample A. Depending on the magnetic history, two different resistances high (R_h) and low (R_l) are found for a fixed applied magnetic field within a certain range. The typical reversal properties of FM dots are also dramatically imprinted into the magnetotransport of this hybrid system. For samples B and C, the linear reversible response of FM dots near the origin in the virgin curve [triangles (green) in Fig. V.6 (b)], which corresponds to the reversible vortex core motion within the nanodots, is imprinted into the magnetoresistance with the reversible magnetoresistance curve [triangles (green) in Fig. V.6 (d)] when the field is swept back and forth. This reversible behavior is lost after the applied field exceeds ∼1.5 and ∼1.25 kOe (annihilation fields of FM dots) for arrays B and C, respectively.

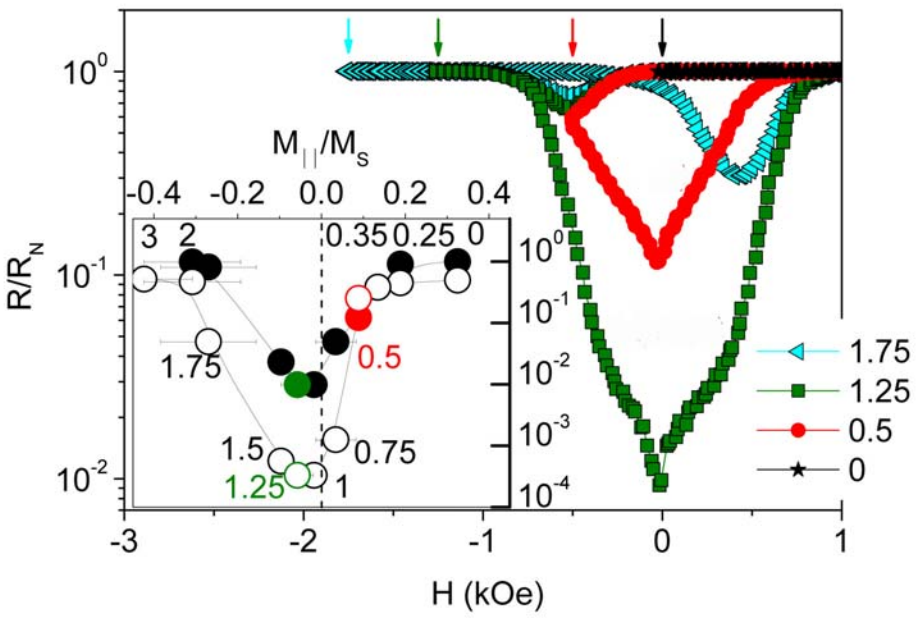

Figure V.7: Normalized resistance vs. in-plane applied field for sample B at T=1.25 K=0.89 T_c (R_N normal-state resistance) corresponding to different cycles with different $|H_r|$ (legend in kOe) after saturation at H_s=2.5 kOe. The vertical arrows point out H_r. Inset: Normalized resistance vs. normalized in-plane magnetization (M_s saturation magnetization) at zero applied field. Each point corresponds to a different cycle ($|H_r|$ indicated by the numbers close to each point). Lines are eye guides. (After Ref. [62]).

The relation between resistance $R(H)$ and magnetic moment $M_{//}(H)$ is also

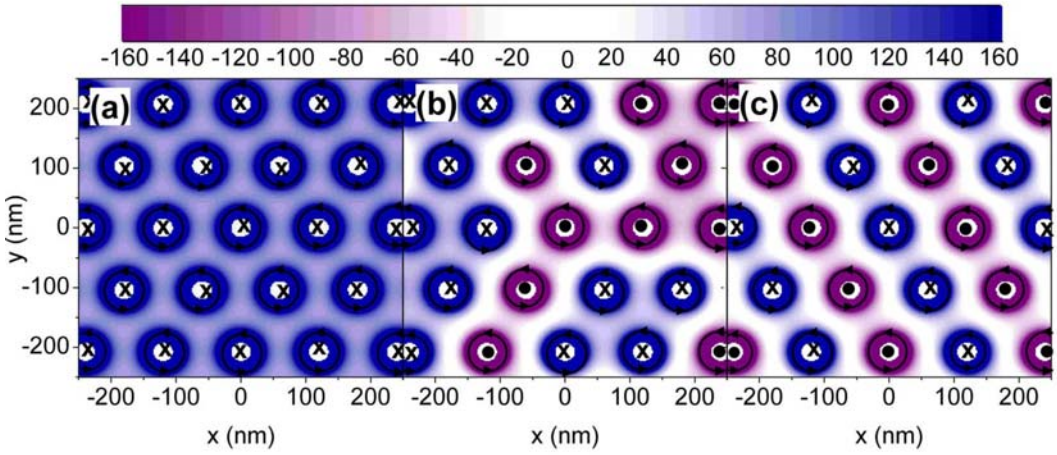

Figure V.8: (a) Magnetostatic calculations of the out-of-plane stray field $H_{\perp}(x,y)$ produced by the vortex cores for distributions in which all vortices have the same polarity (all point down). The legend for $H_{\perp}(x,y)$ in Oe is shown as a color grade bar above graphs. Calculation is made with the parameters of array B (b) same as in (a) for a random distribution of vortex polarities (crosses for down, black dots up). (c) Same as in (a) for an antiferromagnetic arrangement of the vortex polarities. (After Ref. [62]).

investigated. The resistance $R(H)$ is measured, after applying a positive saturating field H_s, as the field is decreased to a reversal field H_r and then swept back to positive saturation, as shown in Fig. V.7. $M_{//}(H)$ is independently measured for the same cycles (not shown). Using values for $R(H)$ and $M_{//}(H)$, which are measured as described above, we obtain resistance as a function of the in-plane magnetization, i.e. $R(M_{//})$, for any field H. A strong asymmetry, with $R(-M_{//})$ two to four orders of magnitude lower than $R(M_{//})$, implies that besides the in-plane magnetization $M_{//}$ an additional "hidden" variable (linked to the magnetic history) leads to this unusual behavior. The only neglected magnetic variable is the out-of-plane magnetization $M_{\perp}$ in the vortex cores, therefore it must play a significant role.

To evaluate the effect of $M_{\perp}$ on the superconducting film we calculate the out-of-plane magnetic field $H_{\perp}$ produced by the vortex cores and compare it to the superconducting critical field H_{cr}. [136] The magnetic field profiles obtained are strongly dependent upon the distribution of the vortex core polarities. We have studied the field profiles for the following three different polarity distributions: (a) all the vortices have the same polarity, (b) a random distribution of polarities, and (c) an antiferromagnetic

(AF) arrangement of polarities. If all the magnetic vortices have the same polarity [Fig. V.8 (a)], $H_\perp > H_{cr}$ everywhere between the dots, the Al film is expected to be in the normal state. With a random distribution of polarities [Fig. V.8 (b)], $H_\perp < H_{cr}$ between vortices with opposite polarity, there is a significant percentage of superconducting "channels" (20±2% of the space between dots) and so, even if not enough to allow percolation, a low finite resistance is expected. Finally, for an AF distribution [Fig. V.8 (c)] $H_\perp < H_{cr}$ in 36±2% of the space between dots, and therefore percolation and zero resistance is expected. Taking into account the distribution of dot sizes and interactions between neighboring dots, Fig. V.8 should not be taken literally as a situation in real samples. However, these calculations show that a transition from higher to lower resistance is expected as the polarity distribution changes from one with the same polarity for the majority of vortices to the other in which 50% of the vortices point up/down. The high-resistance state observed as the external field is reduced from saturation implies that a majority of vortices nucleate with equal polarity [Fig. V.8 (a)]. Although this is in principle unexpected (a 50% up/down polarity distribution is energetically favorable), it can be caused by the unavoidable misalignments between the applied field and the array plane, as shown by micromagnetic simulations in which $\sim 4^\circ$ misalignment produces 85% of the vortices with the same polarity. The low-resistance implies a balanced population of polarities (50% up/down). As the applied field is reduced further to H_r close to the vortex annihilation fields and then reversed, only a fraction of the vortices are annihilated. As the field is reversed these nucleate with opposite polarity so as to reduce magnetostatic interactions with their neighbors, and, due to the external field misalignment, now favors the opposite polarity. Thus, these minor loops yield a balanced population of polarities [Fig. V.8 (b)-(c)]. Since the polarity distributions only change through annihilation/nucleation processes, the low-resistance state is reversible as long as the applied field is below the annihilation field for the majority of the vortices.

Magnetotransport measurements have also been performed with the sample manipulated by various out-of-plane magnetic fields. After saturation with a negative field of -20 kOe, various positive fields (H_z) are applied to tune the magnetic spin configurations of the FM dots. Magnetoresistances are measured by sweeping the in-plane field from -150 Oe to 150 Oe after removal of the positive fields H_z. Fig. V.9 (a) shows

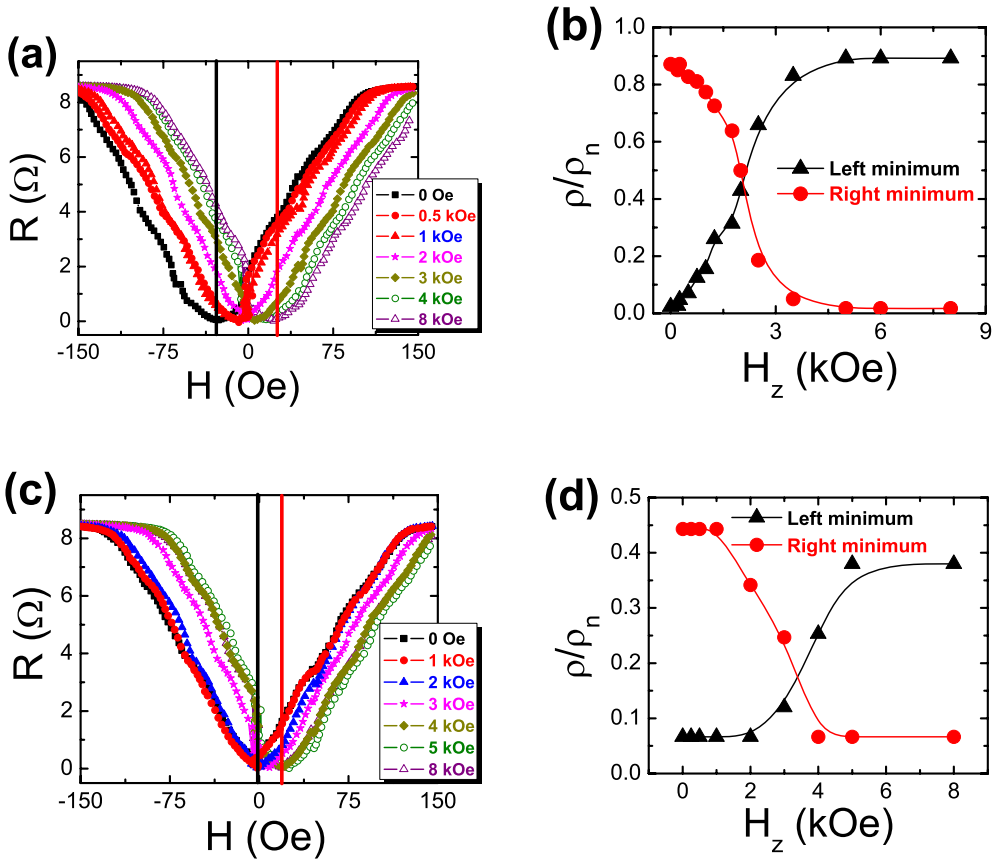

Figure V.9: In-plane magnetoresistance measurements of (a) sample B and (c) sample A after the samples are manipulated by various out-of-plane magnetic fields. Normalized magnetoresistance as a function of out-of-plane manipulation fields for (b) sample B and (d) sample A.

the magnetoresistance curves for sample B as functions of the sweeping fields. Magnetoresistance at a fixed field (corresponding to positive and negative minima) is shown in Fig. V.9 (b) as a function of H_z. The transition from high resistance to low resistance (or vice versa) is related to polarity switch of the vortex cores. For sample B, the vortex cores start to switch polarity at $H_z = 1500$ Oe. At $H_z = 4000 - 5000$ Oe, the polarities of over 90% of the cores have been switched. However, the out-of-plane measurement of sample A gives a similar result to sample B and C, [as shown in Fig. V.9 (c) and (c)] despite the difference in the in-plane measurements. This discrepancy can be explained by the micromagnetic simulations with in-plane and out-of-plane applied fields as discussed in detail earlier in Chapter IV. For samples with larger dots, a vortex state is formed for both the in-plane and out-of-plane fields. For samples with smaller dot, such as the 45 nm diameter dots, a single domain state is exhibited for the in-plane magnetic field, while a vortex state is formed with the out-of-plane magnetic field in order to reduce Zeeman energy (vortex core parallel with magnetic field).

V.C Conclusions

Strong flux pinning effects have been observed in S/F samples with FM dots and antidots as the pinning centers, despite a 10-15% standard deviation in dot diameter and periodicity. The observed asymmetry in flux pinning, which is dependent upon the direction of the magnetic moments of the dots relative to that of the flux field, clearly demonstrates the significant role of magnetic dipole in flux pinning. In addition, we have found that the properties of magnetic vortices can be imprinted into the transport properties of superconducting (Al) thin films. This dramatically modifies the behavior of the superconductor, for which magnetoresistance and magnetization show similarly reversible or irreversible behavior. These effects are induced by out-of-plane magnetic fields produced by the magnetic dots, including stray fields from single domain dots and out-of-plane fields from vortex cores.

V.D Acknowledgement

Support by The Air Force Office of Scientific Research is gratefully acknowledged.

VI

Other applications of porous alumina

VI.A Introduction

In Chapter II, we used anodic porous alumina as a shadow mask for the fabrication of magnetic and nonmagnetic nanodots. The self-ordered porous structure with well controlled pore size, large pattern coverage, and low cost proves that porous alumina is a good candidate for nanofabrication techniques to replace conventional electron beam lithography. The capability to fabricate porous masks with a periodicity less than 20 nm, which exhibit pore density in excess of 10^{12} per square inch, suggests potential applications of this fabrication method towards ultrahigh density recording media. In Chapter V, the pores in porous alumina and nanodots have also been used as the pinning centers for an adjacent superconducting film, which can enhance the critical currents and magnetization at matching fields. In this chapter, I want to discuss the application of porous alumina as sensing devices. [137–139]

Due to the large surface to volume ratio, porous materials have been widely investigated as chemical sensing and biosensing devices. [140,141] When chemical vapors or biomolecules are adsorbed inside the pores, a dramatic change in the electrical or optical properties of porous materials can be detected. In this work, we investigate the porous samples by monitoring a change in the refractive index n with a sensitive

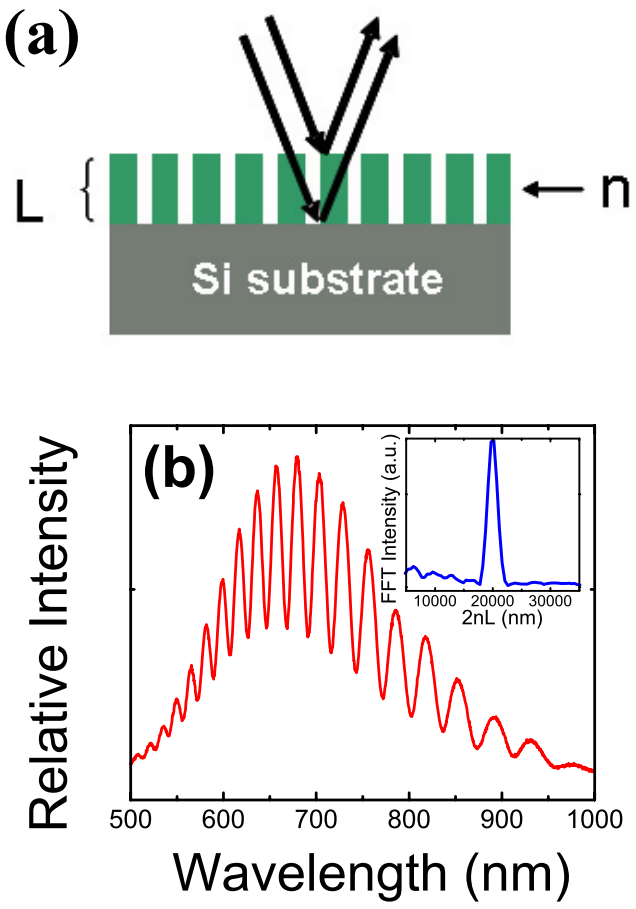

Figure VI.1: (a) Schematic of Fabry-Pérot interferometer; (b) Reflectance spectrum of a typical porous alumina sample with an pore diameter of 13±3 nm. Inset: Fast Fourier transform (FFT) of the spectrum, with the peak corresponding to the effective optical thickness (2nL) of the layer. (After Ref. [137]).

optical interferometer. The spectra shows a series of interference fringes arising from the interference between light reflecting from the top and bottom interfaces of the porous samples. Because the pore diameter is much smaller than the light wavelength λ, the porous layer acts as a single medium with an average refractive index. The fringe maxima are described by the Fabry-Pérot relationship $m\lambda = 2nL$, where m is an integer and L is the thickness of the porous layer. The term $2nL$ is the effective optical thickness of the porous layer, which can be obtained directly as the fast Fourier transform (FFT) peak position, as shown in Fig. VI.1. Filling the pores with an analyte results in a change in n, which causes a shift in the FFT peak position. [140–142]

This optical interferometry method has been widely used by Sailor *et al.* [140–142] to investigate the function of porous silicon (PS) as a sensing device. However, severe degradation due to silicon oxidation reduces the repeatability and reliability of PS sensing devices. Additional treatments to PS, such as pre-oxidation, are required to reduce this degradation. Moreover, it is very difficult to fabricate PS with pore diameters larger than 10 nm, which limits its application towards biosensing, as the size of biomolecules are often larger than 10 nm. In addition, PS materials are not ideal candidates for the investigation of the basic mechanism of porous sensing, due to their disordered and interconnected pores. [143, 144] In this work, we present a study of the capillary condensation of organic vapors within nanoporous alumina with pores open at one end and well controlled sizes in the 10 to 60 nm diameter range.

These porous alumina samples are prepared by anodizing aluminum films on n-type Si substrates, with the pore size and periodicity being controlled by anodization voltages and as well as additional acid etching as described previously. The alumina thickness is at least 6 μm thick so as to ensure that the FFT peaks occur well above the low frequency noise. The distribution of the pore diameters are measured using the field emission SEM, which reduces the charging that generally occurs in conventional SEM , thus enhancing resolution and image quality. Cross-sectional SEM images show that the pores are cylindrical, open at one end, and disconnected (see Fig. VI.2). The stability of porous alumina is confirmed by recovery of a stable base line after filling with gas molecules or phosphate buffered saline (PBS) solution, used as the solvent for the biomolecules. For example, a stable base line with constant effective thickness is

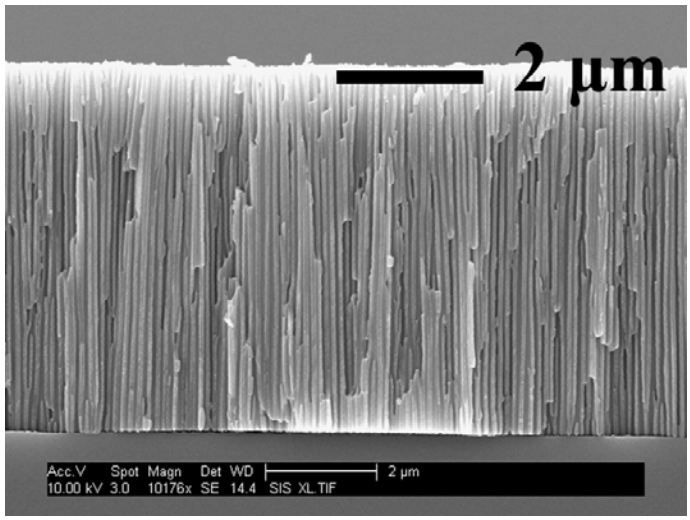

Figure VI.2: Typical cross-sectional SEM image of a porous alumina mask (anodized at 48 V). (After Ref. [137]).

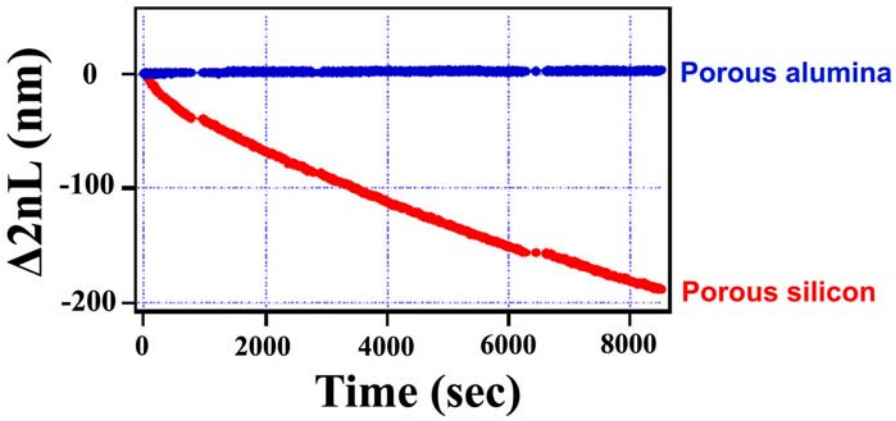

Figure VI.3: Optical interferometry measured base lines of typical porous alumina (blue) and porous silicon (red) with filled by phosphate buffered saline (PBS) solution.

observed in a typical porous alumina sample after filling of PBS solution for more than 2 hours, while a striking drift in the baseline is usually observed in PS samples due to chemical etching from the PBS solution, as shown in Fig. VI.3.

VI.B Gas sensing and capillary condensation

VI.B.1 Capillary condensation

Gas dosing is performed by bubbling pure N_2 through a liquid analyte at 25 °C and subsequently diluting the saturated vapor with pure N_2 using a computer-controlled gas dosing system. The total gas flow is kept constant at 500 standard cubic centimeter per minute (sccm). Relative vapor pressures, P/P_s, where P_s is the saturation vapor pressure, were calculated using the standard vapor pressures of the liquids and the dilution ratio of the gas dosing system.

All samples exhibit isotherms with the same shape and the presence of hysteresis. The initial part of the curve (low P/P_s) is attributed to monolayer-multilayer adsorption on the internal surfaces of the pores. A steep increase in slope is associated with capillary condensation within the nanopores, followed a plateau at high P/P_s as the pores become completely filled with liquid. [145, 146] In our case, the sharpness of the transition is attributed to the narrow pore diameter distribution. The relative pressure at which the transition occurs depends upon both the pore size and the analyte (see Fig. VI.4). Since the pore size and their dispersion are relatively small, we first analyze the desorption curve because this is expected to be independent of uncontrolled features at the pore surface such as roughness, slight variations in shape, possible contaminants etc. [147, 148] To describe the capillary behavior, we use the Kelvin equation [145, 149] with the assumption of a hemispherical meniscus:

$$ln(\frac{P}{P_s}) = -\frac{2\gamma V_L}{RTr_m} \tag{VI.1}$$

where r_m is the radius of the meniscus (equal to the pore radius in our case), R is the ideal gas constant, and V_L and γ are the molar volume and surface tension of the liquid at temperature T. The analytical Kelvin equation (dashed and solid lines in Fig. VI.5), using standard values of V_L and γ for each analyte, is in excellent agreement with the

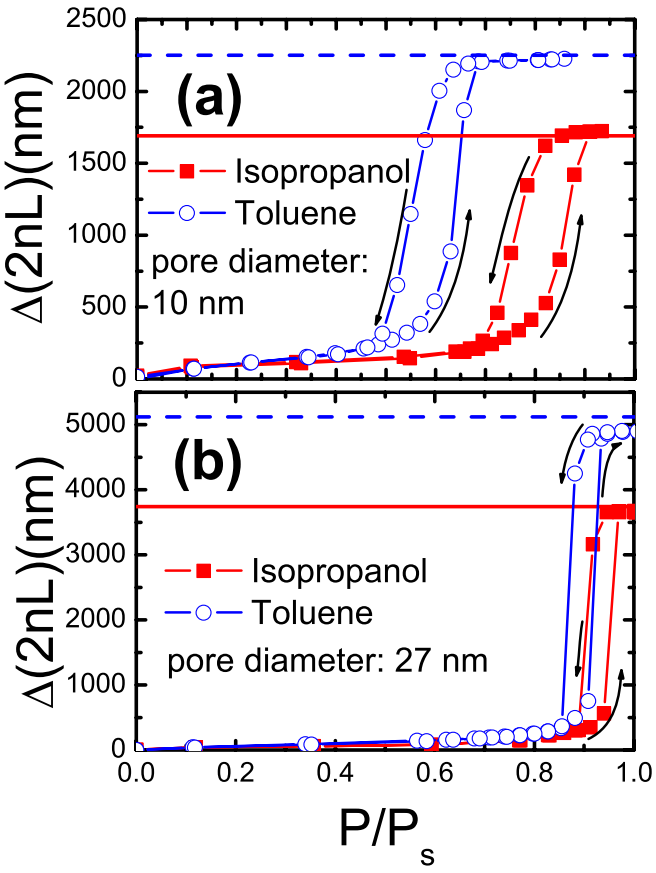

Figure VI.4: Change in 2nL as a function of the relative pressure of an analyte (solid squares for isopropanol and open circles for toluene). Curves are obtained by first increasing (adsorption) and then decreasing (desorption) the relative pressure in discrete steps. Pore diameters of the samples are 10±2 nm (upper panel) and 27±3 nm (lower panel). Horizontal lines correspond to the change in 2nL measured by using the analytes in liquid phase (solid line for isopropanol, dashed line for toluene). (After Ref. [137]).

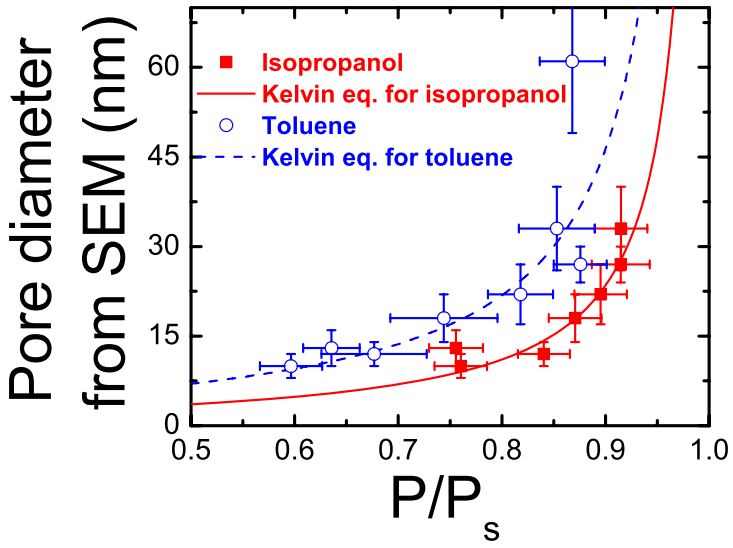

Figure VI.5: Pore diameter obtained from SEM as a function of the relative pressure of the analyte (solid squares for isopropanol, open circles for toluene) at which capillary evaporation takes place. The value is taken as the inflection point of the desorption branch. Solid and dashed lines correspond to the Kelvin equation for isopropanol and toluene, respectively. (After Ref. [137]).

experimental measurements. It is important to stress that the agreement between the experimental data and the Kelvin equation is obtained without any fitting parameters, modeling of the adsorbed film or other considerations.

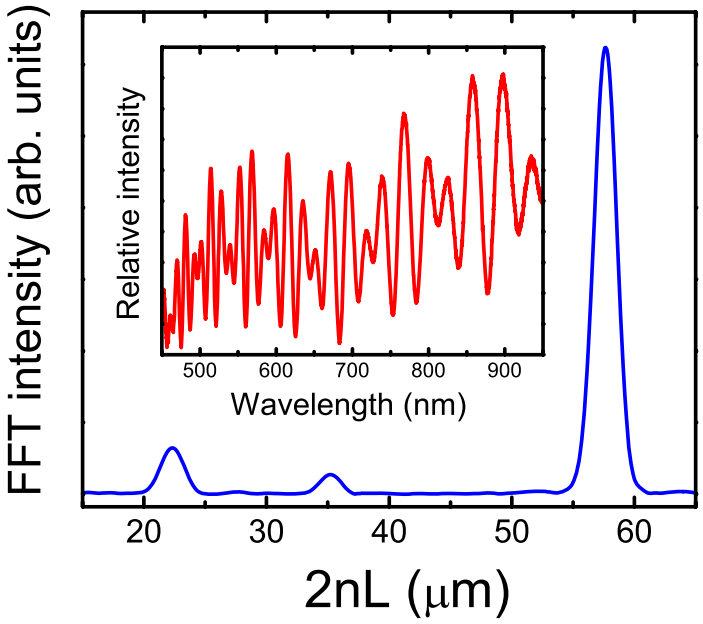

Figure VI.6: FFT of the spectrum, with three peaks corresponding to the effective optical thickness of the top layer, bottom layer and entire sample, respectively. Inset: reflectance spectrum of the bilayer sample. (After Ref. [150]).

VI.B.2 Study of the effect of pore morphology upon capillary condensation through use of porous alumina bilayer

To study the effects of constrictions on hysteretic capillary condensation, such as the classical pore blocking effect, we have fabricated a porous alumina bilayer with different diameters in each layer. The different effective thicknesses of the two layers result in three separate FFT peaks, which correspond to optical interference of the reflections between the top and interface, interface and bottom, and top and bottom of the bilayered samples, respectively. Thus, we can monitor capillary condensation for the top layer (L_1), bottom layer (L_2), and entire porous alumina ($L = L_1 + L_2$) simultaneously so as to avoid time-to-time variations. Other high order FFT peaks have

also been observed, but with smaller intensities. A pore blocking can also be investigated by fabricating bilayered samples with a smaller pore size at the top layers. In addition, this bilayer structure can also be used for self-compensation of a possible drift in the base line, which has been used to improve the sensing stability in PS sensors. [151]

So far, three bilayer samples have been fabricated by a three-step anodization of the aluminum film. After removal of the porous alumina layer anodized from 1.5 μm of the aluminum film (first anodization), the top layer of the bilayer sample is fabricated by anodizing the aluminum film under the same conditions (second anodization) as the first anodization, followed by different anodization conditions (third anodization) to fabricate the bottom layer. For example, the top layer of sample A, which has a smaller diameter at the top layer, is anodized under 15 V in 2.6 M sulfuric acid solution, while the bottom layer is anodized under 40 V in 0.3 M oxalic acid solution. The following 5 min pore widening is used to remove any possible residues inside the pores. For sample B, which has a larger diameter at the top layer, the top layer is anodized under 40 V in 0.3 M oxalic acid solution. Unlike the fabrication of sample A, the remaining aluminum film cannot be directly anodized under a much lower voltage, because of the low conductivity resulting from a thick alumina barrier layer at the bottom of the pores. To overcome this, the sample is etched with 5 wt% phosphoric acid solution for 50 min to reduce the thickness of the barrier layer, and simultaneously increase the pore diameter of the top layer. The remaining aluminum is anodized under 19 V in 2.6 M sulfuric acid, followed by a 2 min etching in the same phosphoric acid solution. For sample C, also with a larger diameter at the top layer, both the top layer and bottom layer are anodized under the same voltage of 40 V to obtain a good pore alignment between two layers. In order to obtain different pore sizes for the two layers, the sample is etched in phosphoric acid for 50 min following anodization of the top layer. Then it is additionally etched for 2 min after completion of the anodization of the bottom layer, thus ensuring different diameters for each layers.

The cross-sectional image of sample A [shown in Fig. VI.7 (a)] shows an "inkbottle"-like structure, with pore diameters of 14 nm and 27 nm for the top and bottom layers, respectively. Crossing the interface, some pores from the top layer continue into larger pores in the bottom layer, while others end at the interface. Meanwhile,

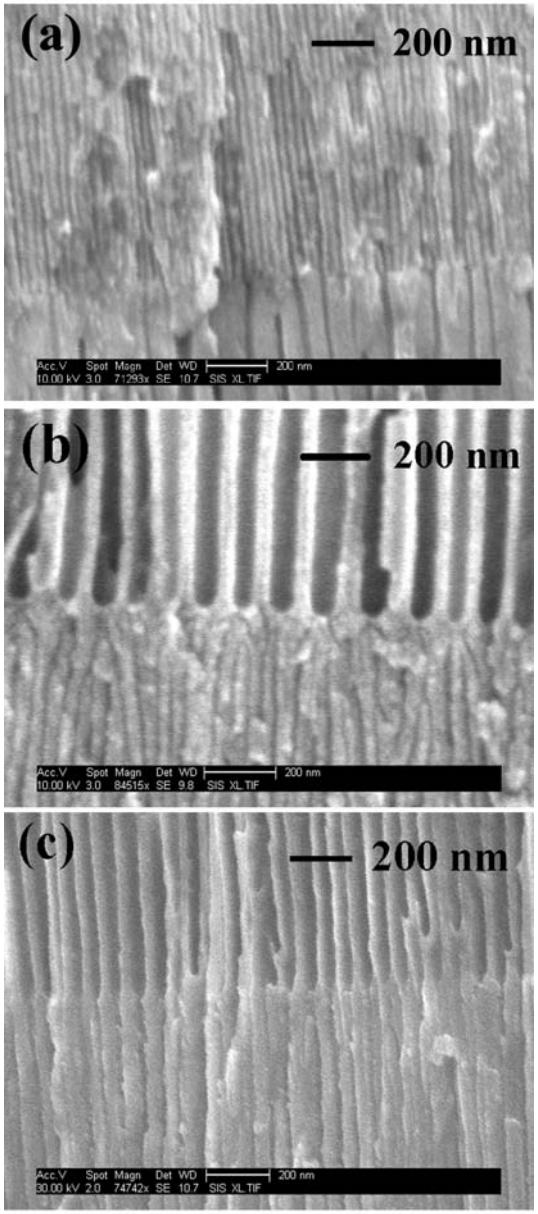

Figure VI.7: Typical cross-sectional SEM images of anodic bilayered porous alumina: (a) sample A with top layer anodized at 15 V and bottom layer anodized at 40 V; (b) sample B with top layer anodized at 40 V and bottom layer anodized at 19 V; (c) both layers anodized at 40 V but with top layer additionally widened by phosphoric acid etching.

a "funnel"-like structure is observed in both samples B and C, with a larger pore diameter at the top layer, as shown in Fig. VI.7 (b)-(c).

Fig. VI.8 (a) shows the evolution of the FFT peaks for sample C as a function of gas dosage (P/P_s). The addition of peak positions 1 and 2 is equal to the position of peak 3, which confirms that these three peaks correspond to the effective thicknesses of the top layer, bottom layer, and whole alumina layer, respectively. The size dependence of the capillary condensation is clearly observed with the condensation occurring at different P/P_s in each layer. The black squares, which indicate later transition (both along adsorption and desorption branches), correspond to the top layer with larger pore size, while the red circles, with lower transitions, correspond to the bottom layer. The transitions of these two layers are similar to those of single layers with the same pore sizes. A similar size dependence is also observed in the adsorption curves for sample A. However, a clear pore blocking effect is observed [shown in Fig. VI.8 (b)] in the desorption branch of the bottom layer (red circles), which shows the nearly same evaporation point as the top layer. This result clearly verifies that evaporation of the liquid in the bottom layer is blocked by the condensed liquid in the top layer, which has a lower evaporation point. Details of this blocking effect will be discussed in detail in the unpublished paper of Casanova, *et al.* [150]

In conclusion, we can detect molecules adsorbed inside the pores of anodic alumina by monitoring the change of refractive index. The controlled pore sizes and narrow distributions make anodized nanoporous alumina excellent systems for studies of gas adsorption and capillary condensation, and hence an excellent candidate to check theoretical models regarding capillary condensation.

VI.C Acknowledgement

Support by The Air Force Office of Scientific Research is gratefully acknowledged.

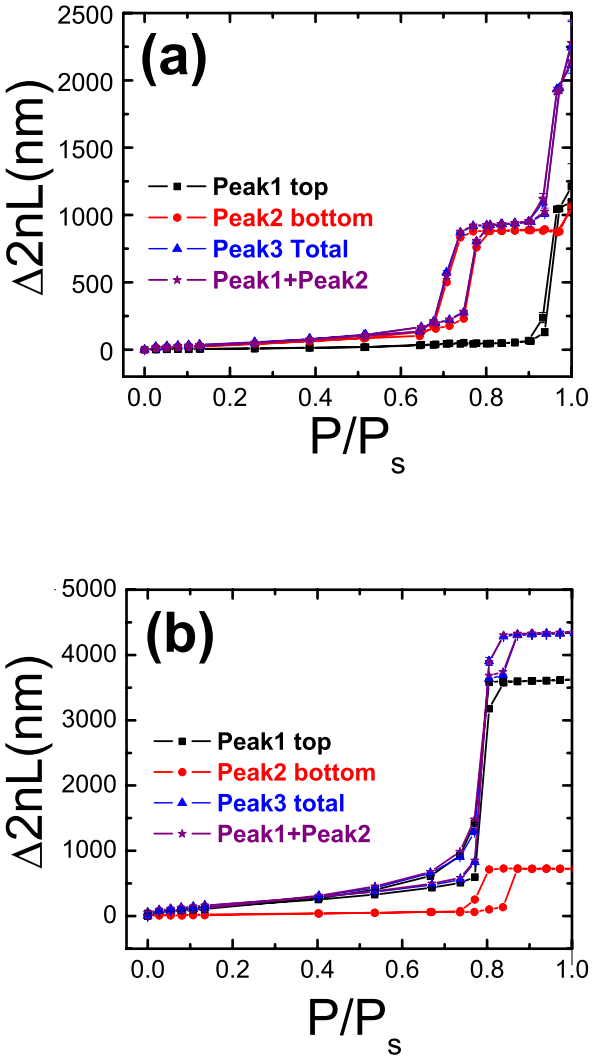

Figure VI.8: Change in 2nL of (a) sample A and (b) sample B as a function of the relative pressure of the isopropanol dosage. The change in effective thickness of the top layer (black squares), bottom layer (red circles), and entire alumina layer (blue triangles) can be obtained simultaneously by monitoring the three FFT peaks. (After Ref. [150]).

VII

Concluding remarks

In this work, we have fabricated self-ordered porous alumina masks directly on both semiconducting and insulating substrates, which can be used as evaporation shadow masks for fabrication of magnetic/nonmagnetic nanopatterns. This porous alumina shadow mask has plenty of benefits, such as a low cost, large pattern coverage and well-controlled pore sizes and periodicities. With these alumina masks, ordered FM and FM/AF exchange coupled nanodot arrays with coverage exceeding 1 cm^2 and average dot sizes and periodicities tuned in the 25-130 nm and 45-250 nm ranges, respectively, are fabricated by electron beam evaporation and subsequent mask lift-off. Masks with a periodicity of 20 nm exhibit pore densities exceeding 10^{12} per square inch, which might have relevance for magnetic media towards a corresponding density above 1 $Tbit/in^2$.

Most nanomagnetism studies are focused primarily upon the scale well above 100 nm due to fabrication limits and equipment resolution. In our work, the sub-100 nm nanodots are fabricated by the alumina masks with a macroscopically large coverage area (over 1 cm^2), which ensures that their magnetic properties can be investigated using alternative techniques that require relatively large quantities of material including SQUID, vibrating sample magnetometry, polarized neutron scattering, ferromagnetic resonance, etc. Since the 10% standard deviation in the dot size and periodicity and the 4 nm standard deviation in the dot height are relatively small, magnetic measurements of such a dot array can be used to investigate the magnetism of a single noninteracting dot.

For the 20-nm thick Fe dots, a transition from a single domain to a vortex state as a function of the dot diameter, which is quantified by the magnetic hysteresis loop width ratio defined as $W_{M=0}/W_{M=0.5M_s}$, and applied magnetic field have been observed. With consideration towards potential applications in magnetic memory systems (MRAM) and related scientific interests, these spin configurations, especially the vortex state, have been intensely investigated in this work by both magnetic measurements and simulations. This single domain to vortex state transition has also been studied by the first order reversal curve method, which quantifies the magnetic phase fractions as well as the distributions of vortex nucleation and annihilation fields. A vortex core size of 16±3 nm for Fe dots with an average diameter of 65 nm is obtained from polarized GISANS measurements, which is in good agreement with results of the Monte Carlo and micromagnetic simulations.

In addition to applications in magnetic memory systems and ultrasmall magnetic field sensors, magnetic nanostructures can also be used as artificial pinning centers for superconducting vortices. The pinning of superconducting vortices at matching fields of H_n can increase stability of the vortices and thus can be used to enhance and tune superconductor characteristics, such as superconducting critical currents. The magnetic nanodots or antidots fabricated in this work using porous alumina have average periodicities close to 100 nm, which results in a strong asymmetric flux pinning effect at a broad temperature range of 4.0-6.5 K and a large first matching field with $H_1 > 2000$ Oe. Thus, our magnetic nanostructures are well suited for applications in the case of high magnetic fields. In addition, and most importantly, we have also found that properties of the magnetic vortices can be imprinted into transport properties of the adjacent superconducting (Al) thin films. This dramatically modifies the behavior of the superconductor, for which magnetoresistance and magnetization show simultaneously reversible or irreversible behavior. These effects are attributed to out-of-plane magnetic fields produced by the magnetic dots, such as stray fields from single domain dots or out-of-plane fields from vortex cores.

In addition to the uses in nanofabrication, porous alumina can also be used as chemical and biosensing chips. By using optical interferometry, we can detect molecules adsorbed inside the pores by monitoring a change in the refractive index. The excellent

stability and disconnected pores with a uniform and adjustable size of 10-100 nm make anodized nanoporous alumina not only excellent candidates for sensing devices, but also a good candidate to investigate basic sensing mechanisms and check theoretical models, such as the vapor capillary condensation.

Bibliography

[1] F. J. Himpsel, J. E. Ortega, G. J. Mankey, and R. F. Willis, Advances in Physics **47**, 511 (1998).

[2] R. Skomski, Journal of Physics: Condensed Matter **15**, R841 (2003).

[3] X. Batlle and A. Labarta, Journal of Physics D: Applied Physics **35**, R15 (2002).

[4] C. E. Zaspel, B. A. Ivanov, J. P. Park, and P. A. Crowell, Physical Review B **72**, 024427 (2005).

[5] A. P. Malozemoff, Journal of Applied Physics **63**, 3874 (1988).

[6] U. Nowak, K. D. Usadel, J. Keller, P. Miltényi, B. Beschoten, and G. Güntherodt, Physical Review B **66**, 014430 (2002).

[7] J. Nogués and I. K. Schuller, Journal of Magnetism and Magnetic Materials **192**, 203 (1999).

[8] A. E. Berkowitz and K. Takano, Journal of Magnetism and Magnetic Materials **200**, 552 (1999).

[9] J. Eisenmenger, Z.-P. Li, W. A. A. Macedo, and I. K. Schuller, Physical Review Letters **94**, 057203 (2005).

[10] J. I. Martín, J. Nogués, K. Liu, J. L. Vicent, and I. K. Schuller, Journal of Magnetism and Magnetic Materials **256**, 449 (2003).

[11] C.-P. Li, I. V. Roshchin, X. Batlle, M. Viret, F. Ott, and I. K. Schuller, Journal of Applied Physics **100**, 074318 (2006).

[12] H. N. Bertram, *Theory of magnetic recording* (Cambridge University Press, Cambridge, Great Britain, 1994).

[13] C. D. Mee and E. D. Daniel, *Magnetic recording technology, 2nd ed.* (McGraw-Hill Companies, Inc., New York, NY, 1995).

[14] J. K. Howard, Journal of Vacuum & Science Technology **A4**, 1 (1985).

[15] R. W. Chantrell and K. O'Grady, Journal of Physics D: Applied Physics **25**, 1 (1992).

[16] A. Moser, K. Takano, D. T. Margulies, M. Albrecht, Y. Sonobe1, Y. Ikeda, S. Sun, and E. E. Fullerton, Journal of Physics D: Applied Physics **35**, R157 (2002).

[17] S. khizroev and D. Litvinov, *Perpendicular magnetic recording* (Kluwer Academic Publishers, Boston, MA, 2004).

[18] M. H. Kryder and R. W. Gustafson, Journal of Magnetism and Magnetic Materials **287**, 449 (2005).

[19] S. A. M. Tofail, I. Z. Rahman, and M. A. Rahman, Applied organometallic chemistry **15**, 373 (2001).

[20] T. W. Mcdaniel, Journal of Physics: Condensed Matter **17**, R315 (2005).

[21] T. Shinjo, T. Okuno, R. Hassdorf, K. Shigeto, and T. Ono, Science **289**, 930 (2000).

[22] J. Miltat and A. Thiaville, Science **298**, 555 (2002).

[23] A. Wachowiak, J. Wiebe, M. Bode, O. Pietzsch, M. Morgenstern, and R. Wiesendanger, Science **298**, 577 (2002).

[24] J. Li and C. Rau, Physical Review Letters **97**, 107201 (2006).

[25] K. W. Chou, A. Puzic, H. Stoll, D. Dolgos, G. Schütz, B. V. Waeyenberge, A. Vansteenkiste, T. Tyliszczak, G. Woltersdorf, and C. H. Back, Applied Physics Letters **90**, 202505 (2007).

[26] K. Y. Guslienko, V. Novosad, Y. Otani, H. Shima, and K. Fukamichi, Physical Review B **65**, 024414 (2001).

[27] K. Y. Guslienko and L. K. Metlov, Physical Review B **63**, 100403 (2001).

[28] K. L. Metlov and K. Y. Guslienko, Journal of Magnetism and Magnetic Materials **242-245**, 1015 (2002).

[29] H. Hoffmann and F. Steinbauer, Journal of Applied Physics **92**, 5463 (2002).

[30] L. D. Buda, I. L. Prejbeanu, U. Ebels, and K. Ounadjela, Computational Materials Science **24**, 181 (2002).

[31] J. Mejía-López, D. Altbir, A. H. Romero, X. Batlle, I. V. Roshchin, C.-P. Li, and I. K. Schuller, Journal of Applied Physics **100**, 104319 (2006).

[32] K. Y. Guslienko, Applied Physics Letters **75**, 394 (1999).

[33] A. J. Bennett and J. M. Xu, Applied Physics Letters **82**, 2503 (2003).

[34] OOMMF code. http://math.nist.gov/oommf.

[35] J. d'Albuquerque e Castro, D. Altbir, J. C. Retamal, and P. Vargas, Physical Review Letters **88**, 237202 (2002).

[36] J. Mejía-López, P. Soto, and D. Altbir, Physical Review B **71**, 104422 (2005).

[37] P. Vargas, D. Altbir, and J. d'Albuquerque e Castro, Physical Review B **73**, 092417 (2006).

[38] C. Kittel, *Introduction to Solid State Physics, 6th ed.* (Wiley, New York, 1986).

[39] W. H. Meiklejohn and C. P. Bean, Physical Review **102**, 1413 (1956).

[40] W. H. Meiklejohn and C. P. Bean, Physical Review **105**, 904 (1957).

[41] W. H. Meiklejohn, Journal of Applied Physics **33**, 1328 (1962).

[42] V. Skumryev, S. Stoyanov, Y. Zhang, G. Hadjipanayis, D. Givord, and J. Nogués, Nature **423**, 850 (2003).

[43] J. Eisenmenger and I. K. Schuller, Nature Physics **2**, 437 (2003).

[44] P. J. Jensen, Applied Physics Letters **78**, 2190 (2001).

[45] K. Liu, J. Nogués, C. Leighton, H. Masuda, K. Nishio, I. V. Roshchin, and I. K. Schuller, Applied Physics Letters **81**, 4434 (2002).

[46] S. Parkin, J. Xin, C. Kaiser, A. Panchula, K. Roche, and M. Samant, Proceedings of the IEEE **91**, 661 (2003).

[47] M. A. Seigler, A. M. Mack, K. Subramanian, and L. Pust, Journal of Applied Physics **91**, 7288 (2002).

[48] J. Nogués, J. Sort, V. Langlais, V. Skumryev, S. Surinach, J. S. Munoz, and M. D. Baro, Physics Report **422**, 65 (2005).

[49] I. S. Jacobs, C. P. Bean, G. Rado, and H. Suhl, *Magnetism* (Academic Press, New York, 1963).

[50] J. S. Kouvel, Journal of Physics and Chemistry of Solids **24**, 795 (1963).

[51] E. Fulcomer and S. H. Charap, Journal of Applied Physics **43**, 4190 (1972).

[52] D. Mauri, H. C. Siegmann, P. S. Bagus, and E. Kay, Journal of Applied Physics **62**, 3047 (1987).

[53] M. Kiwi, J. Mejía-López, R. D. Portugal, and R. Ramírez, Applied Physics Letters **75**, 3995 (1999).

[54] T. C. Schulthess and W. H. Butler, Physical Review Letters **81**, 4516 (1998).

[55] U. Welp, Z. L. Xiao, V. Novosad, and V. K. Vlasko-Vlasov, Physical Review B **71**, 014505 (2005).

[56] J. I. Martín, M. Vélez, J. Nogués, and I. K. Schuller, Physical Review Letters **79**, 1929 (1997).

[57] A. Hoffmann, P. Prieto, and I. K. Schuller, Physical Review B **61**, 6958 (2000).

[58] A. M. Campbell and J. E. Evetts, Advances in Physics **21**, 199 (1972).

[59] G. Blatter, M. V. Feigel'man, V. B. Geshkenbein, A. I. Larkin, and V. M. Vinokur, Review of Modern Physics **66**, 1125 (1994).

[60] U. Welp, Z. L. Xiao, J. S. Jiang, V. K. Vlasko-Vlasov, S. D. Bader, G. W. Crabtree, J. Liang, H. Chik, and J. M. Xu, Physical Review B **66**, 212507 (2002).

[61] W. Vinckx, J. Vanacken, and V. V. Moshchalkov, Journal of Applied Physics **100**, 044307 (2006).

[62] J. E. Villegas, C.-P. Li and Ivan K. Schuller, accepted by Physical Review Letters.

[63] B. D. Terris and T. Thomson, Journal of Physics D: Applied Physics **38**, R199 (2005).

[64] M. Geissler and Y. Xia, Advanced Materials **16**, 1249 (2004).

[65] C. A. Ross, H. I. Smith, T. Savas, M. Schattenburg, M. Farhoud, M. Hwang, M. Walsh, M. C. Abraham, and R. J. Ram, Journal of Vacuum Science & Technology B: Microelectronics and Nanometer Structures **17**, 3168 (1999).

[66] C. A. Ross, Annual Review of Materials Research **31**, 203 (2001).

[67] L. J. Heyderman, H. H. Solak, C. David, D. Atkinson, R. P. Cowburn, and F. Nolting, Applied Physics Letters **85**, 4989 (2004).

[68] R. Olayo-Valles, M. S. Lund, C. Leighton, and M. A. Hillmyer, Journal of Materials Chemistry **14**, 2729 (2004).

[69] L. Malkinski, R. E. Camley, Z. Celinski, T. A. Winningham, S. G. Whipple, and K. Douglas, Journal of Applied Physics **93**, 7325 (2003).

[70] X.-M. Yang, C. Liu, J. Ahner, J. Yu, T. Klemmer, and E. Johns, Journal of Vacuum Science & Technology **22**, 31 (2003).

[71] G. Schmid, Journal of Materials Chemistry **12**, 1231 (2002).

[72] H. Masuda and K. Fukuda, Science **268**, 1466 (1995).

[73] H. Chik and J. M. Xu, Materials Science and Engineering: R: Reports **43**, 103 (2004).

[74] H. Masuda, K. Yada, and A. Osaka, Japanese Journal of Applied Physics **37**, L1340 (1998).

[75] H. Masuda, F. Hasegwa, and S. Ono, Journal of The Electrochemical Society **144**, L127 (1997).

[76] O. Jessensky, F. Müller, and U. Gösele, Journal of The Electrochemical Society **145**, 3735 (1998).

[77] C. Z. Wang, G. W. Meng, Q. Q. Fang, X. S. Peng, Y. W. Wang, Q. Fang, and L. D. Zhang, Journal of Physics D: Applied Physics **35**, 738 (2002).

[78] G. Sauer, G. Brehm, S. Schneider, K. Nielsch, R. B. Wehrspohn, J. Choi, H. Hofmeister, and U. Gösele, Journal of Applied Physics **91**, 3243 (2002).

[79] H. Zeng, R. Skomski, L. Menon, Y. Liu, S. Bandyopadhyay, and D. J. Sellmyer, Physical Review B **65**, 134426 (2002).

[80] K. H. Lee, H. Y. Lee, W. Y. Jeung, and W. Y. Lee, Journal of Applied Physics **91**, 8513 (2002).

[81] K. Nielsch, R. B. Wehrspohn, J. Barthel, J. Kirschner, U. Gösele, S. F. Fischer, and H. Kronmüller, Applied Physics Letters **79**, 1360 (2001).

[82] Y. Peng, H.-L. Zhang, S.-L. Pan, and H.-L. Li, Journal of Applied Physics **87**, 7405 (2000).

[83] M. Zheng, L. Menon, H. Zeng, Y. Liu, S. Bandyopadhyay, R. D. Kirby, and D. J. Sellmyer, Physical Review B **62**, 12282 (2000).

[84] H. Masuda, K. Yashi, Y. Sakamoto, M. Nakao, T. Tamamura, and K. Nishio, Japanese Journal of Applied Physics **40**, L1267 (2001).

[85] H. Masuda and S. Masahiro, Japanese Journal of Applied Physics **35**, L126 (1995).

[86] S. Shingubara, O. Okino, Y. Murakami, H. Sakaue, and T. Takahagi, Journal of Vacuum Science & Technology B: Microelectronics and Nanometer Structures **19**, 1901 (2001).

[87] D. Crouse, Y.-H. Lo, A. E. Miller, and M. Crouse, Applied Physics Letters **76**, 49 (2000).

[88] J. H. Choi, T.-H. Kim, J. Seo, Y. Kuk, and M. S. Suh, Applied Physics Letters **85**, 3235 (2004).

[89] M. S. Sander and L.-S. Tan, Advanced Functional Materials **13**, 393 (2003).

[90] R. W. Wood, J. Miles, and T. Olson, IEEE Transactions on Magnetics **38**, 1711 (2002).

[91] I. Vrublevsky, V. Parkoun, J. Schreckenbach, and G. Marx, Applied Surface Science **220**, 51 (2003).

[92] I. Vrublevsky, V. Parkoun, V. Sokol, J. Schreckenbach, and G. Marx, Applied Surface Science **222**, 215 (2004).

[93] A. P. Li, F. Müller, A. Birner, K. Nielsch, and U. Gösele, Journal of Applied Physics **84**, 6023 (1998).

[94] L. Ba and W. S. Li, Journal of Physics D: Applied Physics **33**, 2527 (2000).

[95] R.-L. Chiu, P.-H. Chang, and C.-H. Tung, Thin Solid Films **260**, 47 (1995).

[96] M. D. Abramoff, P. J. Magelhaes, and S. J. Ram, Biophotonics International **11**, 36 (2004).

[97] Correlation length defined as the distance over which the amplitude of the autocorrelation function (ACF) decays to 37%. $ACF(x,y) \propto \int\int I(\alpha,\beta)I(x+\alpha,y+\beta)d\alpha d\beta$ was obtained from digitized SEM images $I(\alpha,\beta)$ of the arrays.

[98] A. I. Vorobyova and E. A. Outkina, Thin Solid Films **324**, 1 (1998).

[99] A. Mozalev, M. Sakairi, and H. Takahashi, Journal of The Electrochemical Society **151**, F257 (2004).

[100] Y. Yang, H. L. Chen, Y. F. Mei, J. B. Chen, X. L. Wu, and X. M. Bao, Solid State Communications **123**, 279 (2002).

[101] I. V. Roshchin, C.-P. Li, H. Suhl, X. Batlle, S. Roy, S. K. Sinha, S. Park, R. Pynn, M. R. Fitzsimmons, J. Mejía-López, D. Altbir, A. H. Romero, and Ivan K. Schuller, submitted to Physical Review Letters.

[102] G. P. Zhao, M. G. Zhao, H. S. Lim, Y. P. Feng, and C. K. Ong, Journal of Physics: Condensed Matter **17**, 151 (2005).

[103] I. L. Prejbeanu, M. Natali, L. D. Buda, U. Ebels, A. Lebib, Y. Chen, and K. Ounadjela, Journal of Applied Physics **91**, 7343 (2002).

[104] R. K. Dumas, C.-P. Li, I. V. Roshchin, I. K. Schuller, and K. Liu, Physical Review B **75**, 134405 (2007).

[105] C. Pike and A. Fernandez, Journal of Applied Physics **85**, 6668 (1999).

[106] H. G. Katzgraber, F. Pázmándi, C. R. Pike, K. Liu, R. T. Scalettar, K. L. Verosub, and G. T. Zimányi, Physical Review Letters **89**, 257202 (2002).

[107] J. E. Davies, O. Hellwig, E. E. Fullerton, G. Denbeaux, J. B. Kortright, and K. Liu, Physical Review B **70**, 224434 (2004).

[108] J. E. Davies, J. Wu, C. Leighton, and K. Liu, Physical Review B **72**, 134419 (2005).

[109] J. Olamit, K. Liu, Z.-P. Li, and I. K. Schuller, Applied Physics Letters **90**, 032510 (2007).

[110] A. Aharoni, *Introduction to the Theory of Ferromagnetism, 2nd ed.* (Oxford University Press, Oxford, England, 2000).

[111] K. S. Buchanan, P. E. Roy, M. Grimsditch, F. Y. Fradin, K. Y. Guslienko, S. D. Bader, and V. Novosad, Nature Physics **1**, 172 (2005).

[112] B. V. Waeyenberge, A. Puzic, H. Stoll, K. W. Chou, T. Tyliszczak, R. Hertel, M. Fahnle, H. Bruckl, K. Rott, G. Reiss, I. Neudecker, D. Weiss, C. H. Back, and G. Schutz, Nature **444**, 461 (2006).

[113] W. Jung, F. J. C. no, and C. A. Ross, Physical Review Letters **97**, 247209 (2006).

[114] J. K. Ha, R. Hertel, and J. Kirschner, Physical Review B **67**, 064418 (2003).

[115] F. Porrati and M. Huth, Applied Physics Letters **85**, 3157 (2004).

[116] Y. B. Grebenshchikov, N. A. Usov, and K. S. Pestchanyi, Journal of Applied Physics **94**, 6649 (2003).

[117] M. Schneider, H. Hoffmann, and J. Zweck, Applied Physics Letters **79**, 3113 (2001).

[118] This study is in collaboration with Dr. Gredig, who makes the samples with cut-edge, and Dumas *et al.*, who work on the MOKE measurements.

[119] W. Scholz, K. Y. Guslienko, V. Novosad, D. Suess, T. Schrefl, R. W. Chantrell, and J. Fidler, Journal of Magnetism and Magnetic Materials **266**, 155 (2003).

[120] N. A. Usov, Journal of Magnetism and Magnetic Materials **118**, L290 (1993).

[121] Z.-H. Wei, M.-F. Lai, C.-R. Chang, N. A. Usov, J. C. Wu, and J.-Y. Lai, Journal of Magnetism and Magnetic Materials **282**, 11 (2004).

[122] J. E. Villegas, M. I. Montero, C.-P. Li, and I. K. Schuller, Physical Review Letters **97**, 027002 (2006).

[123] V. V. Moshchalkov, M. Baert, V. V. Metlushko, E. Rosseel, M. J. V. Bael, K. Temst, R. Jonckheere, and Y. Bruynseraede, Physical Review B **54**, 7385 (1996).

[124] I. B. Khalfin and B. Y. Shapiro, Physica C: Superconductivity **207**, 359 (1993).

[125] P. S. Swartz and C. P. Bean, Journal of Applied Physics **39**, 4991 (1968).

[126] R. G. Mints and A. L. Rakhmanov, Review of Modern Physics **53**, 551 (1981).

[127] E. R. Nowak, O. W. Taylor, L. Liu, H. M. Jaeger, and T. I. Selinder, Physical Review B **55**, 11702 (1997).

[128] D. J. Morgan and J. B. Ketterson, Physical Review Letters **80**, 3614 (1998).

[129] M. J. V. Bael, L. V. Look, K. Temst, M. Lange, J. Bekaert, U. May, G. Guntherodt, V. V. Moshchalkov, and Y. Bruynseraede, Physica C: Superconductivity **332**, 12 (2000).

[130] M. J. V. Bael, M. Lange, S. Raedts, V. V. Moshchalkov, A. N. Grigorenko, and S. J. Bending, Physical Review B **68**, 014509 (2003).

[131] M. Lange, M. J. V. Bael, L. V. Look, K. Temst, J. Swerts, G. Güntherodt, V. V. Moshchalkov, and Y. Bruynseraede, Europhysics Letters **53**, 646 (2001).

[132] M. Lange, M. J. V. Bael, V. V. Moshchalkov, and Y. Bruynseraede, Journal of Magnetism and Magnetic Materials **240**, 595 (2002).

[133] J. Sort, A. Hoffmann, S.-H. Chung, K. S. Buchanan, M. Grimsditch, M. D. Baró, B. Dieny, and J. Nogués, Physical Review Letters **95**, 067201 (2005).

[134] J. Sort, G. Salazar-Alvarez, M. D. Baró, B. Dieny, A. Hoffmann, V. Novosad, and J. Nogués, Applied Physics Letters **88**, 042502 (2006).

[135] A. A. Fraerman, I. R. Karetnikova, I. M. Nefedov, I. A. Shereshevskii, and M. A. Silaev, Physical Review B **71**, 094416 (2005).

[136] We use the thermodynamic critical field H_{cr} instead of H_c. Here the out-of-plane field from the magnetic vortex cores cannot induce single flux quanta (superconducting vortices) because the superconducting coherence length of 150 nm is larger than the distance over which $H_\perp$ changes magnitude and sign. For sample B, we estimate $H_{cr} \approx 20$ Oe.

[137] F. Casanova, C. E. Chiang, C.-P. Li, I. V. Roshchin, A. M. Ruminski, M. J. Sailor, and Ivan K. Schuller, submitted to Europhysics Letters.

[138] S. Pan and L. J. Rothberg, Nano Letters **3**, 811 (2003).

[139] In collaboration with Alvarez *et al.*, we have also investigated the porous alumina mask as biological sensors, such as the detection of the binding capability between biomolecules.

[140] C. Pacholski, M. Sartor, M. J. Sailor, F. Cunin, and G. M. Miskelly, Journal of American Chemistry Society **127**, 11636 (2005).

[141] J. Gao, T. Gao, Y. Y. Li, and M. J. Sailor, Langmuir **18**, 2229 (2002).

[142] M. J. Sailor and K. L. Kavanagh, Advanced Materials **4**, 432 (1992).

[143] R. Valiullin, S. Naumov, P. Galvosas, J. Karger, H.-J. Woo, F. Porcheron, and P. A. Monson, Nature **443**, 965 (2006).

[144] S. Stapf, Nature Physics **2**, 1745 (2006).

[145] S. J. Gregg and K. S. W. Sing, *Adsorption, Surface Area and Porosity* (Academic Press, London, 1982).

[146] K. S. W. Sing, D. H. Everett, R. A. W. Haul, L. Moscou, R. A. Pierotti, J. Rouquerol, and T. Siemieniewska, Pure and Applied Chemistry **57**, 603 (1985).

[147] A. V. Neimark, P. I. Ravikovitch, and A. Vishnyakov, Physical Review E **62**, R1493 (2000).

[148] D. Wallacher, N. Künzner, D. Kovalev, N. Knorr, and K. Knorr, Physical Review Letters **92**, 195704 (2004).

[149] K. J. Alvine, O. G. Shpyrko, P. S. Pershan, K. Shin, and T. P. Russell, Physical Review Letters **97**, 175503 (2006).

[150] F. Casanova, C. E. Chiang, C.-P. Li, and Ivan K. Schuller, submitted to Applied Physics Letters.

[151] C. Pacholski, C. Yu, G. M. Miskelly, D. Godin, and M. J. Sailor, Journal of American Chemistry Society **128**, 4250 (2006).